



NRL/MR/6770--99-8392

Investigation of Power Flow from a Plasma Opening Switch to an Electron Beam Diode

D.C. BLACK

NRL National Research Council Associate

J.R. BOLLER

F.C. YOUNG

Jaycor

McLean, VA 22102-3008

R.J. COMMISSO

M.C. MYERS

S.J. STEPHANAKIS

B.V. WEBER

Pulsed Power Physics Branch

Plasma Physics Division

December 13, 1999

Approved for public release; distribution unlimited.

20000106 047

REPORT DOCUMENTATION PAGE

Form Approved
OMB No. 0704-0188

Public reporting burden for this collection of information is estimated to average 1 hour per response, including the time for reviewing instructions, searching existing data sources, gathering and maintaining the data needed, and completing and reviewing the collection of information. Send comments regarding this burden estimate or any other aspect of this collection of information, including suggestions for reducing this burden, to Washington Headquarters Services, Directorate for Information Operations and Reports, 1215 Jefferson Davis Highway, Suite 1204, Arlington, VA 22202-4302, and to the Office of Management and Budget, Paperwork Reduction Project (0704-0188), Washington, DC 20503.

1. AGENCY USE ONLY (Leave Blank)		2. REPORT DATE December 13, 1999		3. REPORT TYPE AND DATES COVERED Interim (1 Oct. 1997 — 1 Oct. 1998)	
4. TITLE AND SUBTITLE Investigation of Power Flow From a Plasma Opening Switch to an Electron Beam Diode				5. FUNDING NUMBERS	
6. AUTHOR(S) D.C. Black,* J.R. Boller,** R.J. Commisso, M.C. Myers, S.J. Stephanakis, B.V. Weber, and F.C. Young**					
7. PERFORMING ORGANIZATION NAME(S) AND ADDRESS(ES) Naval Research Laboratory Washington, DC 20375-5320				8. PERFORMING ORGANIZATION REPORT NUMBER NRL/MR/6770--99-8392	
9. SPONSORING/MONITORING AGENCY NAME(S) AND ADDRESS(ES) Defense Threat Reduction Agency Alexandria, VA 22310-3398				10. SPONSORING/MONITORING AGENCY REPORT NUMBER	
11. SUPPLEMENTARY NOTES *NRL National Research Council Associate **JAYCOR, Inc., Vienna, VA 22182					
12a. DISTRIBUTION/AVAILABILITY STATEMENT Approved for public release; distribution unlimited.				12b. DISTRIBUTION CODE	
13. ABSTRACT (Maximum 200 words) A series of experiments was performed on Hawk to investigate the coupling between a plasma opening switch (POS) and an electron-beam (e-beam) diode load. The parameters that were varied independently in this set of experiments were the conduction time, the e-beam diode anode-cathode (A-K) gap (diode impedance), and the POS-to-load distance. The optimum conduction time for maximum load power was found to be roughly 400-600 ns. The optimum A-K gap for maximum load power was found to be 10 to 15 mm, corresponding to an impedance of approximately 4 to 6 Ω . The maximum power measured in these experiments was 40 - 50% lower than that obtained in previous flashboard experiments. The current measurements between the POS and load in the long POS-to-load configuration suggest a picture in which the dominant processes that control the current transfer between the POS and the load change as conduction time is varied but are nearly independent of load impedance. The inferred POS gap at the time of peak load power is always approximately equal to the critical gap for magnetic insulation in both switch-limited and load-limited operation. This implies that the POS-load coupling is self-regulated to maintain saturated electron flow in the POS.					
14. SUBJECT TERMS Plasma opening switch				15. NUMBER OF PAGES 64	
				16. PRICE CODE	
17. SECURITY CLASSIFICATION OF REPORT UNCLASSIFIED	18. SECURITY CLASSIFICATION OF THIS PAGE UNCLASSIFIED	19. SECURITY CLASSIFICATION OF ABSTRACT UNCLASSIFIED	20. LIMITATION OF ABSTRACT UL		

1. Introduction	1
2. Experimental Configuration	1
2.1 Experimental Setup-Hardware and POS Plasma Source	1
2.2 Diagnostics	3
2.2.1 Current measurements	3
2.2.2 Voltage measurements	3
2.2.3 X-ray measurements	5
2.2.4 Axially directed ion flux measurements	6
2.3 System operation	6
2.4 Effect of diode anode composition on load performance	8
3. Experimental results	10
3.1 Variation of conduction time	10
3.1.1 Results from electrical diagnostics	10
3.1.2 Results from radiation diagnostics	17
3.1.3 Results from Faraday cups	22
3.2 Variation of A-K gap	23
3.2.1 Results from electrical diagnostics	25
3.2.2 Results from radiation diagnostics	30
4. Analysis of results and discussion	30
4.1 Diode Impedance	30
4.2 Bremsstrahlung Dose-voltage dependence	39
4.3 Current losses	40
4.4 Flow impedance and the POS gap	43
4.4.1 POS gap and flow impedance variation with conduction time	44
4.4.2 POS gap and flow impedance variation with load impedance	44
4.4.3 Flow impedance variation with inferred gap	47
4.5 Conduction time scaling	47
4.5.1 MHD model for POS conduction scaling	49
4.5.2 Mass scaling on Hawk	50
4.6 Inductance Calculations and "location" of POS opening	53
5. Conclusions	55
Acknowledgements	58
References	59

1. Introduction

High-power (TW) electrical pulses produced by pulsed-power generators, when coupled to radiation producing loads such as electron-beam (e-beam) diodes, provide a source of bremsstrahlung x-rays that is used for various applications including flash radiography, matter interaction studies, and nuclear-weapon-effects simulation. Inductive storage, together with the use of a plasma opening switch (POS), represents a technological approach for providing the power conditioning required to generate such high power pulses. This approach holds the promise of relatively compact, affordable, very high power (>10 TW) pulsed-power generators. While significant progress has been made in understanding the conduction and opening phases of the μ s-conduction-time POS,^{1,2,3} more research is needed to obtain a better understanding of the coupling between a POS and an e-beam diode.

A series of POS-load coupling experiments was performed on the Hawk inductive storage generator.⁴ This facility consists of a $1.1\text{-}\mu\text{F}$ Marx bank, storing 225 kJ at the standard, 640-kV output voltage. The Marx is discharged into a $\sim 600\text{-nH}$ circuit inductance closed by a POS, yielding a sinusoidal current pulse with a peak amplitude of 720 kA and a quarter period of 1.2 μ s. In these experiments, the POS conduction time, e-beam diode impedance, and POS-to-load distance were each independently varied. This was done both to study their effect on power coupling from the POS to the diode load, and to seek a set of parameters which provides optimum coupling between the POS and the e-beam diode.

In this work, cable-gun plasma sources^{5,6} were used. Previous, similar experiments^{1-3,7,8,9} on Hawk used flashboard plasma sources.^{6,10,11,12} Unlike previous work, a tantalum (rather than stainless steel) anode was used to produce bremsstrahlung, and the POS anode geometry differed from that used previously. Another important difference between these experiments and previous work is that this time, the cathode current and load voltage were measured (the latter with a vacuum voltmeter). These additional measurements allowed direct determination of the diode impedance, and have revealed new and subtle insights into POS physics. Also in this work, short and long POS-to-load length shots were systematically compared over a range of conditions including those resulting in maximum load power. This paper presents the results of these experiments.

2. Experimental Configuration

2.1 Experimental Setup-Hardware and POS Plasma Source

Illustrated in Fig. 1 are the two different POS-to-load configurations used on Hawk for these experiments. In Fig. 1, the long POS-to-load configuration (POS and e-beam diode load separated by 49 cm) is shown above the centerline, while the short POS-to-load configuration (POS and e-beam diode load separated by 33 cm) is shown below the centerline. The current-carrying conductors (shown crosshatched) consist of a central, 10.1-cm outer-diameter cathode concentric with a 17-cm, inner-diameter anode. Non-crosshatched areas indicate the vacuum chamber.

The POS plasma is created using twelve equally spaced cable guns,^{5,6} arranged azimuthally to inject plasma between twelve, 1-cm-diameter by 8-cm-long rods in the anode. The cable guns are constructed from 0.25-in diameter, semi-rigid coax with a 60° conical hole drilled at the end. The 12 cable-gun POS plasma sources are driven by four capacitor banks each of which consists of three, $0.6\text{-}\mu\text{F}$, 30-kV capacitors. Each cable

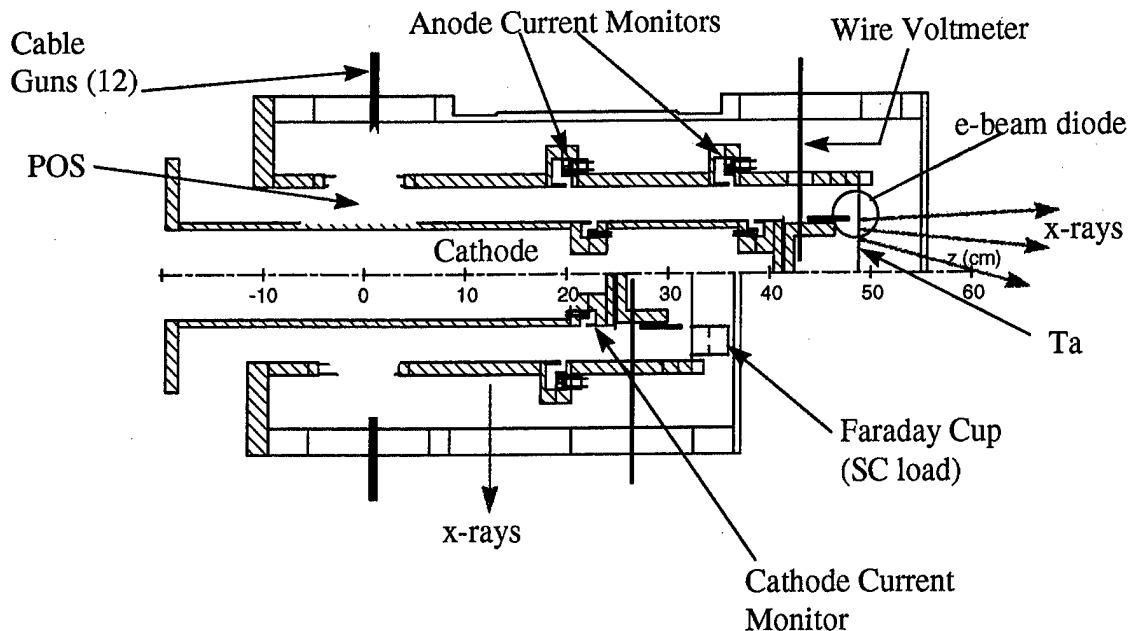


Fig. 1: The Hawk experimental configurations for both the long POS-to-load distance (shown above the axis), and the short POS-to-load distance (shown below the axis).

gun source is powered by one capacitor. For this work, the capacitors are charged to 25 kV, resulting in 35- to 40-kA peak current in each source. The time to peak current for each source is about 0.5 μ s. When the delay between doghouse and marx bank triggers is increased, plasma is injected for a longer time prior to firing the Hawk marx resulting in greater initial plasma mass in the opening switch, and consequently a longer conduction time (see Secs. 2.3 and 4.5, below). The delay between doghouse and marx bank triggers is set using an Orthometrics time delay generator.

The bremsstrahlung converter consists of a 25- μ m (1-mil) thick tantalum foil covered, on the cathode-facing side, with a 6- μ m (0.25-mil) thick aluminum foil. The purpose of the aluminum foil is to reduce the effect of the tantalum converter (presumably outgassing) on the diode behavior, as has been noticed on e-beam diode shots with no POS (see Sec. 2.4, below). Bremsstrahlung produced in the tantalum converter passes through an endplate consisting of a 0.4-mm (16-mil) thick aluminum sheet that provides the vacuum seal, followed by a 6.3-mm (0.25-in) thick Kevlar sheet that is necessary to absorb the shock of flying debris from the diode.

The diode A-K gap is adjustable using a sliding cathode tip that consists of a 10.15-cm inner-diameter, 0.3-cm thick, 3.7-cm long stainless steel ring which fits over the Hawk cathode with electrical contact made by a ring of copper fingerstock. When the vacuum chamber is pumped down, the Hawk cathode moves axially relative to the anode. Thus, the diode A-K gap with the chamber under vacuum is smaller than the A-K gap with the chamber at atmospheric pressure. To set the desired A-K gap, a spacer consisting of a 16.7-cm diameter aluminum disc of the appropriate thickness is placed between the sliding cathode and the tantalum anode. The Hawk chamber is then evacuated to allow the aluminum spacer to adjust the position and planarity of the sliding cathode tip on the center conductor. The Hawk chamber is then vented, the aluminum spacer is removed, and the Hawk chamber is evacuated for the actual shot. This method allows the vacuum diode A-K gap to be set to an accuracy of ± 0.5 mm. For some experiments, the e-beam diode load was replaced by a short circuit.

2.2 Diagnostics

An important, new aspect of this work was the implementation of additional diagnostics to accurately measure cathode current at the load and the load voltage. In addition to the current and voltage diagnostics, several radiation diagnostics were used during e-beam diode shots to measure bremsstrahlung. During shots with a short circuit load, Faraday cups were employed to obtain a measurement of axially directed ion flux at the load. This section describes these diagnostics.

2.2.1 Current measurements

Current monitors (B-dots), placed in the anode and cathode between the POS and the load, were used in both the long and short POS-to-load configurations. Each B-dot loop consisted of a single turn of copper wire approximately 3-mm in radius. The B-dots were located inside grooves that extended around the entire circumference of the cathode and anode. In the long POS-to-load configuration, four current monitors were located at each of two axial locations, two on the anode 180° apart (see Fig. 1), and two on the cathode also 180° apart (see Fig. 1). The azimuthal separation allows a crude determination of azimuthal asymmetry in the current flow. In the short POS-to-load configuration, four current monitors were located at one axial position, again two on the anode separated by 180°, and two on the cathode separated by 180°. Each of the B-dot loops provides a signal proportional to dB/dt at its particular location. This signal is then numerically integrated and converted to an effective current assuming symmetry, $I = 2\pi B/\mu_0$. Based on the dimensions of the B-dot loops, the inductance of each loop is approximately 5-10 nH. Together with the 50 Ω termination at the digitizer, this leads to a sub-nanosecond L/R response time.

The generator current is measured upstream of the POS using two independent methods. First, four B-dot loops, 90° apart, are mounted in the Hawk chamber door immediately on the load side (downstream) of the Hawk vacuum insulator. The signals from these four probes are averaged to provide a signal proportional to dI/dt that is integrated numerically to obtain the generator current. The second method is a shunt resistor immediately on the generator side (upstream) of the Hawk insulator. Four voltage pickoffs 90° apart are added to obtain a signal proportional to the generator current.

The current diagnostics are calibrated by charging the Hawk marx to 50 kV (as opposed to the usual 80 kV charge) and discharging through a short circuit load without a POS. This results in a relatively slow calibration pulse ($\sim 1.2\mu s$ quarter period). The accuracy of the current measurements is estimated to be $\pm 5\%$. All the signal cables were carefully timed to ± 1 ns. Differences in cable lengths were accounted for in the analysis.

2.2.2 Voltage measurements

The Hawk generator voltage is measured using a capacitive voltage divider¹³ in oil just upstream of the insulator. In series with this capacitive voltage divider is a resistive divider that consists of a single non-inductive film resistor in series with the transmission line, terminated by a matched digitizer input impedance. The combination of capacitive

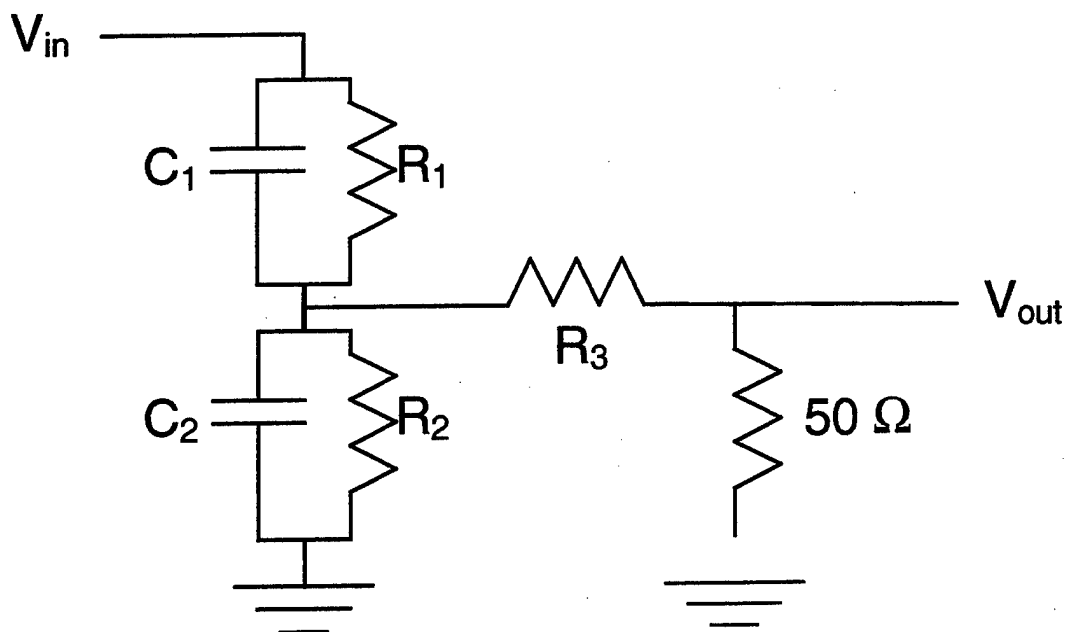


Fig. 2: Circuit diagram for the wire vacuum voltmeter used on Hawk.

and resistive dividers provides a total voltage division of 293,000 to 1. High frequency response of the probe is roughly 500 MHz.

Load voltage is measured directly using a vacuum voltmeter (PSI-VVM-16), thus eliminating the uncertainty associated with inductively correcting an upstream voltage measurement. This vacuum voltmeter consists of an RC voltage divider followed by a pure resistive voltage divider as shown in Fig. 2. Detailed analysis of the circuit response for this type of voltage divider may be found elsewhere.¹⁴ The RC divider consists of a stack of alternating insulator rings and gradient (aluminum) rings concentric with a nylon rod all mounted on an aluminum base plate (the ground side of the voltmeter). The volume between the nylon rod and the insulator stack is filled with a solution of approximately 2 g/l sodium thiosulfate (Na_2SO_4) in deionized water resulting in an insulator-stack resistivity of roughly 700 Ω (measured with a resistive bridge at 1 kHz). A tap-off electrode in the nylon center rod at the base of the voltmeter measures the RC divided voltage and leads to the tap-off stem at the center of the nylon rod. The tap-off stem contains a 2235- Ω resistor which, in series with the transmission line and terminated by the 50- Ω digitizer input impedance, provides an additional voltage division. The voltmeter was calibrated *in situ* using a Spire pulser to generate a 700-V, 100-ns, square pulse, with a risetime of 5 ns. The resulting calibration factor was 9,260 V/V.

A comparison of a typical load voltage signal, measured using the wire voltmeter, with the corresponding POS voltage, calculated by inductively correcting the upstream voltage measurement to the upstream edge of the POS injection region, is shown in Fig. 3. It can be seen from this figure that the wire voltmeter signal agrees with, but is much less noisy than, the inductively corrected signal. The ~10-ns time difference between the initial rise of the POS voltage and wire voltmeter signal is associated with POS-to-load power flow phenomena discussed in Secs. 3.1.1 and 3.2.1. This crosscheck of the measured load voltage against the calculated POS voltage tends to confirm that the wire voltmeter provides accurate, low noise measurement of the load voltage.

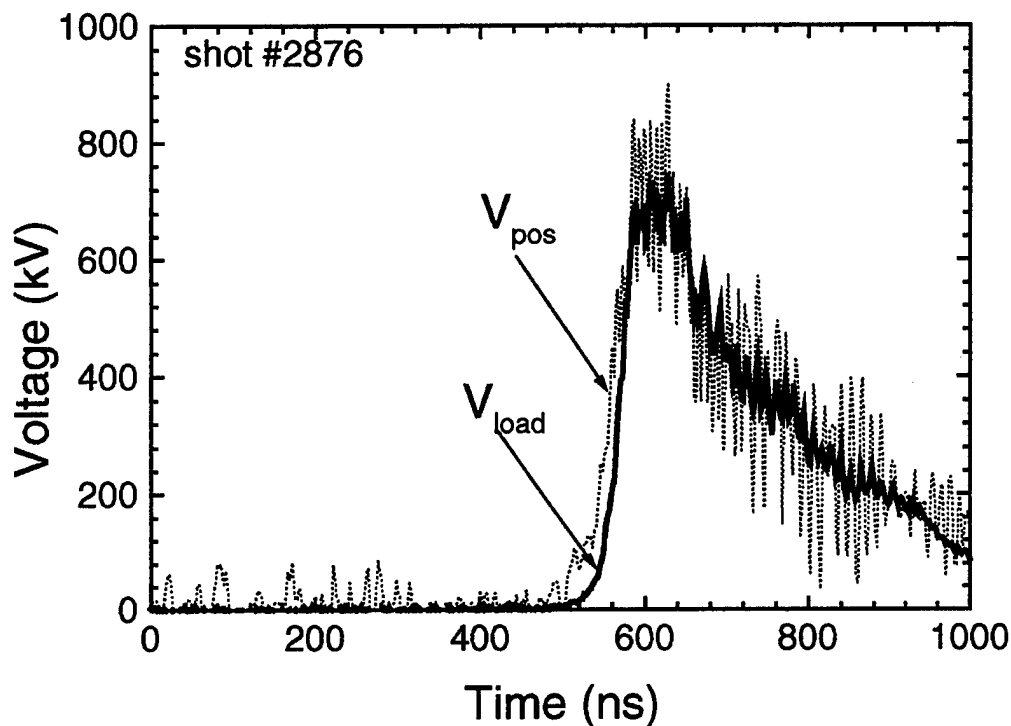


Fig. 3: Comparison of wire voltmeter signal with the calculated POS voltage from a Hawk diode shot with the short POS-to-load configuration.

2.2.3 X-ray measurements

X-rays were detected with a variety of radiation detectors. A scintillator-photodiode (SPD) combination was used to measure the x-ray time history. It consisted of a 1-in thick by 2-in diameter fast-response, organic scintillator mounted on a 2-in diameter, single-stage phototube. The SPD was fielded inside a lead "pig" (26 mm thick walls) with a 1.3-cm diameter aperture and filtered with 20 mils of aluminum. The SPD was placed 1 m from the Hawk tantalum converter package, and was biased to -2000 V. The response of the SPD expressed as the ratio of absorbed photon energy to incident photon energy, varies from 5% at photon energies of 50 keV to 8% at photon energies of 700 keV. Thus, the SPD signal is very nearly proportional to the radiated energy. Also, an unfiltered, end-viewing pinhole camera (located approximately 1 m from the tantalum converter) was used to obtain a time-integrated bremsstrahlung photograph. The 18-mil diameter pinhole in the end-viewing camera was positioned to provide a 4:1 demagnification on the film. An unfiltered, time-integrated, side-viewing pinhole camera was also employed to look at bremsstrahlung produced by high-energy electrons striking the anode (outer conductor) between the POS and the e-beam diode load. For the side-viewing camera, the 18-mil diameter pinhole was positioned to provide roughly 6:1 demagnification of the image on the film. Both Polaroid type 52 (400 ASA) and type 57 (3000 ASA) film with intensifier screens were used in the pinhole cameras.

TLD's were employed on all diode shots to obtain a time integrated dose measurement. $\text{CaF}_2\text{:Mn}$ TLD's were used because their dose-response is similar to that of silicon and they are much more sensitive than LiF TLD's. Five square (4 mm x 4 mm

x 1 mm), $\text{CaF}_2\text{:Mn}$ TLD chips in aluminum holders were mounted on the front face of the Hawk vacuum chamber. One was placed at the e-beam diode axis, while the other four were located at the diode-cathode radius (5 cm) and separated azimuthally by 90° . The TLD's were calibrated by exposing them at a rate of 60 R/hr with a Co-60 source for 17.1 hr, and then reading them out on a Harshaw model 2000 TLD reader. For the 1.25-MeV Co-60 gamma-rays, a conversion factor of 1.0 relates the absorbed dose in $\text{CaF}_2\text{:Mn}$ to the absorbed dose in silicon. However, for the lower energies expected on Hawk (a few hundred keV), $\text{CaF}_2\text{:Mn}$ is more sensitive than silicon. Rather than performing a detailed analysis of the TLD spectral response, it was assumed that the Hawk spectrum could be represented as monoenergetic at an average energy equal to one-fifth of the endpoint energy. For typical endpoint energies expected on this Hawk run (600-800 keV) a factor of 0.85 converts from absorbed dose in $\text{CaF}_2\text{:Mn}$ to absorbed dose in silicon. The calibration factor for the square $\text{CaF}_2\text{:Mn}$ TLD chips is approximately 21 rad(Si)/ μC .

2.2.4 Axially directed ion flux measurements

In addition to e-beam diode shots, some shots were taken with a short circuit load. For these shots, large-area aperture Faraday cups with no electrical bias were placed behind holes in the short-circuit plate in order to detect axially-moving ions reaching the load (see Fig. 1). Previously, small-area aperture, electrically biased Faraday cups were used in both short- and long-conduction time experiments.^{15,16,17} In the Faraday cups, the ion current passing through a 5-mm diameter aperture generates a voltage across a 64-m Ω resistor connected to ground. This voltage is measured and converted to ion current density. An applied magnetic field from permanent magnets inside the Faraday cups inhibits collection of electrons and emission of secondaries, eliminating the need for a negative electrical bias. The Faraday cups were removed for e-beam diode shots.

2.3 System operation

Data for a typical Hawk shot (#2876), including generator and load currents, load voltage, and x-rays, are shown in Fig. 4. A short POS-to-load configuration was used for this POS-driven e-beam diode shot at 640-kV erected marx voltage (80-kV charge). All the results presented in this report will be for this marx voltage. The e-beam diode A-K gap was 10.4 mm, and the conduction time (defined as the time from when the generator current, I_{GEN} , begins to rise until voltage begins to rise on the load voltmeter) was roughly 520 ns. The generator current starts to rise at time, $t=0$. The load anode current shown in Fig. 4 is the average of the two azimuthally separated current monitors on the anode, while the load cathode current is the average of the two azimuthally separated current monitors on the cathode. Because no systematic azimuthal asymmetries were observed from the B-dot signals, only the average of azimuthally separated B-dot signals will be shown in all that follows, unless otherwise noted. In Fig. 4, the load current measured on the anode rises simultaneously with the load voltage, while the load current measured on the cathode and the radiation signal rise slightly later. The time difference between the arrival of load current along the anode and the cathode was not the same for all conduction times or A-K gaps. The variation in current arrivals will be discussed in detail in Sec. 3.1.1 and 3.2.1.

The load voltage rises to roughly 700 kV, and maintains this high value for roughly 80 ns. During the voltage pulse, the difference between the load current measured at the

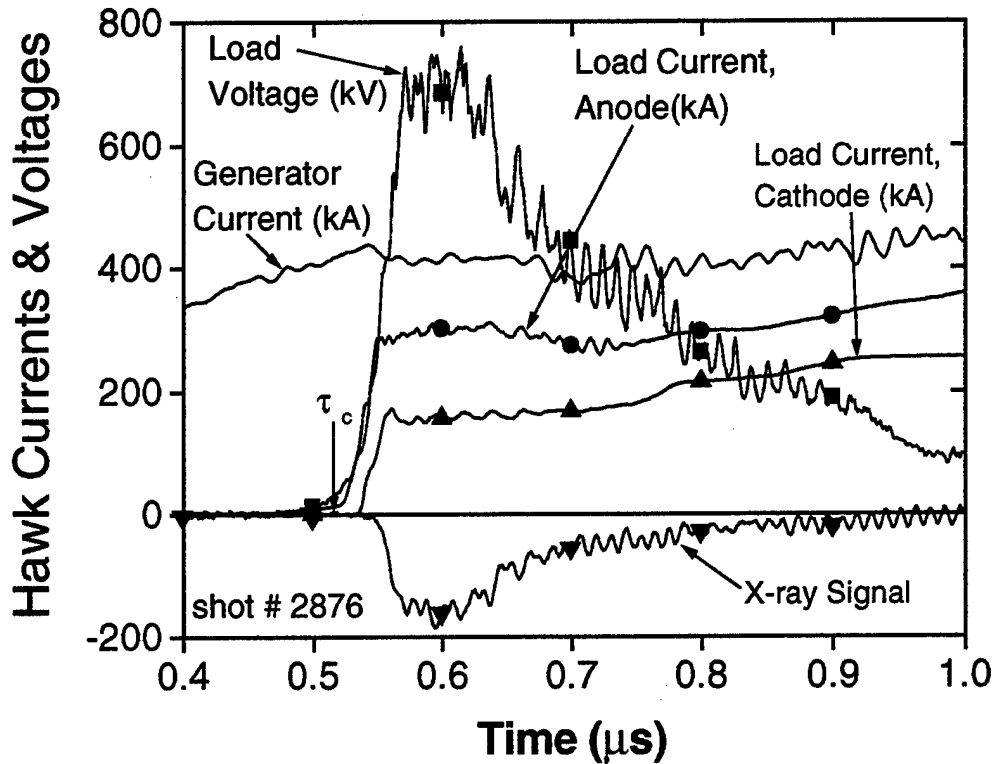


Fig. 4: Hawk current, voltage, and radiation data for a typical e-beam diode load shot in the short POS-to-load configuration.

anode and the generator current, roughly equal to 100 kA in Fig. 4, represents current loss between the switch and the load. Similarly, the difference between the anode load current and the cathode load current, more than 100 kA in Fig. 4, represents electron-flow current at the axial location of these current monitors.

As mentioned in section 2.1, the conduction time was varied by adjusting the delay between the trigger for the capacitors which drive the cable-gun POS plasma sources and the trigger for the Hawk marx bank. The actual observed delay was determined from the time difference between the initial rise of the doghouse current signals and the initial Hawk generator voltage signal. Fig. 5 shows the observed delay, dt_{obs} , versus set delay, dt_{set} , for a series of Hawk discharges in a conduction time scan for both long and short POS-to-load lengths and a variety of A-K gaps. The equation for the least-squares, best-fit line through the data in Fig. 5 is $dt_{obs} = 1.03 dt_{set} + 0.54 \mu s$. The jitter in the observed delay, determined from the root-mean-square deviation of the data in Fig. 5 from the best-fit line, is ± 50 ns (shown as dashed lines in Fig. 5). One data point in Fig. 5 falls well outside the rms deviation. The cause of this anomalous data point is not known. One possibility is that noise in the trigger cabling caused the orthometrics channel to pre-fire.

The effect of this pulsed power jitter on the conduction time jitter can be investigated by plotting the conduction time versus the observed delay for the same data used in Fig. 5. This is shown in Fig. 6, along with a typical cable-gun source current waveform. As

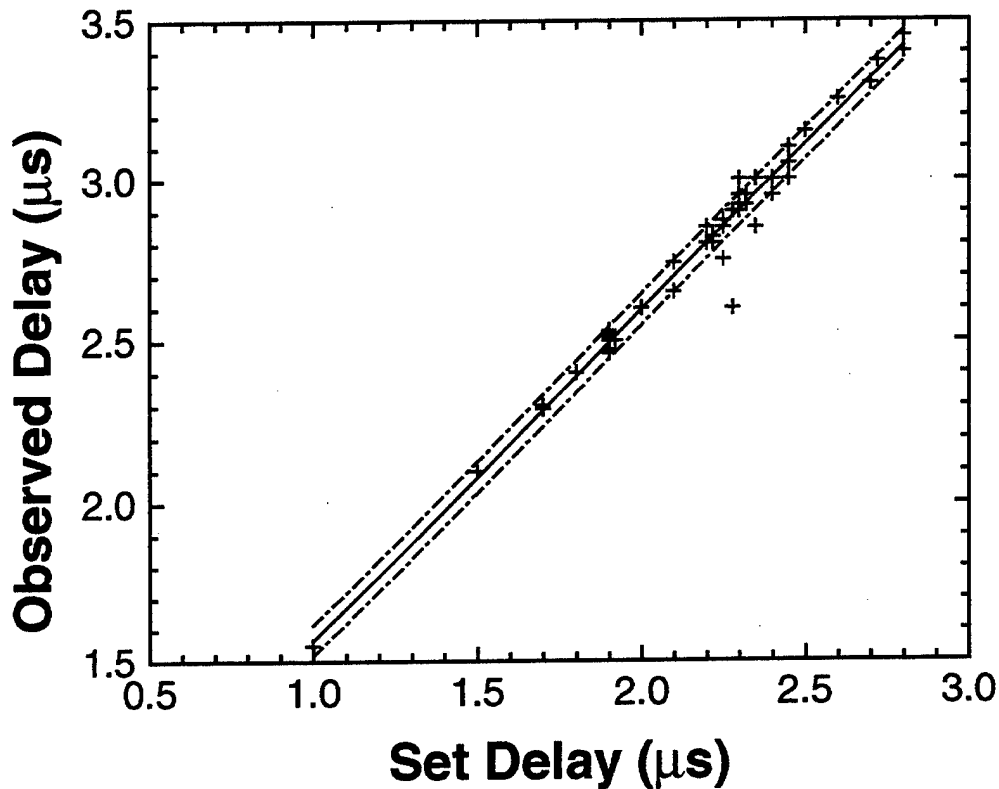


Fig. 5: Observed delay, dt_{obs} , versus set delay, dt_{set} , between firing the POS cable guns and firing Hawk. The solid line is a linear fit to the data.

expected, the data in this figure show an increasing conduction time as the observed delay is increased. However, an unexpected result is the sudden, sharp increase in conduction time at an observed delay between 2.8 μs and 3.0 μs . The conduction time is much more sensitive to small changes in observed delay between 2.8 μs and 3.0 μs than to changes outside this range of observed delay. We will look at a possible explanation for this behavior in Sec. 4.5.

2.4 Effect of diode anode composition on load performance

A series of Hawk shots was performed to investigate the effect of varying the e-beam diode anode material. Three types of load anode were tested: a stainless steel plate, a 1-mil thick tantalum foil covered on the cathode-facing side with 0.25-mil thick aluminum foil, and a bare 1-mil thick tantalum foil. Hawk shots were taken, both with and without a POS, using each of the three diode anode types. The diode impedance is calculated as the load voltage (from the wire voltmeter) divided by the average of the two load cathode current signals. Diode impedance histories for each type of diode anode for a shot with no POS are shown in Fig. 7. The A-K gap was held constant at 5 mm for all three shots compared in Fig. 7. For all shots, the zero of time is the start of the Hawk generator current. The diode impedance with the bare tantalum anode decreases earlier and is

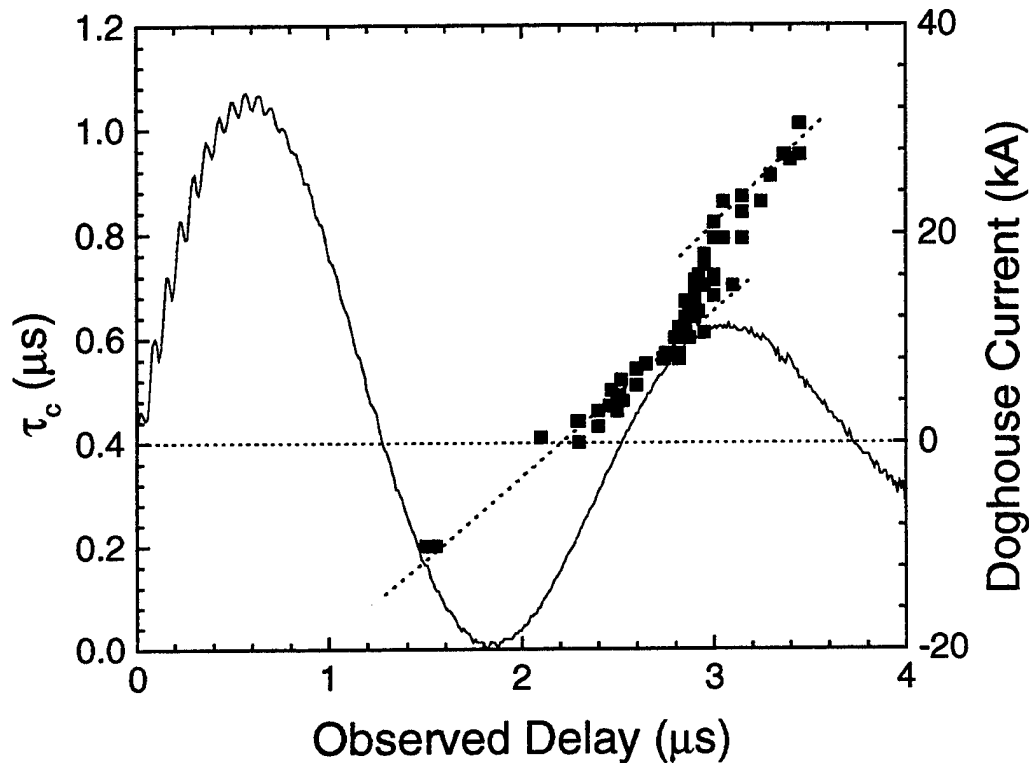


Fig. 6: Conduction time versus observed delay between the doghouse trigger and the Hawk marx trigger.

significantly lower than the impedance with either the covered tantalum or the stainless steel anode, which are roughly equivalent to each other. The onset of impedance collapse is earlier with the bare tantalum. This behavior for the bare tantalum foil may result from the release of surface impurities when the diode starts to carry current. These impurities may become ionized, leading to plasma in the load, and that may result in a reduced effective A-K gap and/or rapid diode closure. Since the high atomic number of tantalum relative to stainless steel makes it much more efficient at producing bremsstrahlung, the aluminum covered tantalum foil is preferable to stainless steel (at equal diode impedance) for the applications of interest.

When a POS was used for the same 5 mm diode A-K gap, the impedance behavior with the bare tantalum anode improved, and appeared to be no different from that with the stainless steel or aluminum-covered tantalum anode. This suggests that for shots with a POS, impurities in the tantalum do not have enough time to be released into the gap region before impedance collapse occurs. Although there were no obvious deleterious effects on diode behavior when a bare tantalum anode was used on POS shots, it is desirable to minimize any impurities at the load. Therefore, the tantalum covered with 0.25-mil aluminum was utilized as the load anode for all the Hawk data presented in this paper.

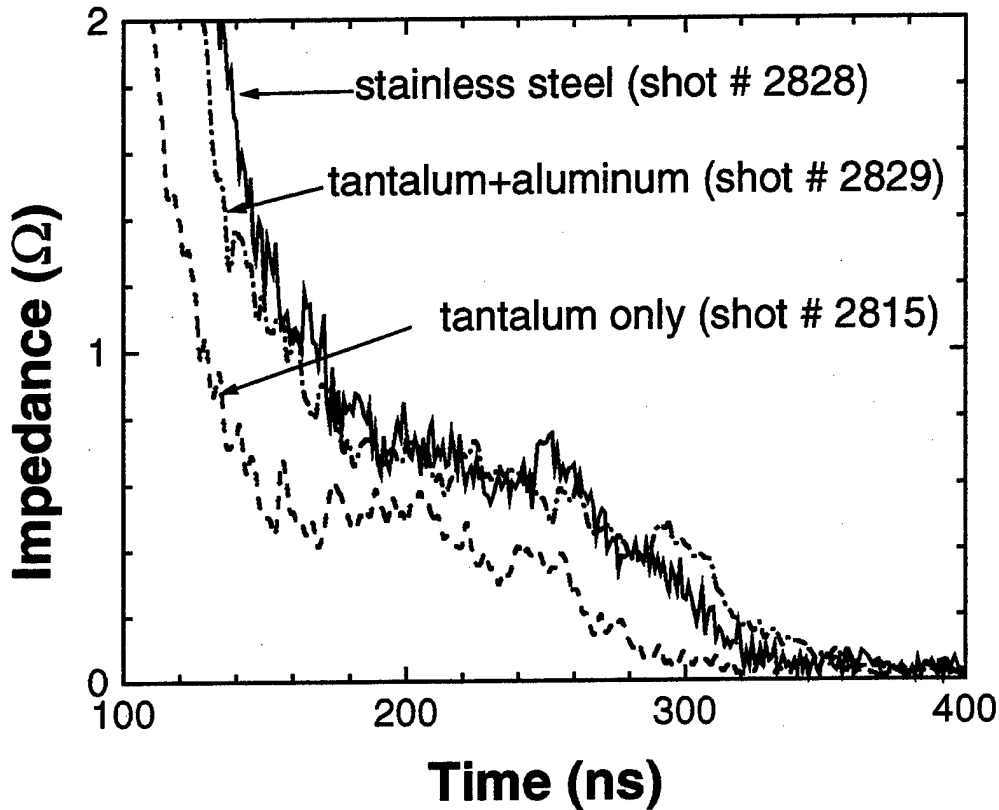


Fig. 7: Impedance histories for non-POS Hawk shots with three different diode anodes. $t = 0$ is the start of the Hawk current.

3. Experimental results

In this section, the results of conduction time scans and A-K gap scans in both short and long switch-to-load configurations are presented.

3.1 Variation of conduction time

The POS conduction time was varied for a fixed 10.4-mm A-K gap load in both the long and short POS-to-load configurations (some data for a short circuit load will also be shown).

3.1.1 Results from electrical diagnostics

Load voltage and current trends with varying conduction time are shown in Fig. 8(a) and Fig. 8(b) for the long and short POS-to-load lengths, respectively. The current and voltage data in these figures represent values at the time of peak load power, where load power is calculated as the product of load anode current and load voltage. Data for the longer POS-to-load configuration, shown in Fig. 8(a), indicate that for short conduction times ($\sim 0.2 \mu\text{s}$), load anode and cathode currents at the time of peak load

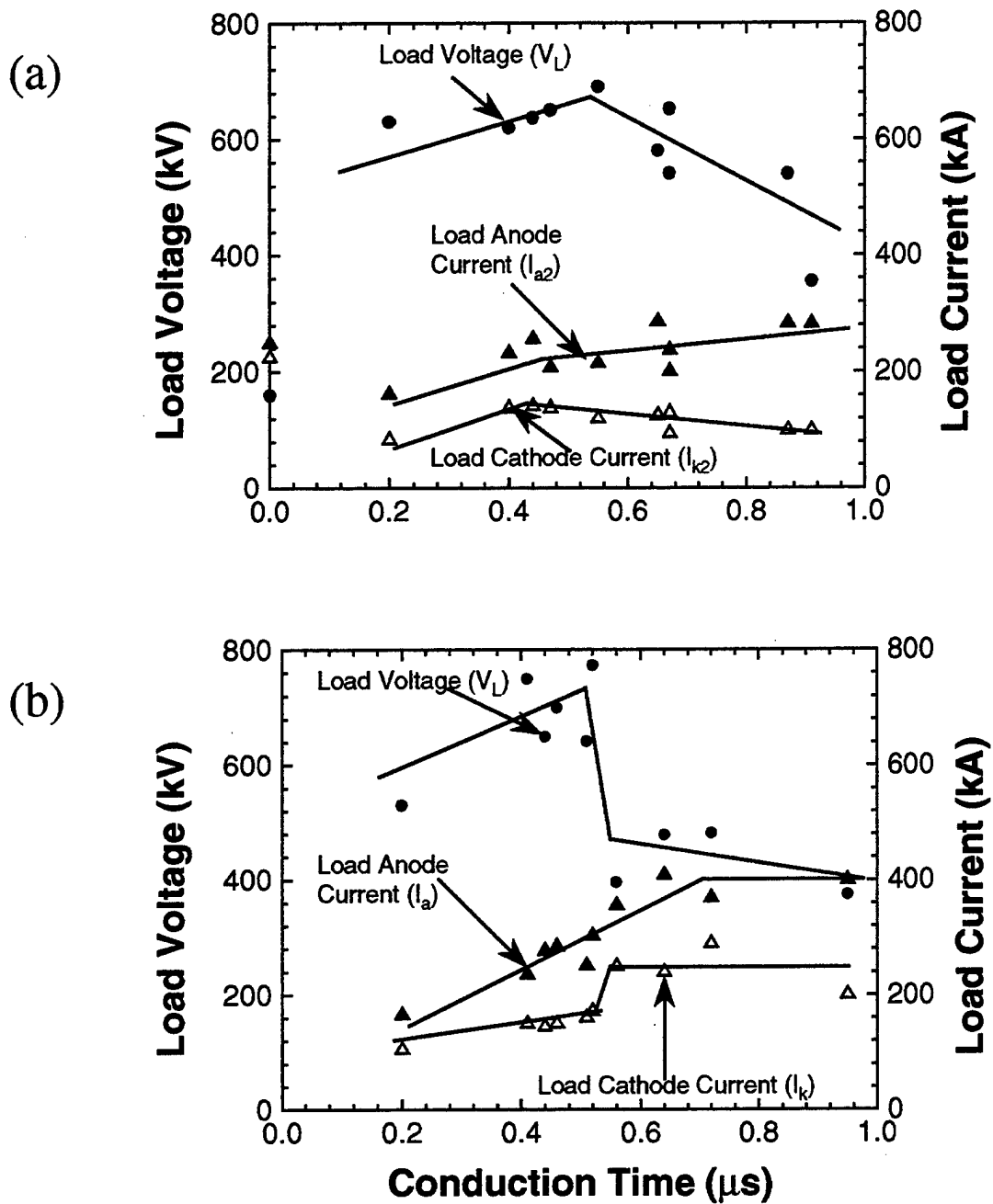


Fig. 8: Load voltage (filled circles), load anode current (filled triangles), and load cathode current (open triangles) at the time of peak load power versus conduction time for (a) the long POS-to-load configuration and (b) the short POS-to-load configuration.

power are small (approximately 150 kA and 90 kA respectively). Load anode current, I_a , is observed to increase steadily as the conduction time is increased, reaching a maximum value of just under 300 kA for conduction times near 0.9 μs . The load cathode current, I_k , remains fairly constant at approximately 100 kA. At conduction times longer

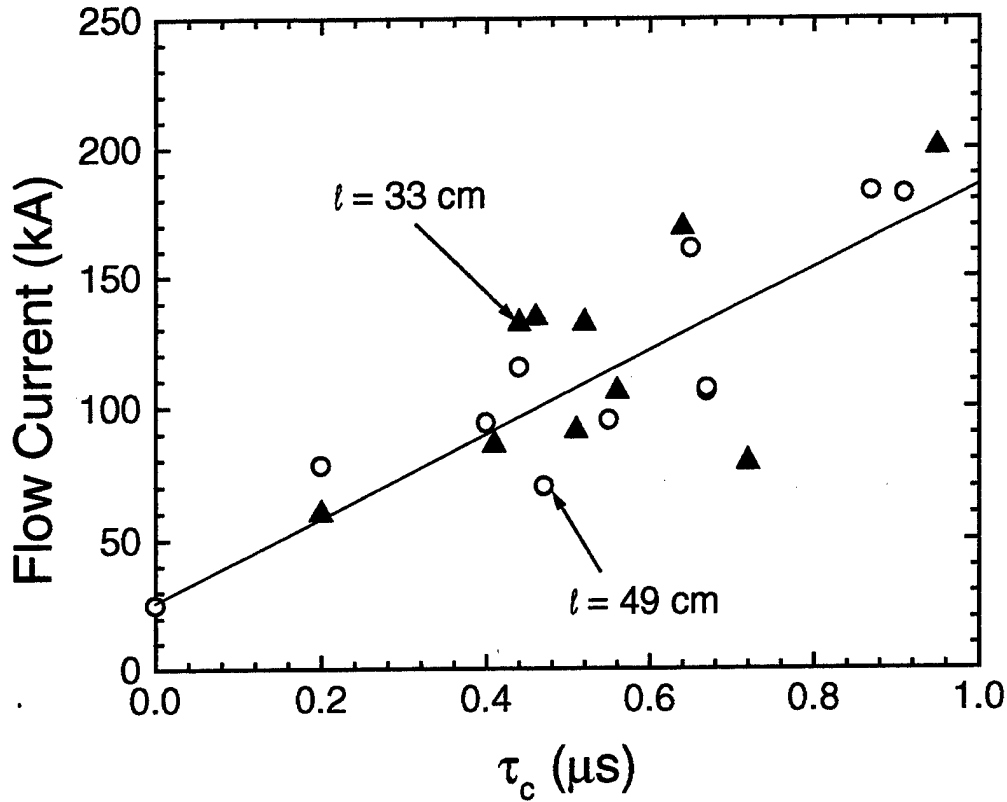


Fig. 9: Flow current, at the time of peak load power, versus conduction time for the long POS-to-load configuration (open circles) and the short POS-to-load configuration (filled triangles).

than $0.5 \mu\text{s}$, Fig. 8(a) indicates a drop in load voltage, V_L , that results in reduced diode power. The most significant difference in the data for the shorter POS-to-load configuration shown in Fig. 8(b), is the sudden transition, at conduction times just above $0.5 \mu\text{s}$, to low impedance behavior. This is indicated by the sudden drop in load voltage concurrent with the increase in load anode and cathode currents. This sudden drop in voltage (and impedance) suggests that plasma is reaching the load at long conduction times and influencing the diode behavior in the shorter POS-to-load configuration.

The flow current is computed as the difference between the load anode and load cathode currents. The flow current at the time of peak load power is plotted versus conduction time in Fig. 9 for both the long and short POS-to-load configurations. The flow current varies from approximately 50 kA at short conduction times ($\sim 0.2 \mu\text{s}$) up to 200 kA at a conduction time of $0.95 \mu\text{s}$. Although there is a fair amount of scatter in the data, flow current does not appear to be affected by the POS-to-load distance.

Fig. 10 shows the peak diode power, P_L , versus conduction time, τ_c , for both long and short POS-to-load configurations. The circles correspond to the long POS-to-load distance while the triangles correspond to the short POS-to-load distance. The conduction time corresponding to peak power is roughly $0.52 \mu\text{s}$. For greater τ_c , the load power decreases because the load voltage decreases, as can be observed in Fig. 8(a) and Fig. 8(b). For lower τ_c , the load power decreases because the generator current is

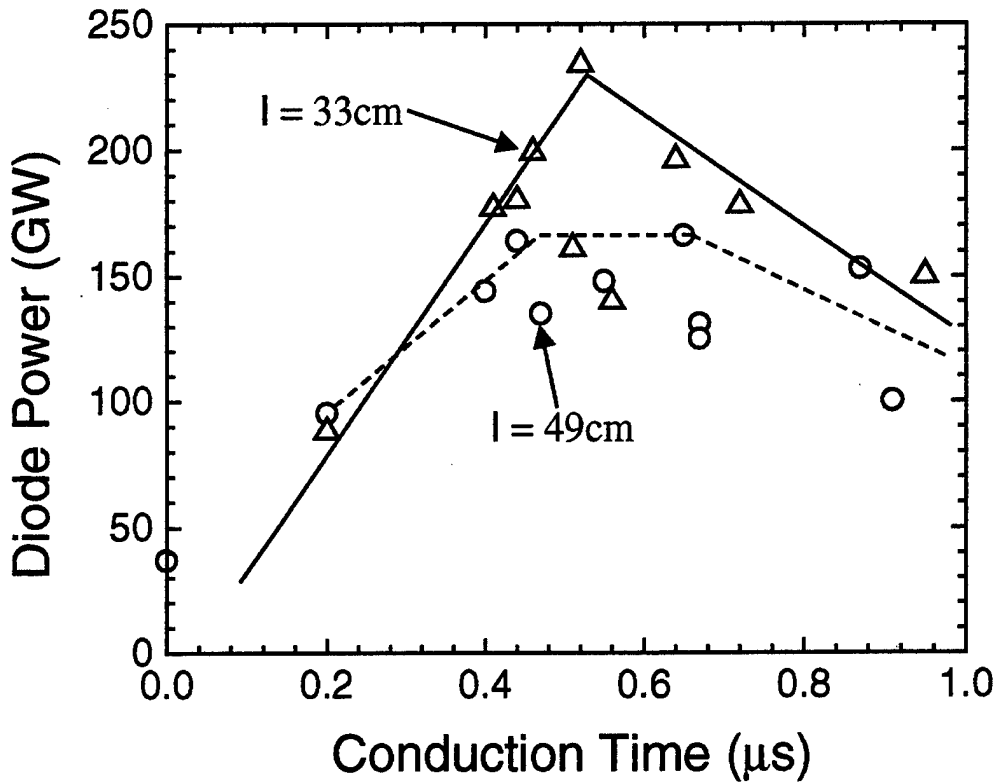


Fig. 10: Peak diode power versus conduction time for both the long (circles) and short (triangles) POS-to-load configurations.

smaller at opening, leading to smaller load currents. From the data in Fig. 10, we see that the shorter POS-to-load configuration generally yields higher diode power than the long POS-to-load configuration, particularly near the optimum conduction time for maximum diode power. By comparing I_a and V_L in Fig. 8(a) and Fig. 8(b), one can conclude that the reason for the higher power in the short POS-to-load case is a combination of higher V_L and higher I_a .

The optimum conduction time of $0.5 - 0.6 \mu s$ in the short POS-to-load configuration is significantly shorter than the $\sim 0.8 - 0.9 \mu s$ optimum observed in previous Hawk experiments with flashboard POS's.^{1,7,8} This lower optimum conduction time results in significantly lower conduction current (~ 400 kA versus ~ 700 kA) and peak electrical power delivered to the load (~ 240 GW versus ~ 400 GW). In addition to the source of the POS plasma, there are several differences between the short switch-to-load cable gun POS experiments and past flashboard POS experiments. First, the POS-to-load distance was 25 cm with the flashboard POS versus 33 cm with the cable gun POS. Second, the diode voltage at peak power was not directly measured in the flashboard POS experiments, but was inferred from an inductive correction of the upstream voltage measured at the insulator. Third, the diode anode consisted of a stainless steel plate in the flashboard POS experiments, while it consisted of an aluminum covered tantalum foil in the cable gun POS experiments. Finally, the radial electrode separation in the POS

region was 2.5 cm followed by 4 cm in the flashboard POS experiments, while it was a constant 3.6 cm in the cable gun POS experiments. Some combination of these differences may be partly or totally responsible for the disparity in peak power.

Time differences between the arrival of current and voltage signals at the load provide further insights into the behavior of the opening switch. Fig. 11 shows generator current, both downstream cathode currents, both downstream anode currents, and load voltage as functions of time for three long POS-to-load Hawk shots using a short circuit load. The subscripts 1 and 2 refer to B-dot monitors near the POS and near the load, respectively. Three different conduction times are shown. For all three conduction times, both cathode current monitors, the load voltage monitor and the downstream anode current monitor all begin to see signal at the same time. This suggests that an opening occurs in the POS plasma, and current is transferred to the short circuit load within the time required for an electromagnetic pulse moving at or near the speed of light to travel from the location of POS opening to the load. However, as conduction time increases, the first anode current signal rises earlier relative to the other current and voltage signals. This suggests the propagation of a current sheet past the first anode current monitor prior to POS opening for moderate to long conduction times. The small load voltage (~a few 10's of kV) is consistent with inductive voltage pickup as the POS opens and current is shunted to the short circuit load. Note that the current transfer is nearly 100%.

Having considered arrival time differences for electrical signals with a short circuit load, we next consider the behavior with a diode load. Fig. 12 shows the generator current, both downstream anode currents, both downstream cathode currents, and load voltage as functions of time for three long POS-to-load Hawk shots with different conduction times. One can notice significant differences as conduction time increases in terms of the arrival time of each of the signals. For short conduction times, $\tau_c \sim 160$ ns [Fig. 12(a)], the load voltage rises before any of the anode or cathode current signals begin to rise. This indicates that the POS opened (generated a voltage) before POS plasma and its associated current reached the axial location of the first anode and cathode current monitors (I_{a1} and I_{k1} respectively) at $z = 20$ cm from the POS (see Fig. 1). Also, the voltage generated immediately after POS opening is not high enough for diode emission to occur. When $V_L \approx 100$ kV all the anode and cathode currents (with the possible exception of I_{a1}) rise simultaneously. This suggests that an opening occurs in the POS plasma, and current is transferred to the diode load within the time required for an electromagnetic pulse moving at or near the speed of light to travel from the location of POS opening to the load.

Near the optimum conduction time [Fig. 12(b): $\tau_c \sim 540$ ns], the load voltage and the first anode current (I_{a1}) rise simultaneously, while the other anode and cathode currents rise later. It is possible that the POS opens at the axial location of the first anode current monitor, nearly 25 cm upstream of the vacuum voltmeter location (see Fig. 1). The time difference between the rise of the first and second anode current signals (~ 20 ns) suggests propagation of a resistive current channel at a speed of ~ 0.9 cm/ns along the anode, similar to previous observations.^{8,19} The voltage generated across the propagating current channel is too low for diode emission to occur. The second anode-current-monitor (I_{a2}) and first cathode-current-monitor (I_{k1}) signals rise at approximately the same time, suggesting that the propagating current flow is not purely radial between the electrodes (i.e. there is an axial component to the current streamlines). The second cathode current signal (I_{k2}) rises ~ 10 ns after the second anode current signal, implying that diode-emission current begins about the time that the propagating current channel

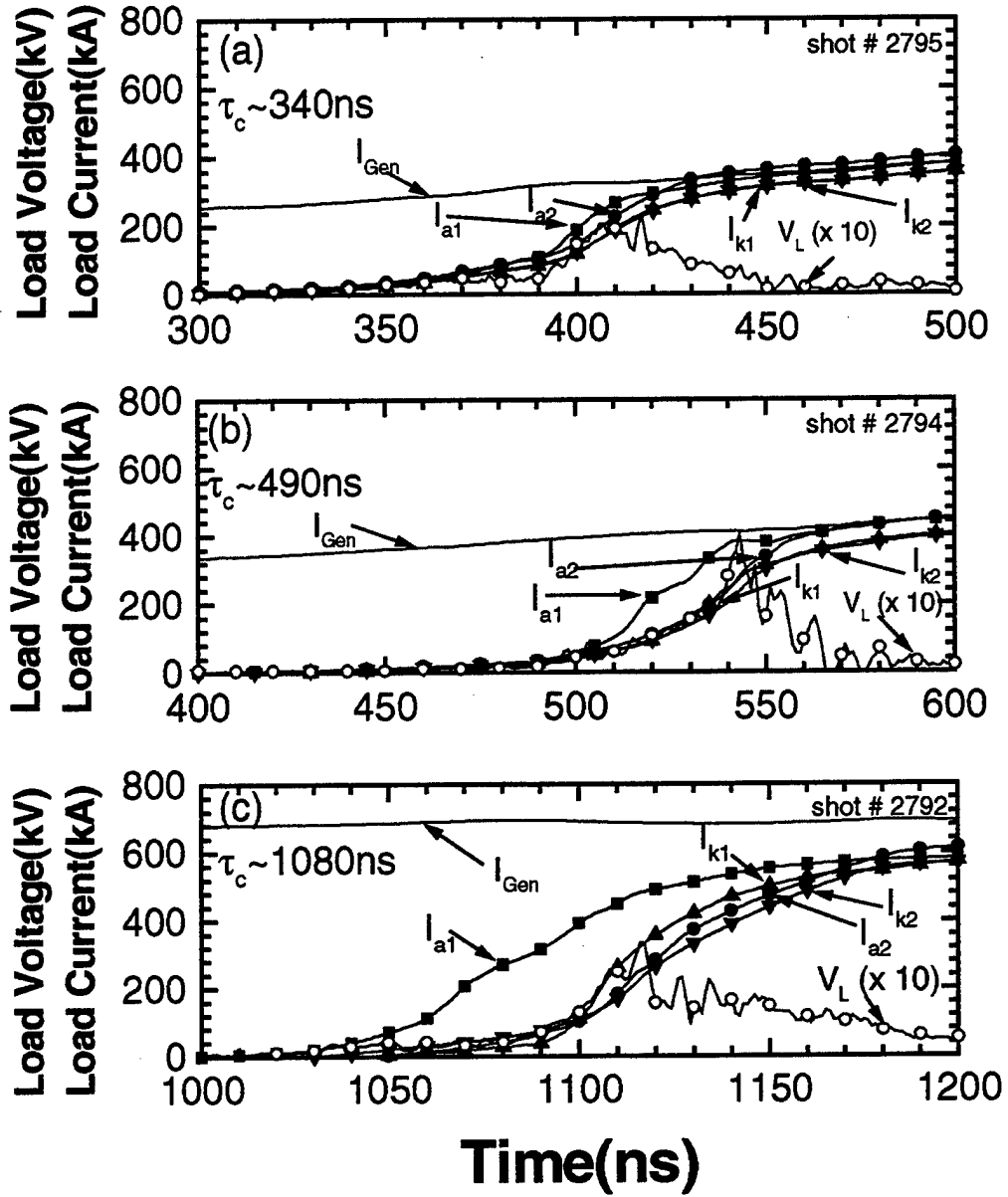


Fig. 11: Anode and cathode currents (both at two axial locations), and load voltage traces for three different conduction times on Hawk in the long POS-to-load configuration with a short-circuit load.

reaches the load. It is about this time that the load voltage and current begin to rise to their peaks and bremsstrahlung radiation is produced.

An estimate of the ion number density in the propagating current sheet may be obtained by equating the inferred 0.9 cm/ns propagation speed to the Alfvén speed. Assuming a magnetic field at the anode associated with I_{a1} and an average mass

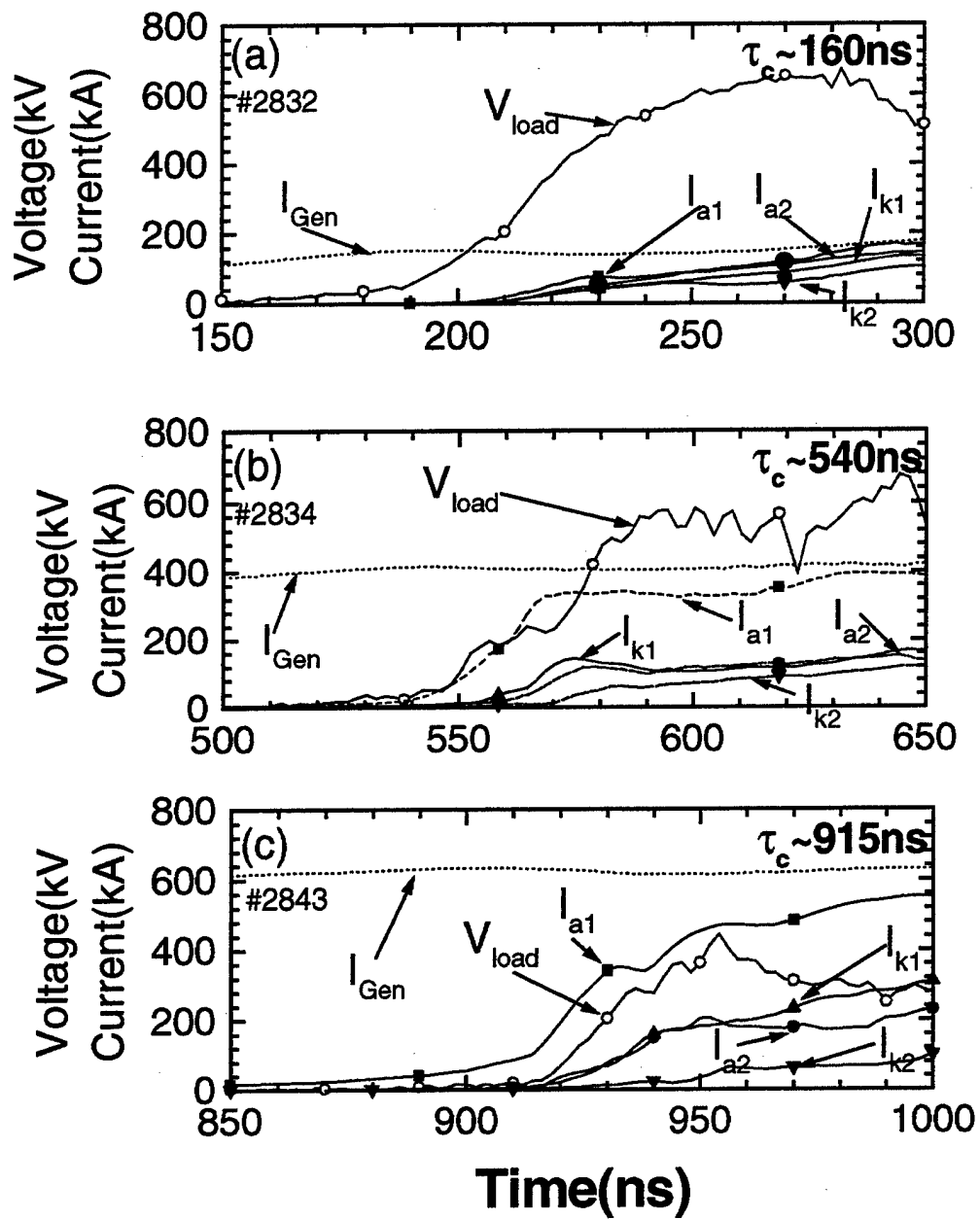


Fig. 12: Anode and cathode currents (both at two axial locations), and load voltage traces for three different conduction times on Hawk in the long POS-to-load configuration with a diode load. A-K gap is fixed at 10.4 mm for all three shots.

number of 14 (see Sec. 4.5.2), one arrives at a density for the plasma current channel of $\sim 10^{11} \text{ cm}^{-3}$. This is $\sim 0.01\%$ of the initial measured electron density in the POS.⁶

For the longest conduction time case [Fig. 12(c): $\tau_c \sim 915 \text{ ns}$], the first anode current trace shows a slow rising foot that begins before the load voltage. The load voltage begins just before or at the same time that signals are observed on the second anode current monitor and the first cathode current monitor. The time difference between the rise of the first and second anode current signals ($\sim 50 \text{ ns}$) suggests the propagation of a non-resistive current channel at a speed of 0.32 cm/ns along the anode, significantly slower than the propagation speed of the resistive current channel for the optimum conduction time. This behavior suggests that the current channel becomes resistive (in a sense opening occurs) at approximately the same time as it reaches the axial location of the second anode current monitor or, possibly, the load. The signal on the second cathode current monitor rises $\sim 10 \text{ ns}$ after the start of the main voltage pulse, implying that diode-emission begins after the current channel reaches the load. The slow rising foot on the voltage trace may be a result of the inductive voltage associated with the current channel moving past the location of the wire voltmeter.

Fig. 13 shows downstream current and voltage measurements for short POS-to-load configuration Hawk shots at three different conduction times. The results are similar to those observed in the long POS-to-load configuration. For short conduction times [Fig. 13(a)], the load voltage begins to rise before either of the load current monitors start to indicate current, and the load anode and cathode current signals rise simultaneously. Closer to the optimum conduction time [Fig. 13(b)], the load anode current signal rises simultaneously with the load voltage, while the load cathode current signal begins to rise several nanoseconds later. At long conduction times [Fig. 13(c)], the load anode current begins to rise slightly before the load voltage, while the load cathode current rises at the time the load voltage begins to rise sharply.

3.1.2 Results from radiation diagnostics

The spatial distribution of current losses in the POS-to-load region can be determined from x-ray images in Fig. 14, in which side-viewing, time-integrated pinhole photographs are compared for the long and short POS-to-load lengths. The top x-ray image is from shot 2834, a long POS-to-load shot, while the bottom image is from shot 2876, a short POS-to-load shot. As the photographs are time integrated, they do not indicate when the current losses occur. However, these losses most likely occur after POS opening when there is high voltage on the load. The x-ray image for shot 2834 shows that some current is lost along the POS-to-load anode in the long POS-to-load configuration. These losses can be reduced by moving the load closer to the opening switch and thereby allowing more current to reach the load, as seen by comparing the pinhole camera result for shot 2876 to that for shot 2834 in Fig. 14. Higher load current and consequently a higher diode voltage and power result for the short POS-to-load configuration (234 GW versus 148 GW). In the x-ray image from shot 2834, emission starts at the same axial distance from the POS as it does in the image from shot 2876. Therefore, current losses appear to occur over a smaller area for the short than for the long POS-to-load configuration. Also in Fig. 14, the side-viewing pinhole camera photograph for the short POS-to-load configuration suggests increased emission from the load region, when compared to the side-viewing pinhole camera photograph for the long POS-to-load configuration. The issue of current losses in the long and short POS-to-load configurations will be revisited in Sec. 4.3.

An interesting trend is observed in the side-viewing pinhole camera pictures for the long POS-to-load case. Fig. 15 is a set of such pinhole camera photographs for a

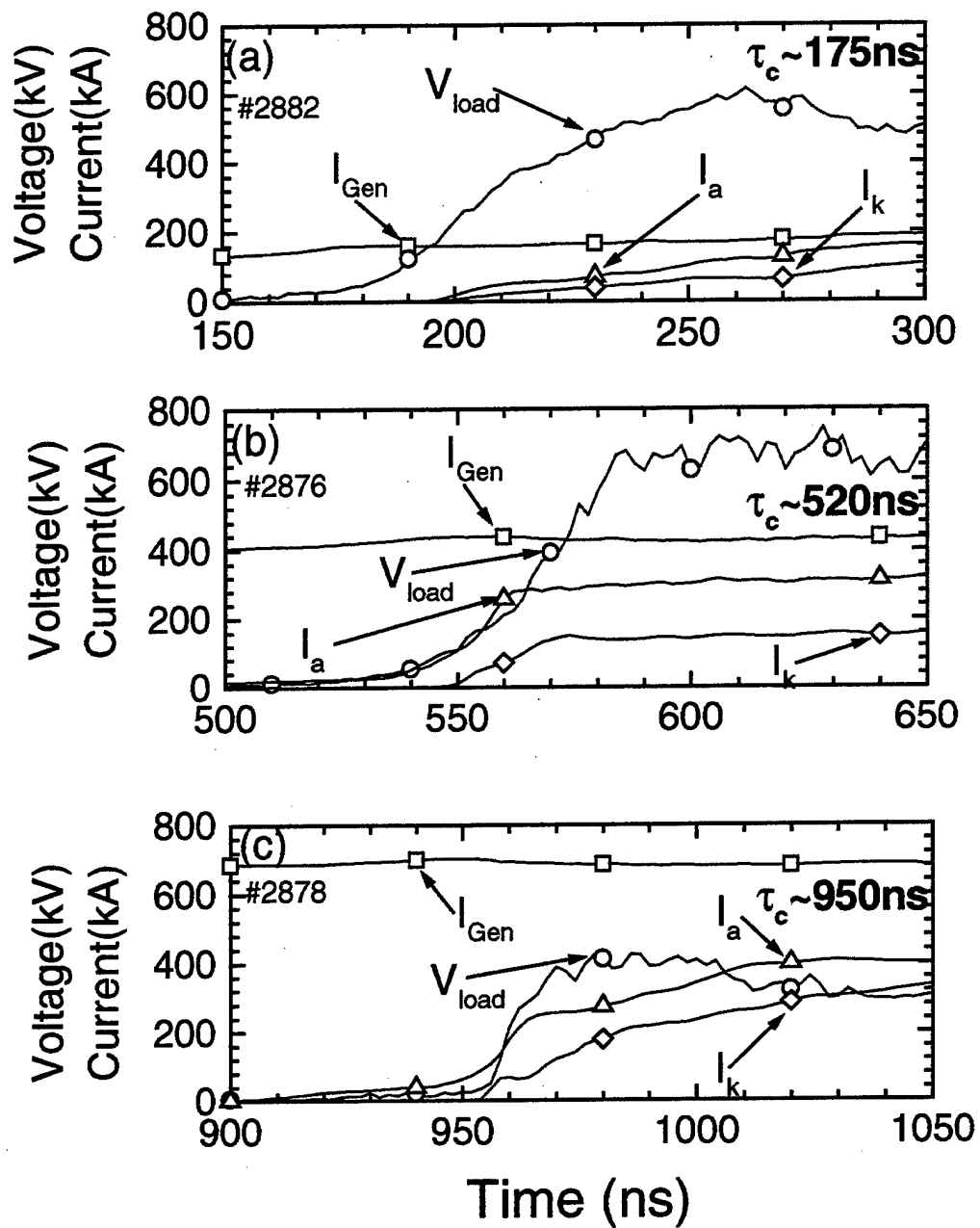


Fig. 13: Load anode current, load cathode current and load voltage traces at three different conduction times on Hawk in the short POS-to-load configuration with a diode load. A-K gap is fixed at 10.4 mm for all three shots.

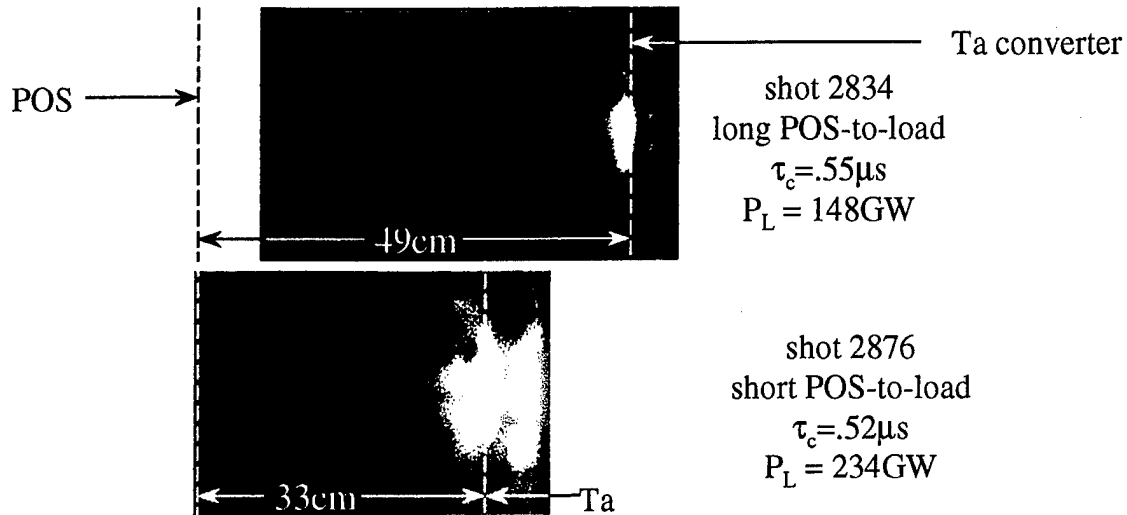


Fig. 14: Side-viewing x-ray pinhole photographs for both the long and short POS-to-load configurations with similar conduction times.

sequence of shots with conduction times ranging from $0.2\mu s$ to $0.91\mu s$. Bremsstrahlung emission observed in these side-viewing pinhole photographs suggests that high-energy electrons strike the anode region between the POS and the load at progressively increasing axial distances from the original POS location as the conduction time increases. This behavior may indicate that the location of POS opening occurs farther downstream as the conduction time is increased, and will be discussed and analyzed in more detail in Sec. 4.6.

Fig. 16 shows end-viewing x-ray pinhole photographs from several shots in the short POS-to-load configuration with conduction times ranging from $0.2\mu s$ to $0.95\mu s$. At conduction times less than $0.52\mu s$, where maximum power is achieved (see Fig. 10), pinching of the electron beam is observed with the brightest emission occurring inside the cathode radius. For conduction times greater than $0.52\mu s$, a sudden transition to a non-pinching beam is observed with much of the brightest emission occurring outside the radius of the cathode. Note that in Fig. 16, the 3000 ASA film is shown for conduction times $> 0.52\mu s$, while 400 ASA film is shown for conduction times $\leq 0.52\mu s$ (i.e. the film shown for $\tau_c > 0.52\mu s$ is 7.5 times more sensitive than the film shown for $\tau_c \leq 0.52\mu s$). The reason that the more sensitive (3000 ASA) film is shown in Fig. 16 for $\tau_c > 0.52\mu s$ is that the 400 ASA film was completely dark. This implies that much less radiation was produced for $\tau_c > 0.52\mu s$. The transition from a pinching beam for $\tau_c \leq 0.52\mu s$ to a non-pinching beam for $\tau_c > 0.52\mu s$ suggests that plasma is influencing the diode behavior at long conduction times with the short POS-to-load

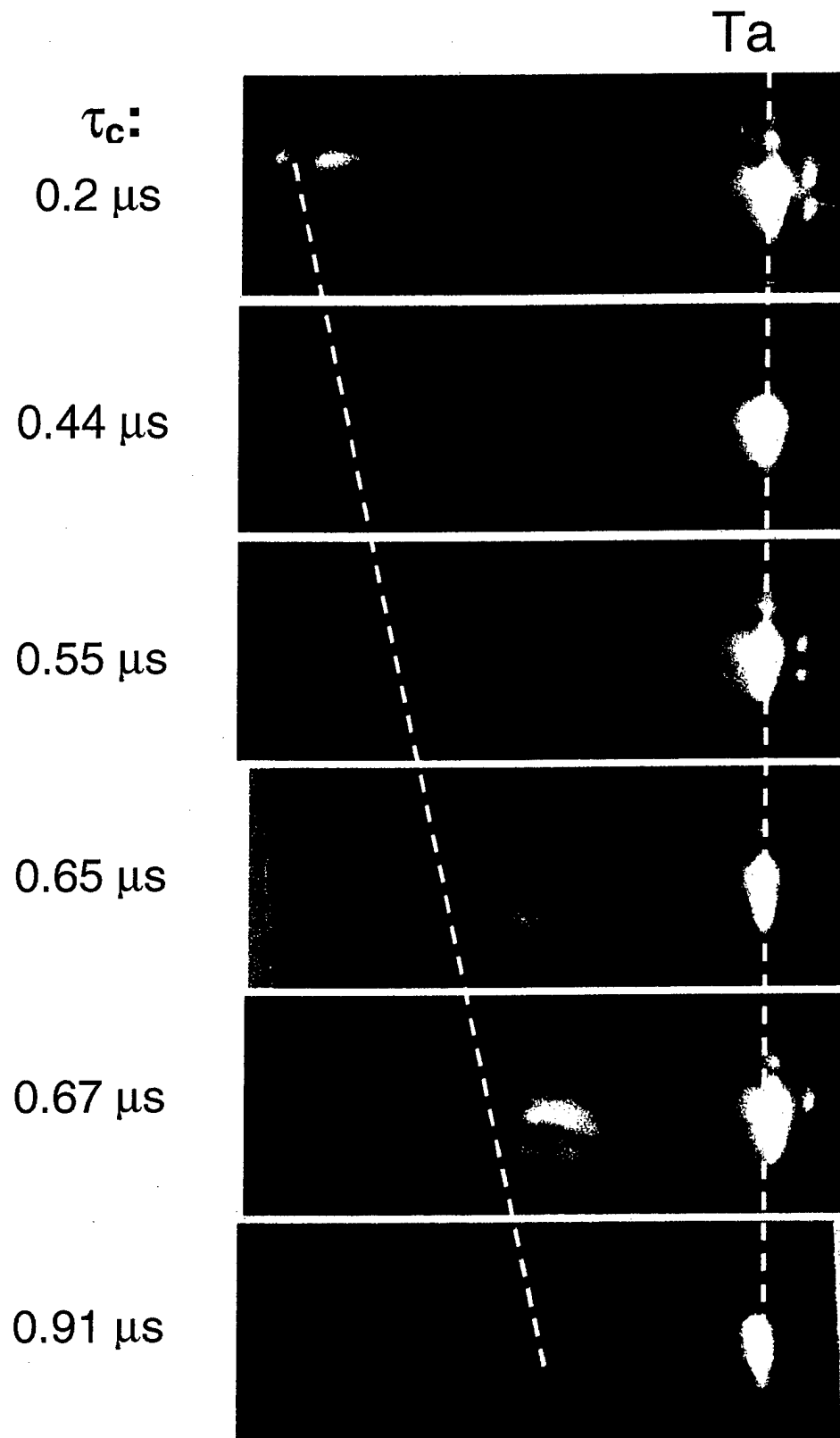


Fig. 15: Side-viewing x-ray pinhole photographs for several, different conduction times on Hawk with the long POS-to-load configuration.



Fig. 16: End-viewing x-ray pinhole camera images for several different conduction times for the short POS-to-load configuration showing sharp transition from electron beam pinching. The cathode radius is indicated by the dashed circle in each photograph. Note that the film shown for $\tau_c \leq 0.52 \mu s$ is 7.5 times less sensitive than that shown for $\tau_c \geq 0.56 \mu s$.

configuration, and is consistent with the observation of rapid voltage decrease at $\tau_c > 0.52 \mu s$ shown in Fig. 8(b). This point will be discussed further in Sec. 4.1.

The peak scintillator photodiode (SPD) signal is plotted versus conduction time in Fig. 17 for both switch-to-load configurations. The SPD signal is largest near the optimum conduction time of $0.52 \mu s$. Also, the short switch-to-load configuration yields a higher SPD signal than the long switch-to-load configuration. These results are consistent with the higher diode power inferred for the short switch-to-load configuration at the optimum conduction time (Fig. 10). As conduction time is increased above $0.52 \mu s$, the peak SPD signal in the short POS-to-load configuration drops sharply, falling below the signal obtained for the long POS-to-load configuration. However, the diode power inferred from current and voltage signals, as shown in Fig. 10, is still higher for the short POS-to-load case than for the long POS-to-load case. Comparing Fig. 17 with Fig. 8(a), Fig. 8(b), and Fig. 10, it is noted that the trends of SPD signal with conduction time for both switch-to-load configurations resemble more closely the respective trends of voltage with conduction time than the trends of diode power with conduction time. For example, the sharp drop in diode voltage for the short POS-to-load configuration at conduction times greater than $0.52 \mu s$ has a severe detrimental effect on the peak x-ray signal. This strongly suggests that the radiated x-ray energy is not directly proportional to the diode power, but depends more strongly on the diode voltage. This point will be discussed further in Sec. 4.2.

A plot of the SPD signal full-width-at-half-maximum (FWHM) versus conduction time is shown in Fig. 18. At conduction times shorter than $0.6 \mu s$, the FWHM for the long POS-to-load configuration is usually greater than the FWHM for the short POS-to-load configuration. One possible explanation for this is that the transit time for the POS plasma to reach the load is greater for the long POS-to-load configuration, thus giving more time between POS opening and diode shorting by POS plasma. The scatter in the FWHM data makes it difficult to draw any further conclusions. Also, since the shape of the SPD signal was not always triangular, the FWHM is not very useful in calculating the energy in the radiation pulse.

One way to estimate the total energy in the radiation pulse is to integrate the SPD signal. A plot of the integral of the SPD signal versus conduction time for both POS-to-load configurations is shown in Fig. 19. In this figure, the integral of the SPD signal is plotted as an open circle, while the average of the five TLD readings is plotted for comparison as a cross. In both the long POS-to-load configuration [Fig. 19(a)] and the short POS-to-load configuration [Fig. 19(b)], the trends in the SPD signal integral are very similar to those for the average TLD reading. The peak in both measurements occurs at approximately $0.5 \mu s$. In the short POS-to-load configuration, there is a sharp drop in both the integrated SPD signal and the average TLD reading when conduction

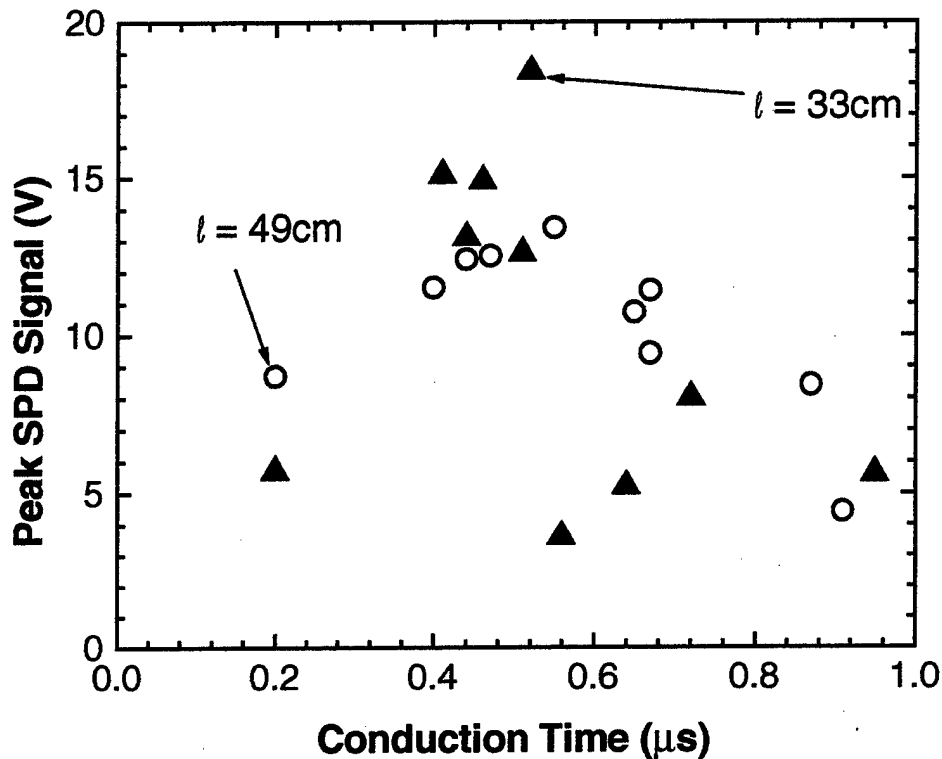


Fig. 17: Peak scintillator photodiode signal versus conduction time for both the long (open circles) and the short (filled triangles) POS-to-load Hawk configurations.

time is increased above 0.52 μs . The same behavior with conduction time was observed for the load voltage [Fig. 8(b)] and the peak SPD signal [Fig. 17].

3.1.3 Results from Faraday cups

To detect plasma reaching the diode load, Faraday cups were used on several shots with a short circuit load in both the short and long POS-to-load configurations. Faraday cups were not fielded on shots with an e-beam diode load. Faraday cups were placed behind holes in the short circuit plate in order to look for axially-moving plasma reaching the load (see Fig. 1). The measured Faraday cup voltage is converted into ion current density. Fig. 20 shows the results of Faraday cup measurements with the short POS-to-load configuration for four different conduction times. Anode load currents are shown as solid curves, and ion current densities are shown as dashed curves. The peak ion current density is nearly 100 A/cm² for the 1- μs conduction time.

The ion number density may be estimated from the current density by assuming the ion charge, $Z_i=1$, and an ion velocity in the range $0.3 \text{ cm/ns} < v_i < 1 \text{ cm/ns}$, typical of the propagation speed of the current-carrying plasma channel discussed in Sec. 3.1.1.^{18,19} This corresponds to a plasma ion density in the range $6 \times 10^{11} \text{ cm}^{-3} < n_i < 1.8 \times 10^{12} \text{ cm}^{-3}$. This is the same as, or slightly higher than, the ion number density inferred by equating the current-channel propagation velocity with the Alfvén speed (see Sec. 3.1.1). This

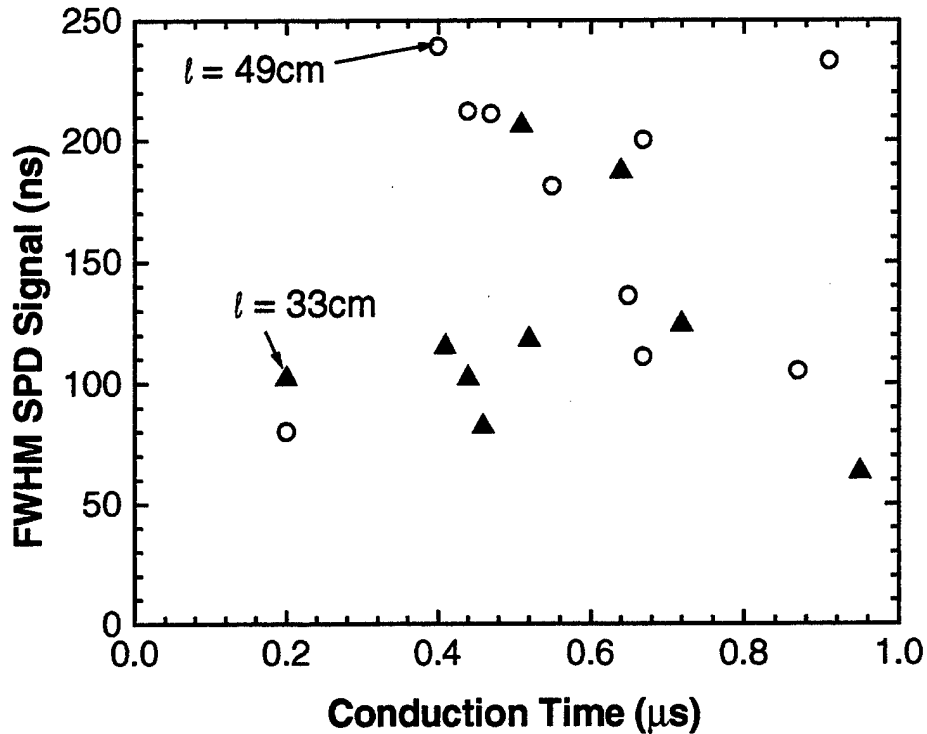


Fig. 18: Full width at half maximum for the scintillator photodiode signal versus conduction time for both the long (open circles) and short (filled triangles) POS-to-load Hawk configurations.

low-density burst of ions consistently reaches the load approximately 30 - 40 ns after the load anode current begins to rise, for conduction times ranging from 0.3 μs to 1 μs . At short conduction times ($< 0.5 \mu\text{s}$), the Faraday cup signals shown in Fig. 20 indicate a small initial burst of plasma which appears to be associated with the fast-propagating current channel discussed in Sec. 3.1.1 reaching the load. This initial small burst of plasma is immediately followed by a larger burst that appears to be associated with slower moving, higher density plasma that trails the propagating current channel. For the short POS-to-load data shown in Fig. 20, a large increase in the magnitude of the Faraday cup signal is observed when conduction time is increased beyond 0.5 μs , and the signal appears to indicate a single burst of ions. This is consistent with a large increase in the plasma density reaching the diode load. This plasma may reduce the diode impedance and thereby lower the diode power, particularly for long conduction times (see Sec. 4.1, below). For the long POS-to-load configuration data, this large increase in the Faraday cup signal for long conduction times was not observed.

3.2 Variation of A-K gap

The effect of A-K gap variation was studied in both switch-to-load configurations. For the long switch-to-load configuration, the conduction time was maintained at $0.62 \pm 0.05 \mu\text{s}$, while for the short switch-to-load configuration, the conduction time was maintained at $0.47 \pm 0.02 \mu\text{s}$. These conduction times correspond to maximum electrical power

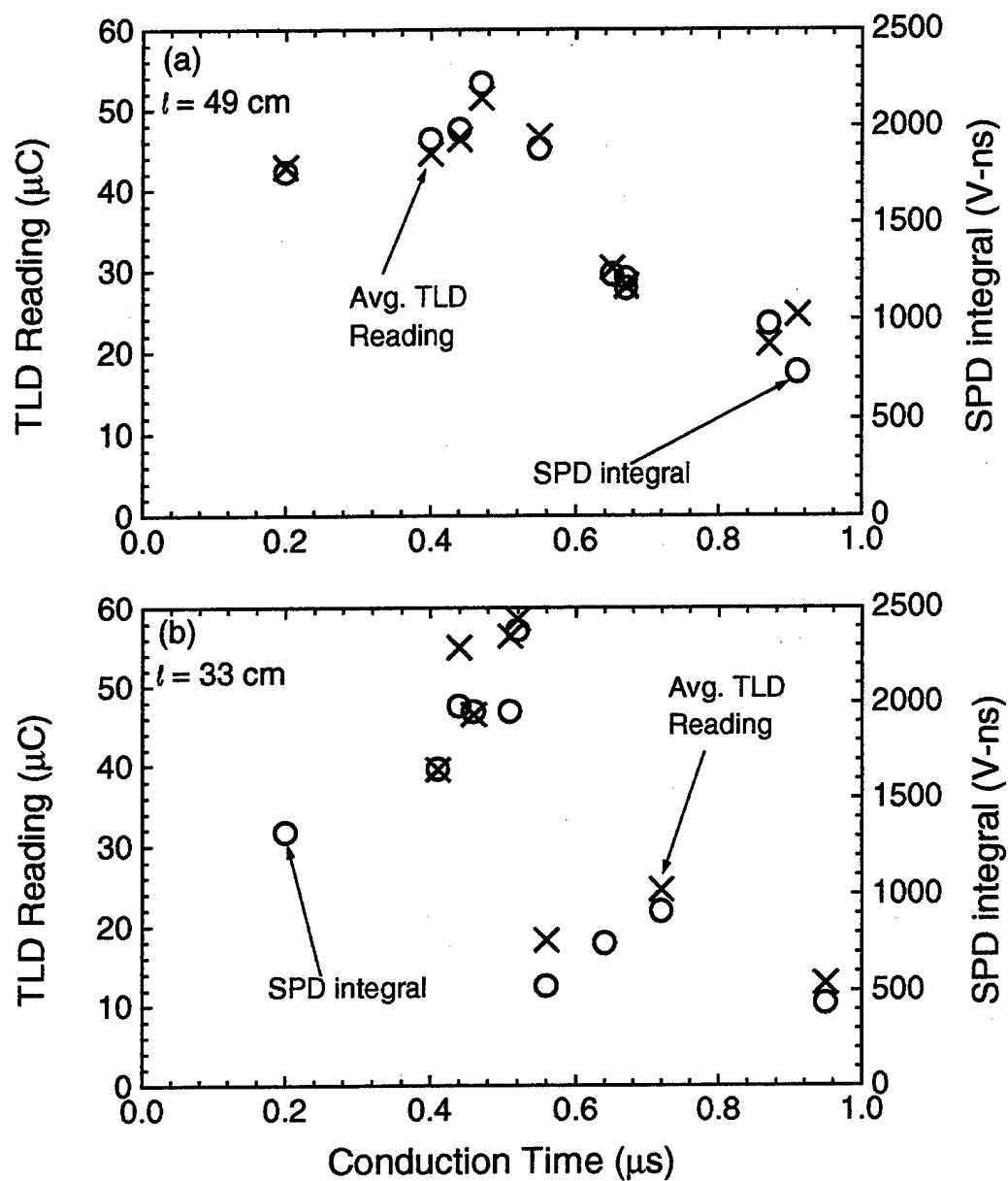


Fig.19: Integral of the scintillator photodiode (SPD) signal (open circles) and the average TLD reading (crosses) versus conduction time for (a) the long POS-to-load configuration and (b) the short POS-to-load configuration.

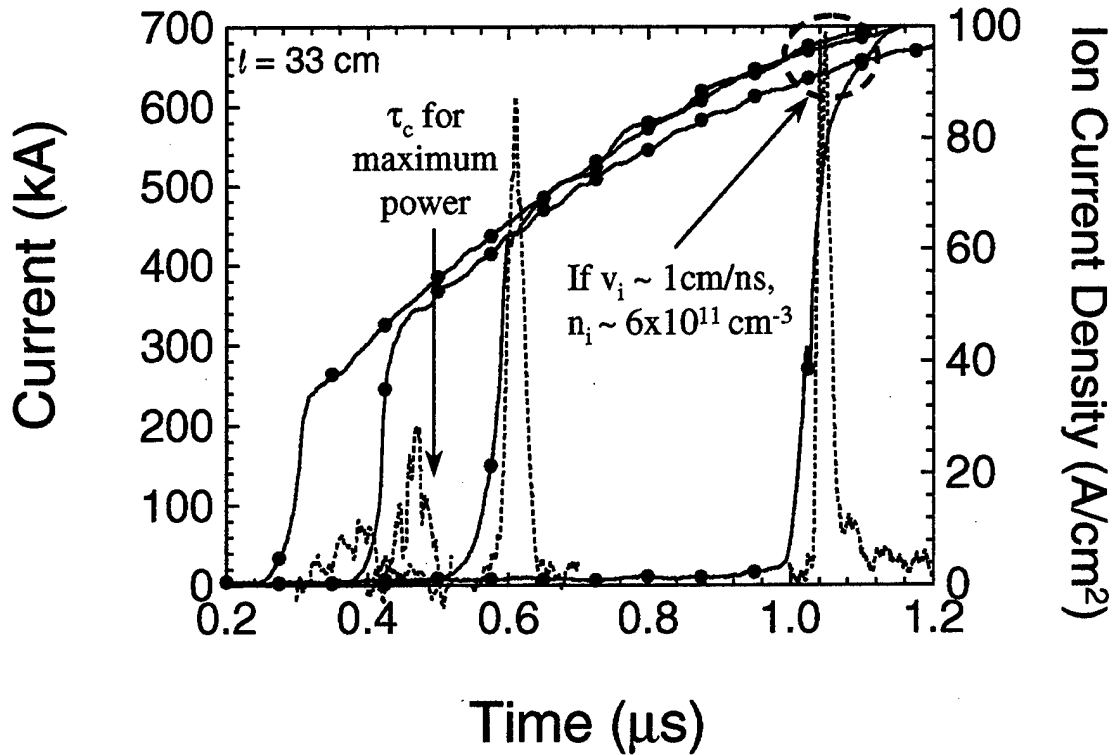


Fig. 20: Load anode current waveforms (solid lines) and Faraday cup signals (dashed lines) for four different conduction times in the short POS-to-load configuration.

delivered to the load. In both cases, the diode A-K gap was varied from a short circuit (0 mm) to 20 mm by using different thickness spacers as described in Sec. 2.3. The ultimate parameter of interest in this variation is the load impedance. The relationship between load impedance and A-K gap is discussed in Sec. 4.1.

3.2.1 Results from electrical diagnostics

Load anode and cathode currents and load voltage at the time of peak power are plotted versus A-K gap in Fig. 21(a) and Fig. 21(b) for the long and short POS-to-load lengths, respectively. The load voltage increases with A-K gap up to a gap of approximately 10 mm, above which the load voltage remains fairly constant. With the exception of the anode current in the short POS-to-load configuration, the load anode and cathode currents decrease with A-K gap up to a gap of approximately 10 mm, above which the load anode and cathode currents remain fairly constant.

The flow current at the time of peak power is plotted as a function of A-K gap for both POS-to-load configurations in Fig. 22. For the long POS-to-load configuration, represented by the open circles in Fig. 22, the data show a fair amount of scatter with flow currents ranging from 60 kA to 140 kA. However, the flow current does not vary strongly with A-K gap as indicated by the least-squares best-fit line through the long POS-to-load data (solid line). For the short POS-to-load configuration, represented by the filled triangles in Fig. 22, the flow current shows a sharp increase from near zero at a 5.6-mm A-K gap to approximately 130 kA at an 8.1-mm A-K gap. As the A-K gap is increased above 8.1 mm, the flow current remains fairly constant in the short POS-to-

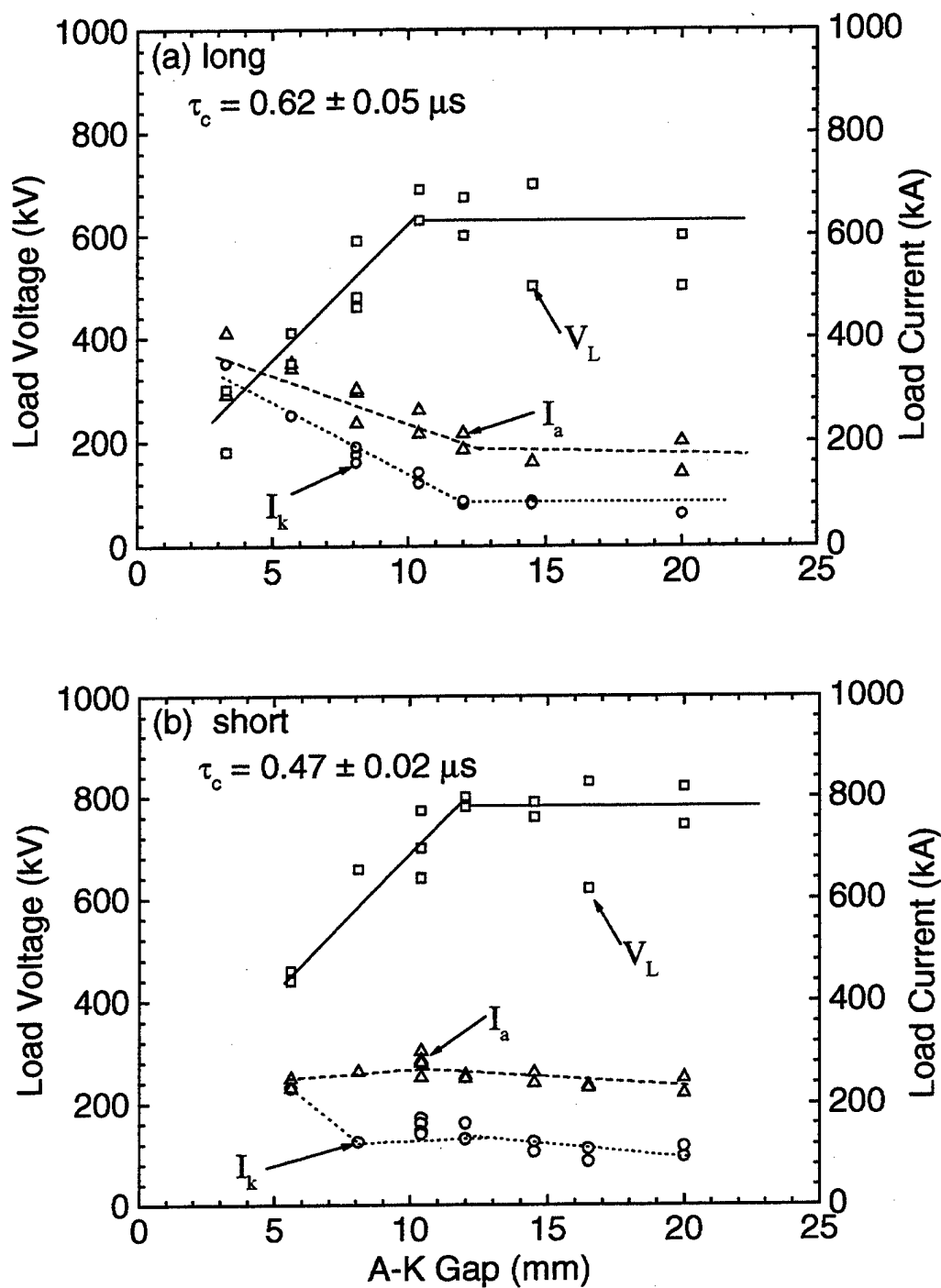


Fig. 21 Load anode current (open triangles), load cathode current (open circles) and load voltage (open squares) at the time of peak power as a function of diode A-K gap for (a) the long POS-to-load Hawk configuration, and (b) the short POS-to-load Hawk configuration.

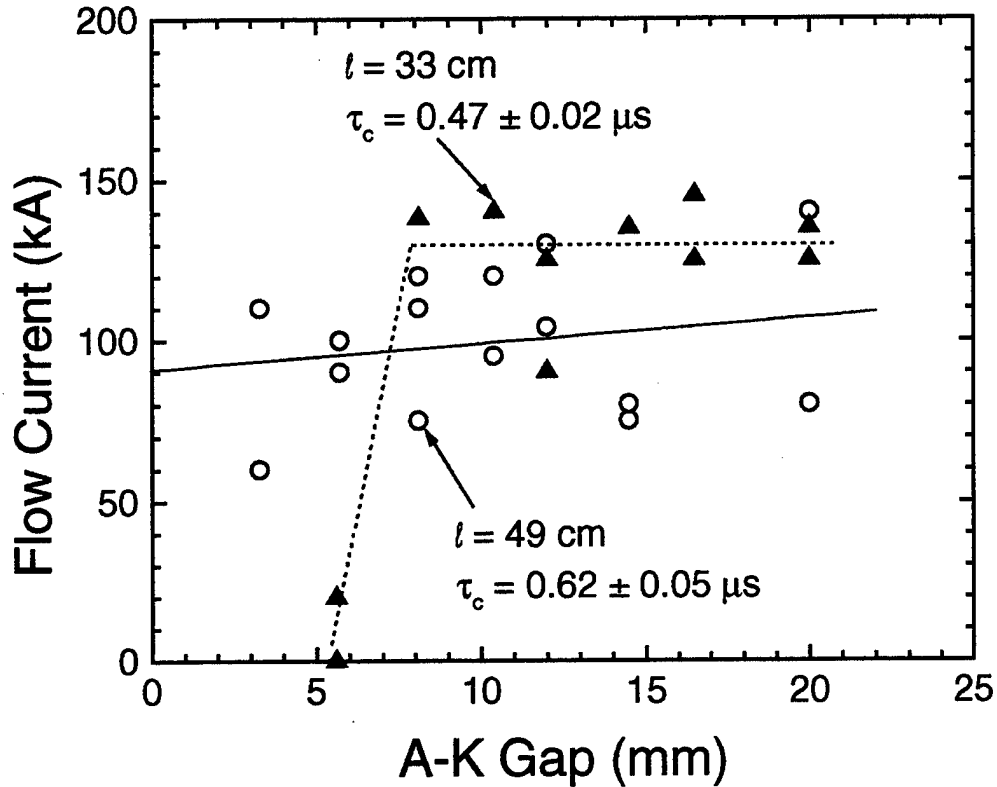


Fig. 22 Flow current at the time of peak power as a function of diode A-K gap for the long (open circles) and the short (filled triangles) POS-to-load Hawk configurations.

load configuration. The short POS-to-load data show less scatter than the long POS-to-load data in Fig. 22.

The impact of the current and voltage trends on diode power as the A-K gap is varied is shown in Fig. 23. The diode power is larger for the short POS-to-load configuration than for the long POS-to-load configuration over a broad range of A-K gaps, consistent with more current reaching the load for the short POS-to-load distance. For the short POS-to-load configuration, the optimum A-K gap for maximum power is between 10 and 15 mm, while the optimum gap for the long POS-to-load configuration is slightly smaller, between 6 and 10 mm. For diode A-K gaps greater than optimum, reduced diode current results in lower power, while for diode A-K gap less than optimum, smaller diode voltage is responsible for lower diode power. This result is consistent with the switch-limited load-limited POS picture.^{1,7,8}

Now, we can look at variation of the various current and load-voltage signal arrival times when the A-K gap is varied in both the long and short POS-to-load configurations. Load current and voltage waveforms near the time of POS opening for three long POS-to-load shots with different A-K gaps are shown in Fig. 24. The symbols used for the currents are the same as in Sec. 3.1.1. The A-K gap for Fig. 24(a) is 5.6 mm, corresponding to the load-limited operating regime. Consistent with load-limited behavior, the voltage for the 5.6-mm A-K gap shot is relatively low (~400 kV), while the

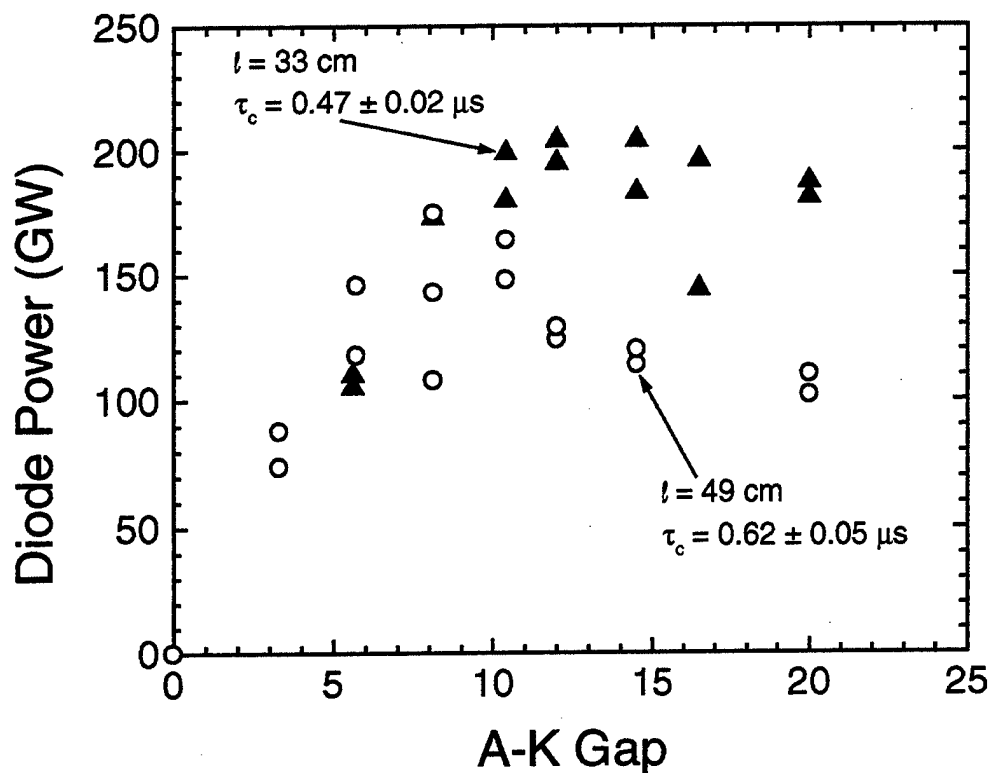


Fig. 23: Diode power versus A-K gap for both the long (open circles) and short (filled triangles) POS-to-load configurations.

load anode current is relatively high for the 640-ns conduction time ($\sim 350 \text{ kA}$) and is about 70% of the generator current. Looking at the signal arrival times for the 5.6-mm A-K gap shot, the anode current just downstream of the switch rises simultaneously with the load voltage, while the other anode and cathode currents rise slightly later in time. This behavior is similar to what is observed in Fig. 12(b) except that the shape of the voltage waveform is different with an extended "plateau" of $\sim 80 \text{ kV}$ before steeply rising when the load anode current begins to rise. The difference in magnitude between I_{a1} and I_{a2} represents current loss between the two anode current probe locations, about 100 kA at the time of peak load power. Similarly, the difference in magnitude between I_{a2} and I_{k2} represents the electron flow current at the load, approximately 100 kA at the time of peak load power.

Next, we consider Fig. 24(b), which shows data for a 10.4-mm A-K gap, corresponding to the transition between load-limited and switch-limited operation. The power is maximized for this A-K gap, and the diode impedance at this gap should be near the critical impedance.^{1,7,8} Here the load voltage is higher than in the load-limited case, while the load anode and cathode currents are lower. Despite the change in the magnitude of the current and voltage signals, the signal arrival times are very similar to those in the load-limited regime, suggesting that the current channel propagation is similar to that in the load-limited case. The current loss represented by the difference between I_{a1} and I_{a2} , greater than 150 kA at the time of peak load power, is approximately

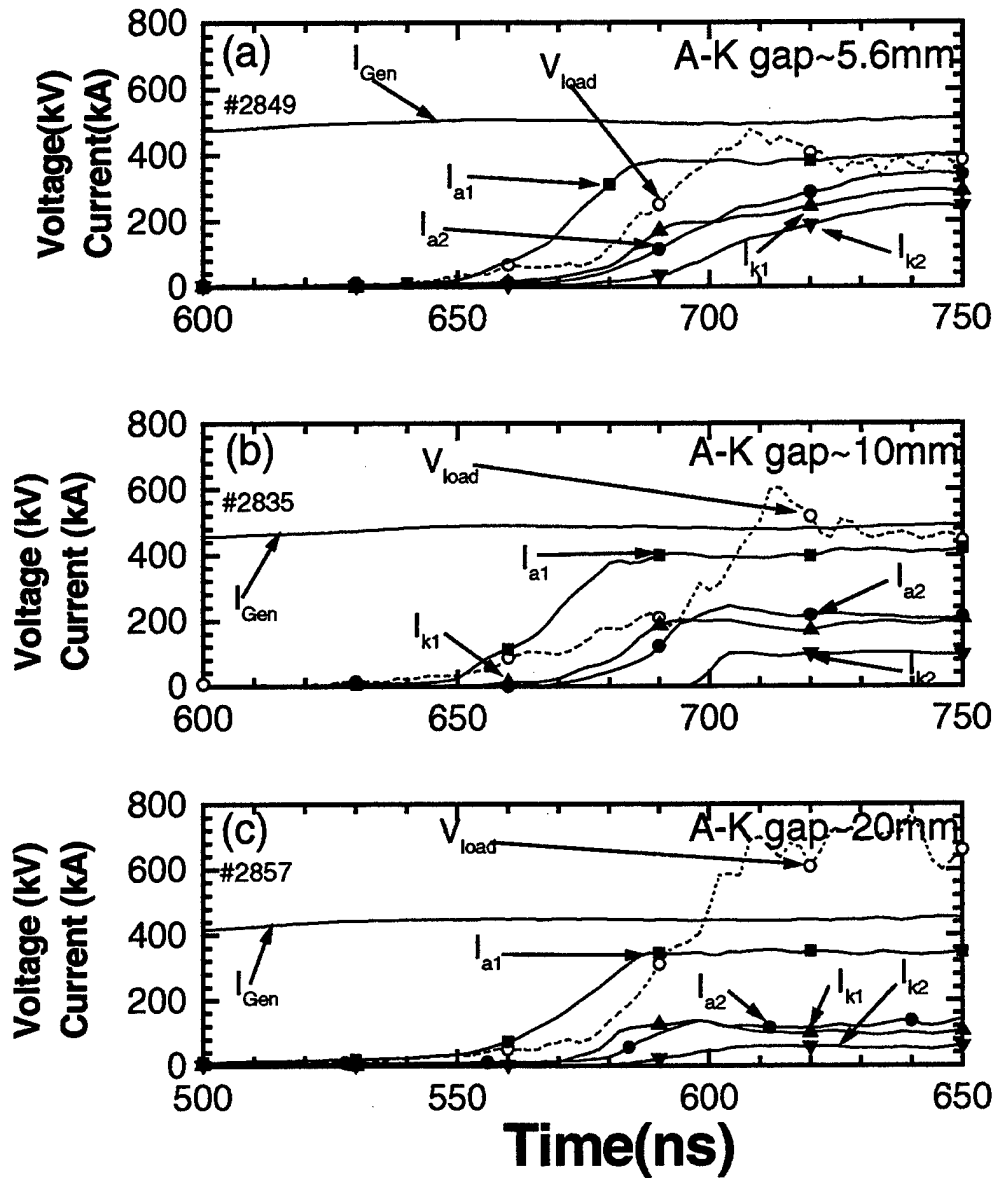


Fig. 24: Anode and cathode currents (both at two axial locations), and load voltage traces for three different A-K gap settings on Hawk in the long POS-to-load configuration.

three times higher than that for the 5.6-mm A-K gap. The electron flow current at the load (the difference between I_{a2} and I_{k2}) is also about 150 kA at the time of peak load power.

Fig. 24(c) shows data for a 20.0-mm A-K gap, corresponding to the switch-limited regime of operation. In this case, the load voltage is relatively high (~700 kV) while the load anode current (I_{a2}) is relatively low (~150 kA). As with the smaller A-K gap shots, the anode current signal just downstream of the switch rises simultaneously with the load voltage signal, while the other current signals rise slightly later in time. Thus, it appears that the A-K gap does not affect the nature of the current propagation, but does affect the magnitude of current and voltage at the load. The current loss between the two anode current probes is greater than 200 kA for this gap setting, while the electron flow current at the load is approximately 75 kA.

Similar current propagation behavior is measured for the short POS-to-load configuration, shown in Fig. 25. One important difference in the short POS-to-load configuration, for an A-K gap of 5.6 mm [Fig. 25(a)], is that the load anode current, I_a , is equal to the load cathode current, I_k . This implies that there is no vacuum flow current at the load at the time of peak power.

3.2.2 Results from radiation diagnostics

The peak SPD signal is plotted versus A-K gap for both POS-to-load configurations in Fig. 26. The trends in the peak radiation signal are similar to those of the peak load voltage in Fig. 21. This similarity is consistent with the observations made earlier in Sec. 3.1.2. The short POS-to-load configuration yields higher x-ray signals than the long POS-to-load configuration over a broad range of A-K gaps. The full-width-at-half-maximum (FWHM) of the SPD signal is plotted versus A-K gap in Fig. 27. The maximum FWHM occurs at different values of A-K gap for the two different POS-to-load configurations, and the maximum is larger for the long POS-to-load configuration. The larger FWHM for the long POS-to-load configuration may be a result of decreased POS plasma influence on the diode in the long POS-to-load configuration.

The integral of the SPD signal and the average TLD reading are plotted versus A-K gap in Fig. 28. These two time-integrated measurements show similar trends as the A-K gap is varied. For the long POS-to-load configuration [Fig. 28(a)], the SPD integral and average TLD reading exhibit a narrow peak with the maximum occurring between 8 and 10 mm. For the short POS-to-load configuration [Fig. 28(b)], a broad maximum is observed in both the SPD integral and the average TLD reading. Also, less scatter is observed in the short than the long POS-to-load configuration.

4.0 Analysis of results and discussion

Having outlined trends in the data in the previous section, we can now analyze the electrical data to determine diode impedance, flow impedance, inferred POS gap, and the critical POS gap for magnetic insulation. This analysis provides further insight into coupling between the POS and an e-beam diode load.

4.1 Diode Impedance

The impedance of a pinched-beam diode can be predicted from the critical current formula²⁰

$$I_L = (1.6) * 8500 * (\gamma^2 - 1)^{1/2} \frac{R_c}{\Delta}. \quad (1)$$

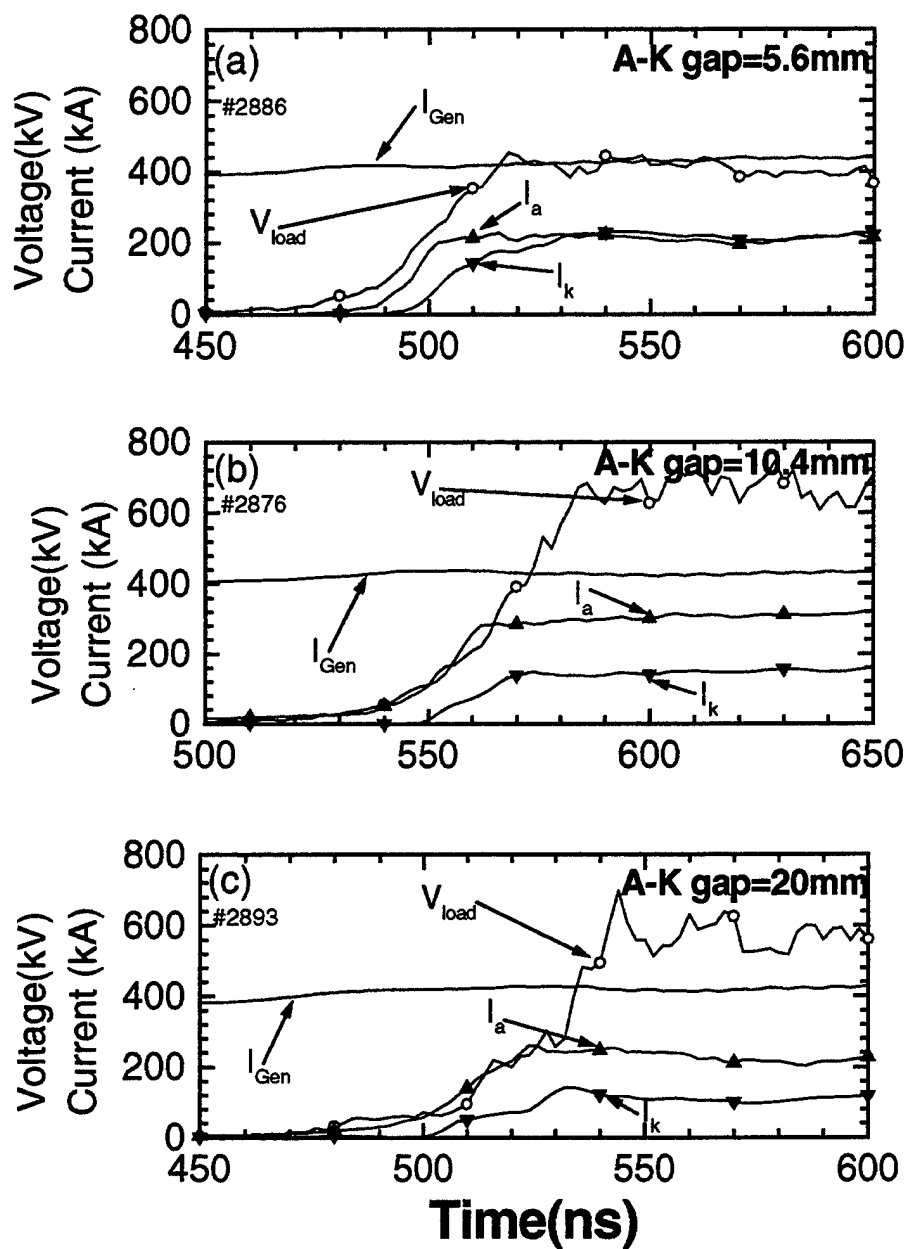


Fig. 25: Load anode current, load cathode current, and load voltage traces for three different A-K gap settings on Hawk in the short POS-to-load configuration.

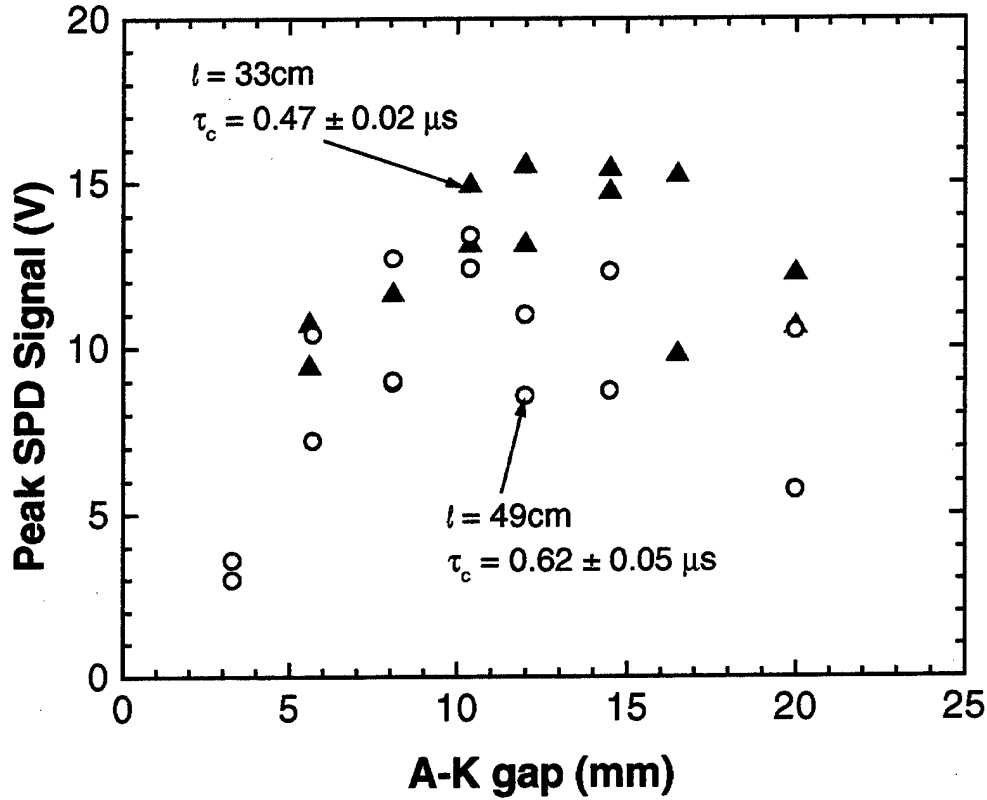


Fig. 26: Peak scintillator photodiode signal plotted versus A-K gap for both the long (open circles) and short (filled triangles) POS-to-load configurations.

where $\gamma (= 1 + eV_L/mc^2)$ is the ratio of the electron mass to its rest mass, V_L is the load (diode) voltage, e is the magnitude of the electron charge, m is the electron rest mass, R_c is the cathode radius, Δ is the diode A-K gap, and I_L is the load (diode) current (presumably I_{k2} and I_k for the long and short POS-to-load configurations, respectively). Rearranging Eq.(1), the load impedance is therefore given by:

$$Z_L = \frac{V_L}{I_L} = \frac{\Delta}{(1.6)(8500)R_c} \left[\frac{mc^2}{e} \right] \left[1 + 2 \left(\frac{mc^2}{eV_L} \right) \right]^{-1/2} \cong 38 \frac{\Delta}{R_c} \left[1 + \frac{1}{V_L^{(MV)}} \right]^{-1/2} \quad (2)$$

where $V_L^{(MV)}$ is the load voltage in units of MV. A-K gap closure has not been included in Eq.(2). To account for gap closure, Δ in Eq.(2) is replaced with an effective gap, $\Delta_{eff} = \Delta - vt$, where v is the speed at which the anode and cathode surface plasmas in the diode close the gap, and t is time after POS opening.

A series of Hawk shots was performed in which the diode impedance was varied by adjusting the A-K gap for a fixed conduction time. Diode impedances were calculated as the diode voltage (measured with the wire voltmeter) divided by the cathode load current (the average of the two cathode B-dot current monitors near the load). This method of

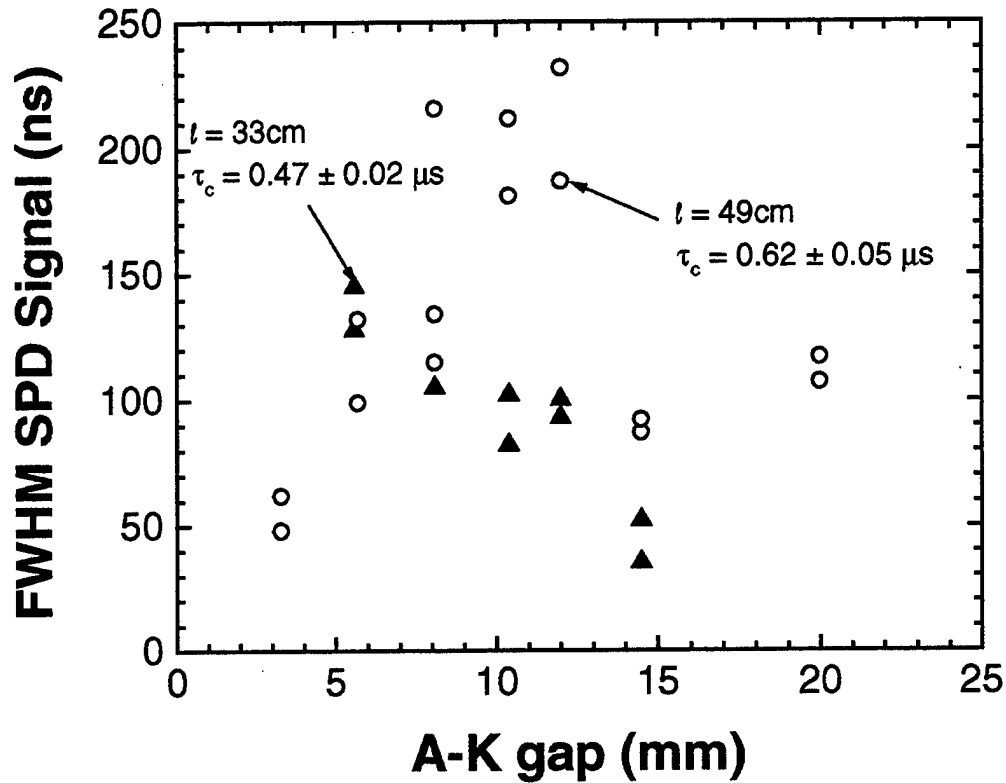


Fig. 27: Full width at half maximum for the scintillator photodiode signal versus A-K gap for both the long (open circles) and short (filled triangles) POS-to-load Hawk configurations.

determining diode impedance differs from previous Hawk experiments^{1,7,8} in which cathode current measurements were not available, and consequently anode current was used to determine diode impedance.

Because diode impedance is varied by adjusting the diode A-K gap prior to each shot, it is worthwhile to compare the impedance from Eq.(2) for a given A-K gap with the measured diode impedance at the time of peak power. This comparison is shown in Fig. 29. Impedances from the A-K gap scan described in Sec. 3.2 are plotted for both the long and short POS-to-load configurations. The solid line is a linear fit to the expected diode impedance from Eq.(2) based on the short POS-to-load data and assuming a gap closure rate of 2 cm/ μ s. As can be seen in Fig. 29, the results of Eq.(2), adjusted for gap closure, agree with the measured diode impedance at peak power. For A-K gaps less than 2 mm, diode impedance is zero because the gap is shorted by the expanding anode and cathode surface plasmas.

Measured and predicted diode impedances at the time of peak load power are plotted versus conduction time in Fig. 30(a) and (b) for an A-K gap of 10.4 mm. The predicted diode impedance is determined from Eq.(2) adjusting for gap closure. For both POS-to-load configurations, the predicted diode impedance remains fairly constant (between 4 and 5 Ω) over the range of conduction times used in these experiments. For the long POS-to-load configuration, the measured diode impedance shows a fair amount of scatter, but is always greater than or equal to the predicted diode impedance. For the

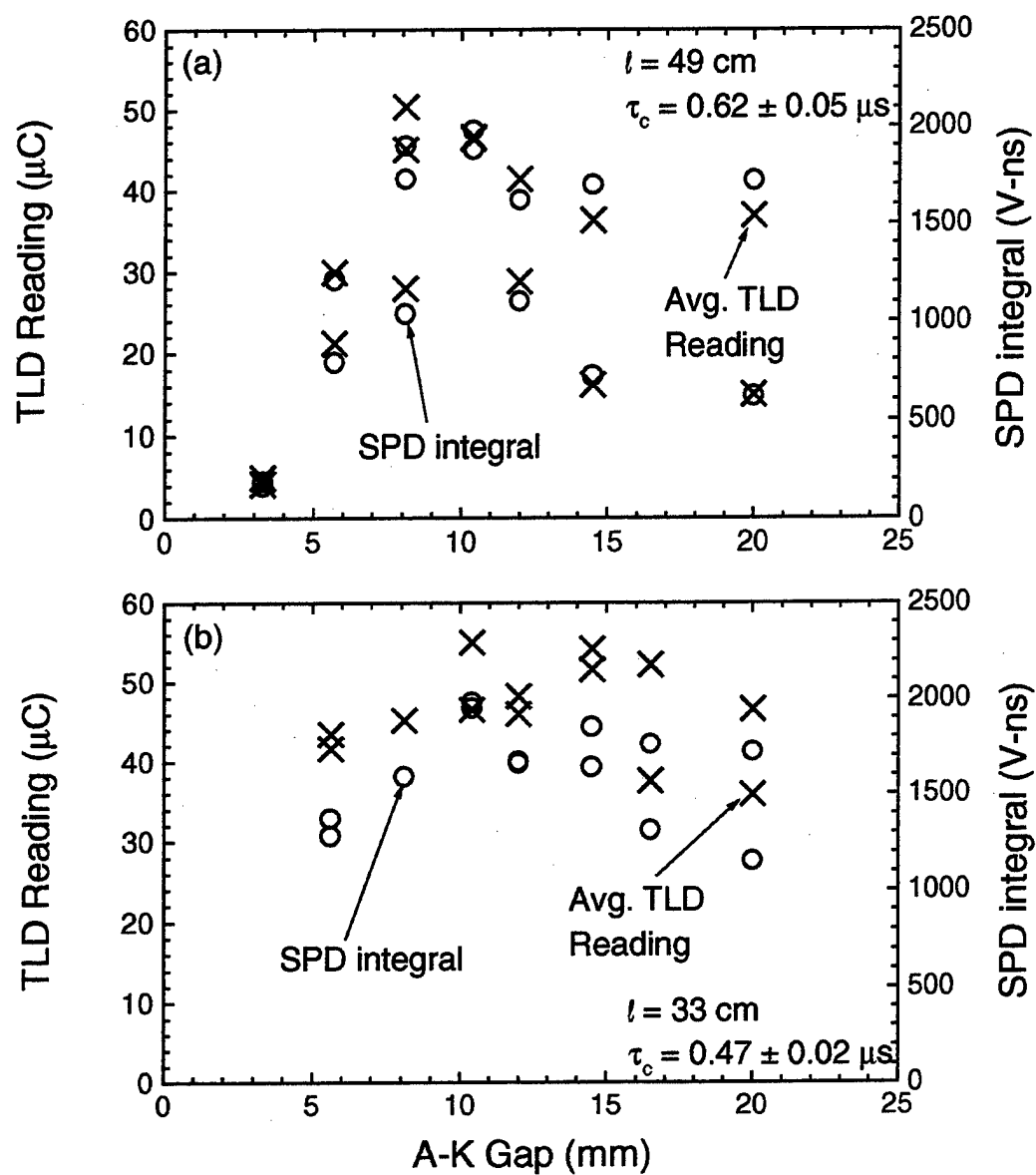


Fig. 28: Integral of the scintillator photodiode (SPD) signal (open circles) and the average TLD reading (crosses) versus A-K gap for (a) the long POS-to-load configuration and (b) the short POS-to-load configuration.

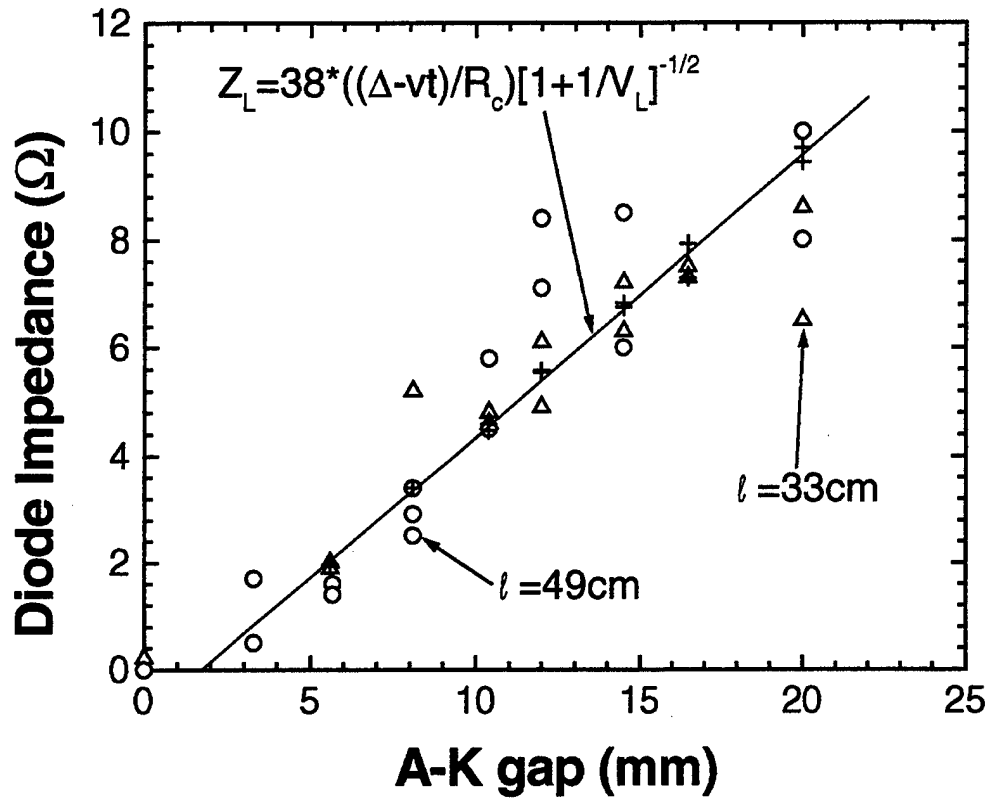


Fig. 29: Diode impedance at peak power versus A-K gap for both the short (triangles) and long (circles) POS-to-load configurations. The solid line represents a linear best fit to the calculated impedance (crosses) based on critical current.

short POS-to-load configuration, the measured diode impedance is equal to the predicted impedance for conduction times less than 0.5 μs , while the measured impedance is significantly lower than the predicted impedance ($\sim 2 \Omega$ versus $\sim 4 \Omega$) for conduction times greater than 0.5 μs . It is interesting to note in Fig. 30(b) that for the short POS-to-load configuration, the measured diode impedance drops abruptly at a conduction time of approximately 0.5 μs . This time corresponds to the conduction time after which: a) a sharp drop in diode voltage and a sharp rise in load anode current are observed [see Fig. 8(b)]; b) the pinched-beam behavior degrades [see Fig. 16]; c) the peak photodiode signal decreases [see Fig. 17]; and d) the Faraday cup signal increases sharply [see Fig. 20]. This accumulated evidence suggests that the diode impedance in the short POS-to-load configuration is influenced by POS plasma reaching the load when $\tau_c > 0.5 \mu\text{s}$.

Further evidence that plasma reaching the load in the shorter POS-to-load configuration influences diode behavior is shown in Fig. 31. Impedance time histories for several different conduction times with a 10.4-mm load A-K gap in both the short and long POS-to-load configurations are compared. In the long POS-to-load configuration, Fig. 31(a), the impedance decreases at switch opening to a characteristic value determined by the diode A-K gap (~ 3 to 5Ω based on Fig. 29), and this impedance is

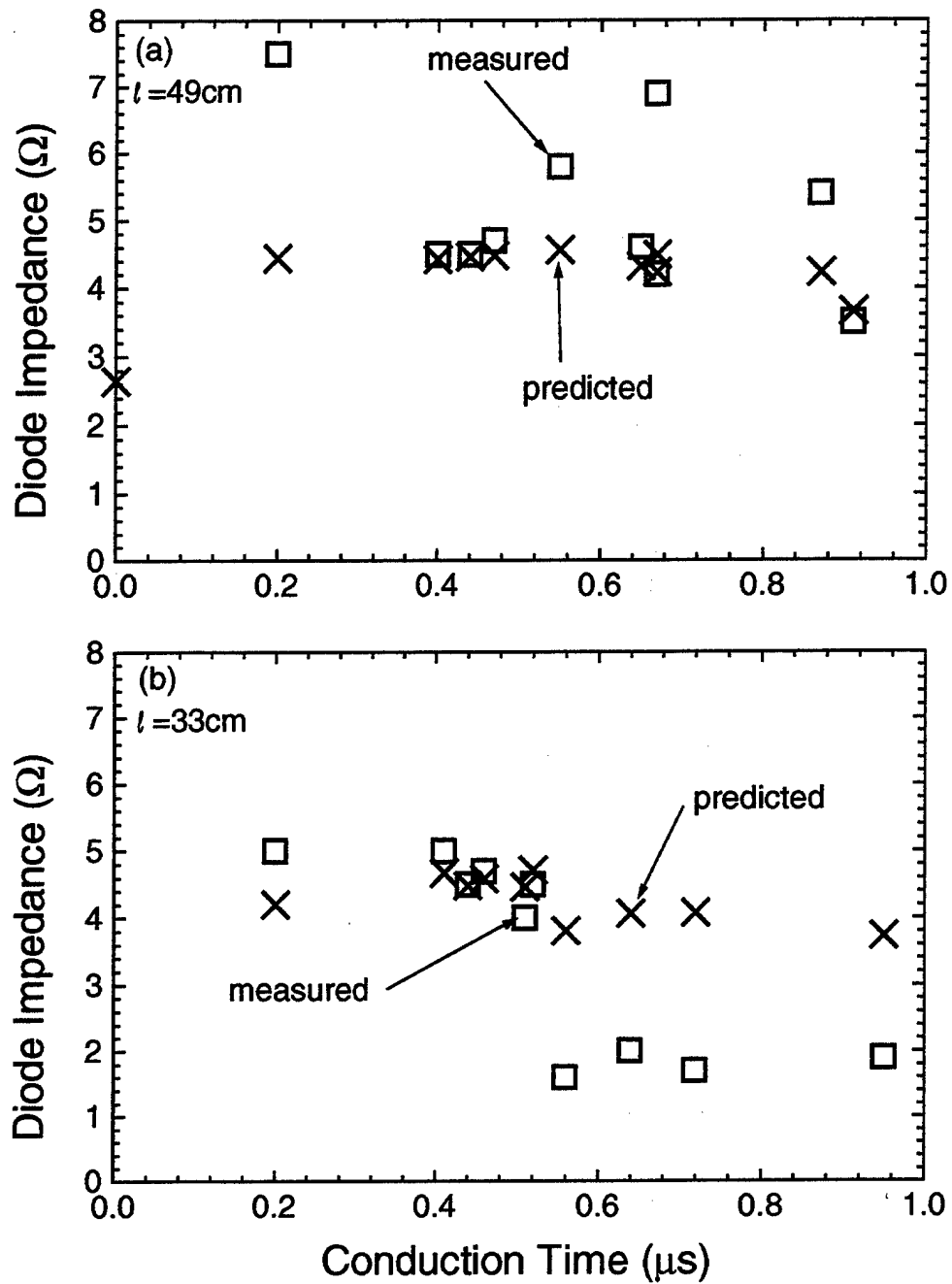


Fig. 30: Measured and predicted diode impedance versus conduction time for (a) the long POS-to-load configuration and (b) the short POS-to-load configuration. The diode A-K gap was 10.4 mm.

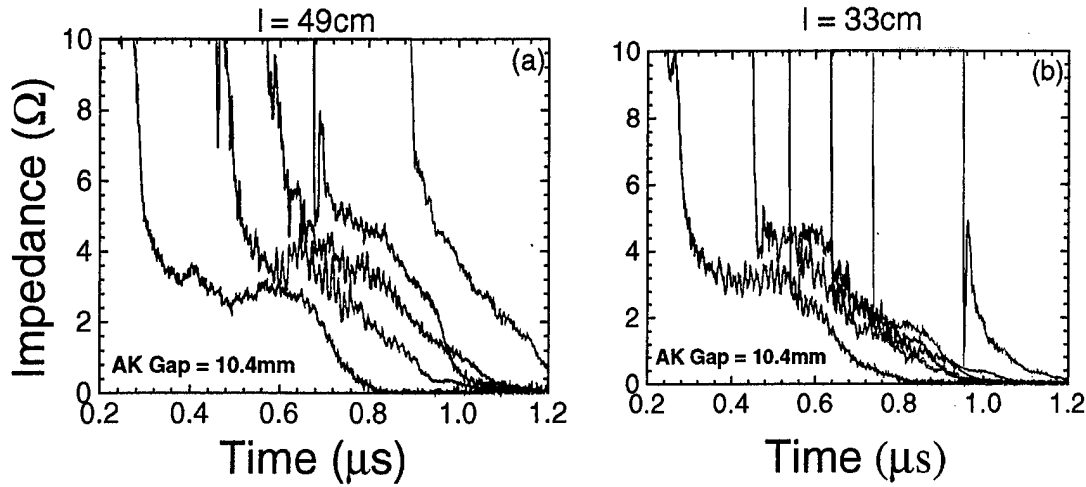


Fig. 31: Impedance histories for five different conduction times in (a) the long POS-to-load configuration, and (b) the short POS-to-load configuration.

maintained during a plateau phase which lasts for a few hundred ns. The duration of the plateau phase gradually decreases as the conduction time is increased. For conduction times of $\sim 1 \mu\text{s}$, there is no clear plateau phase. The short POS-to-load configuration, shown in Fig. 31(b), has a very different behavior. As the conduction time is increased beyond 500 ns, the diode impedance decreases at switch opening to a value below that determined by the A-K gap. Furthermore, the duration of the plateau in diode impedance is less than 100 ns, much shorter than the duration for the long POS-to-load case. This suggests that plasma affects the load sooner in the short POS-to-load case. The exact mechanism by which plasma reduces the diode impedance is not clear from these data. This question will be studied in the future. Although plasma appears to influence the diode impedance in the short POS-to-load case, the impedance behavior for this case does not resemble that of a plasma-filled diode (initial impedance of zero, followed by increasing impedance) as has been observed in previous flashboard POS experiments.⁸

Fig. 32 shows load voltage and load anode and cathode current measurements as a function of diode impedance at the time of peak load power. Fig. 32(a) shows data for the long POS-to-load configuration, while Fig. 32(b) shows data for the short POS-to-load configuration. As a result of the linear relationship between diode impedance and A-K gap shown in Fig. 29, the trends are the same as observed in Fig. 21. In the load-limited region, to the left of the dashed vertical line in both figures, the load voltage increases with increasing impedance, reaching approximately 600 kV for the long POS-to-load configuration and 750 kV for the short POS-to-load configuration. In the switch-limited region, to the right of the dashed vertical line in both figures, the load voltage is approximately constant for both POS-to-load configurations. In both the switch-limited and load-limited regimes, the load anode current decreases with increasing load impedance in the long POS-to-load configuration [Fig. 32(a)], while it remains approximately constant for the short POS-to-load configuration [Fig. 32(b)]. In both the switch-limited and load-limited regions, the load cathode current decreases with increasing impedance. For the 5-cm radius cathode, the critical impedance at which diode behavior changes from load-limited to switch-limited, 4 to 5 Ω , is higher than reported in previous work,^{1,7-9} 1.5 to 2 Ω . This is because the load cathode current, rather than the load anode current, was used to define the diode impedance.

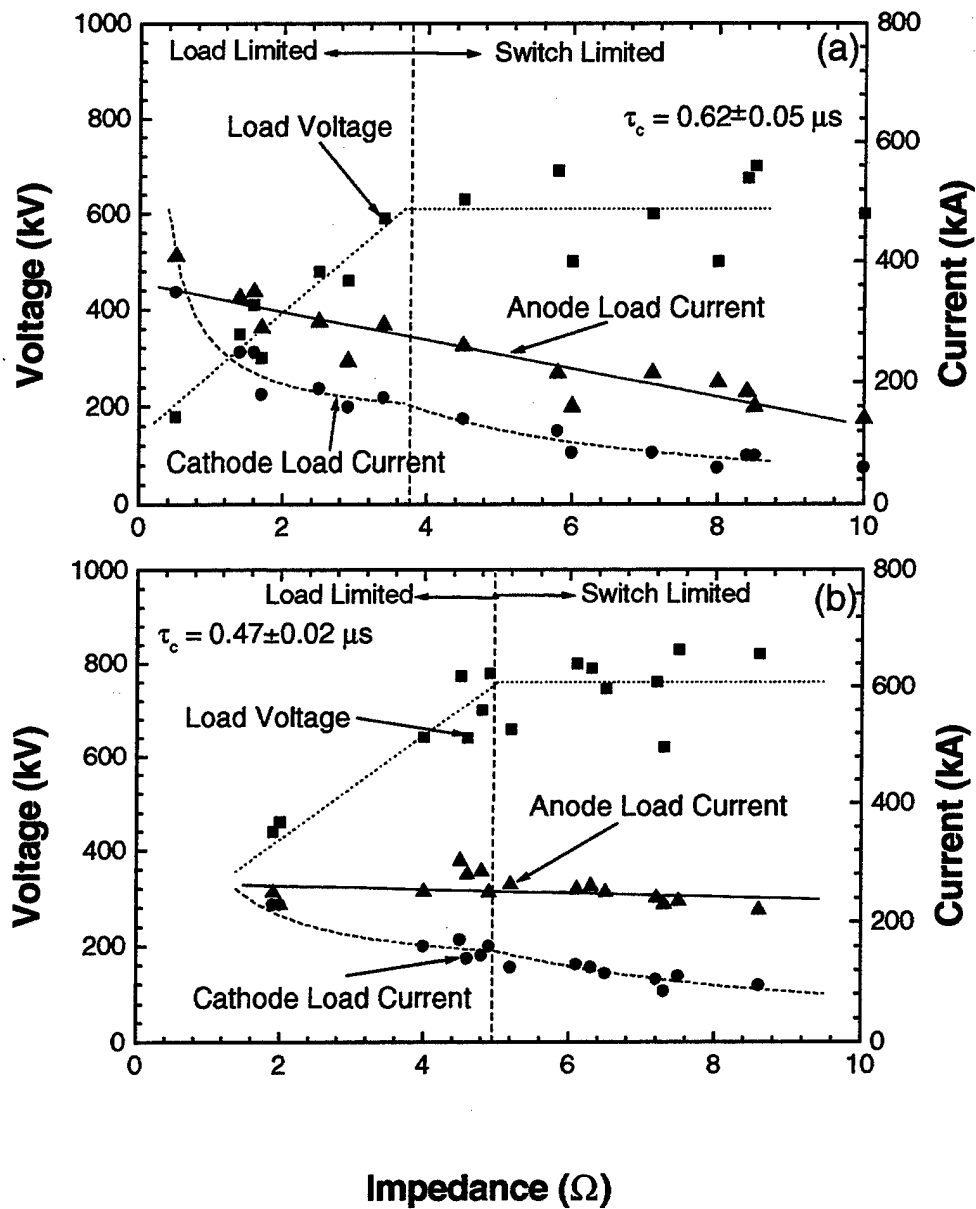


Fig. 32: Load voltage, cathode current, and anode current plotted versus diode impedance for (a) the long POS-to-load configuration and (b) the short POS-to-load configuration.

$$\text{Model: } \text{brems} = \alpha * I_{a2} * V_L^\beta \quad \alpha = 1.93\text{E-}18 \quad \beta = 2.34 \quad \chi^2 = 0.45331$$

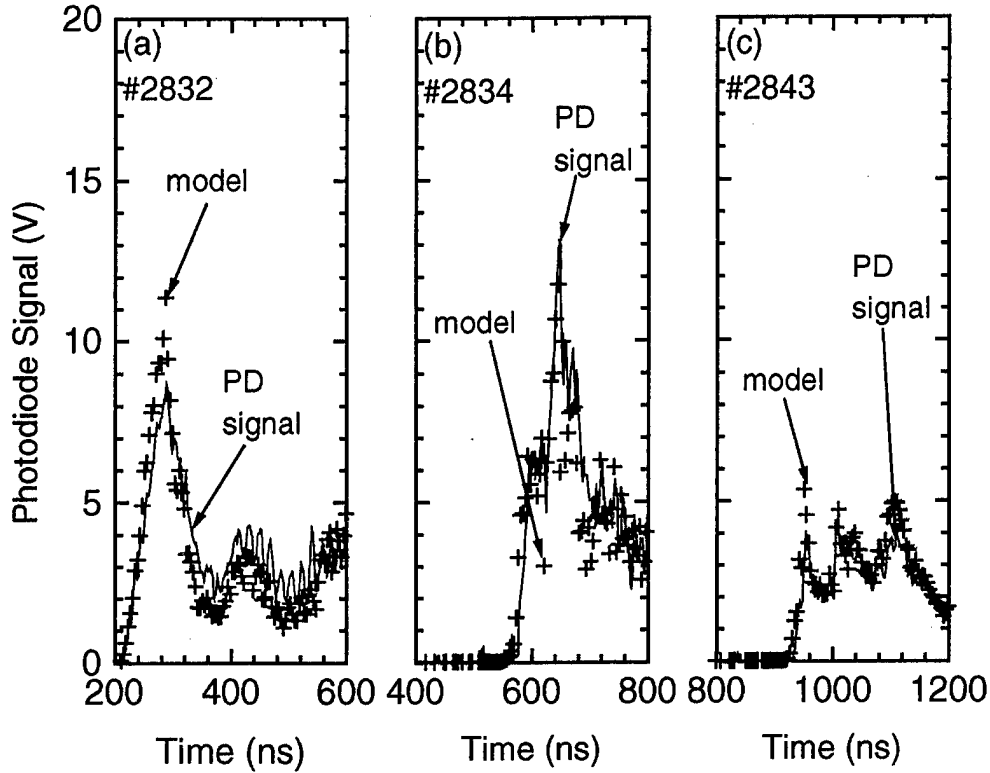


Fig. 33: Photodiode signal (solid line) shown together with nonlinear fit to the form $\alpha I_L V_L^\beta$ (crosses) for the long POS-to-load configuration at three different conduction times.

4.2 Bremsstrahlung Dose-voltage dependence

In Sec. 3.1.2, it was observed that bremsstrahlung production by this e-beam diode is not proportional to the diode power, but depends more strongly on the diode voltage. The exact relationship between diode voltage and bremsstrahlung production has been the subject of much research.^{21,22} In general, the on-axis dose rate, $\dot{\gamma}$, for a narrow e-beam measured 1 m downstream from the diode has been expressed as: $\dot{\gamma} \propto I_L V_L^\beta$, where V_L is the diode voltage, I_L is the diode current, and β is between 2.65 and 2.8 for diode voltages greater than 1 MV. For this work however, the maximum diode voltage was approximately 800 kV, so the previously determined scaling may not apply. Data for both the long and short POS-to-load configurations were fit to an expression of the form $\dot{\gamma} = \alpha I_L V_L^\beta$ where α and β were independent parameters to be determined. The results are shown in Fig. 33 and Fig. 34 for the long and short POS-to-load configurations, respectively. Reasonable fits ($\chi^2 < 1$) to the measured SPD signals are achieved for three different conduction times. The dose-voltage scaling for these low voltage measurements is significantly weaker than the dose-voltage reported for voltages greater than 1 MV. For the long POS-to-load configuration (Fig. 33), the dose

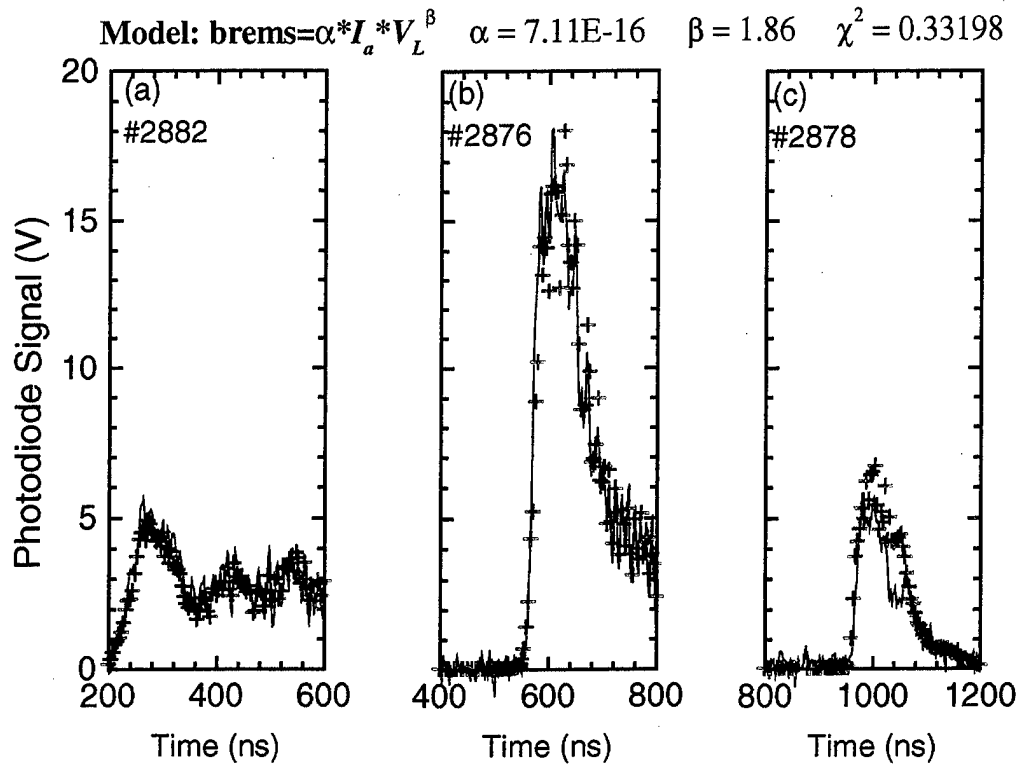


Fig. 34: Photodiode signal (solid line) shown together with nonlinear fit to the form $\alpha I_a V_L^\beta$ (crosses) for the short POS-to-load configuration at three different conduction times.

rate scales as $V_L^{2.3}$, while for the short POS-to-load configuration (Fig. 34), the dose rate scales as $V_L^{1.9}$.

There are a number of possible explanations for the difference in dose-voltage scaling between the short and long POS-to-load configurations. First, these dose-voltage scalings were determined from an empirical fit to the data assuming that the entire load anode current contributes to bremsstrahlung production in the load. While this assumption produced reasonable fits to the data as shown in Fig. 33 and Fig. 34, it may not be accurate. Thus, the difference in dose-voltage scaling between the long and short POS-to-load configurations may result from a different fraction of the load anode current contributing to bremsstrahlung production for the different POS-to-load distances. The portion of the current that is non-radiation-producing ion current has not been accounted for either. Another factor that affects the dose-voltage dependence for e-beam diodes is the incident angle of the electrons striking the tantalum anode. This angle may be affected by the proximity of the POS to the load, resulting in a different dose-voltage scaling for different POS-to-load distances. A detailed investigation of these different factors and their affect on the dose-voltage scaling is beyond the scope of this study, and is left for future work.

4.3 Current losses

Downstream current measurements provide a quantitative means of comparing current losses between the long and short POS-to-load configurations and validating the

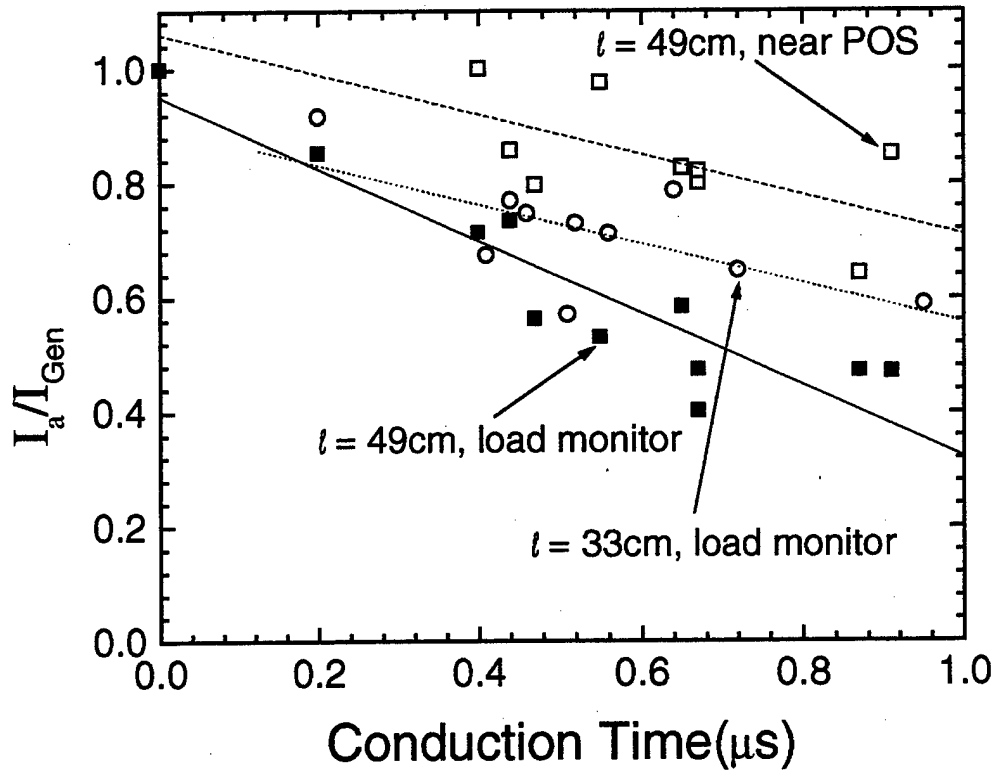


Fig. 35: Anode-current-to-generator-current ratio at the time of peak power versus conduction time for both the long (filled and open squares) and short (open circles) POS-to-load configurations. The diode A-K gap is fixed at 10.4 mm.

behavior suggested by the pinhole camera photographs in Fig. 14 and Fig. 15. The ratios of the downstream anode currents to the generator current at the time of peak load power for both POS-to-load configurations are plotted in Fig. 35 as a function of POS conduction time for a fixed diode A-K gap of 10.4 mm. The same ratios are plotted in Fig. 36 as a function of diode impedance with conduction time fixed at $0.62 \pm 0.05 \mu s$ and $0.47 \pm 0.02 \mu s$ for the long and short POS-to-load configurations, respectively. In both Fig. 35 and Fig. 36, the squares (open and filled) correspond to measurements in the long POS-to-load configuration. The filled squares indicate the ratio of the anode current measured near the load to the generator current, while the open squares indicate the ratio of anode current measured just downstream of the POS (see Fig. 1) to the generator current. The open circles indicate the ratio of the anode load current to generator current in the short POS-to-load configuration. Note that the load anode current monitor in the short POS-to-load case is at the same axial distance from the POS as the monitor measuring the anode current just downstream of the POS in the long POS-to-load case. The lines shown in Fig. 35 and Fig. 36 are linear fits to the data points.

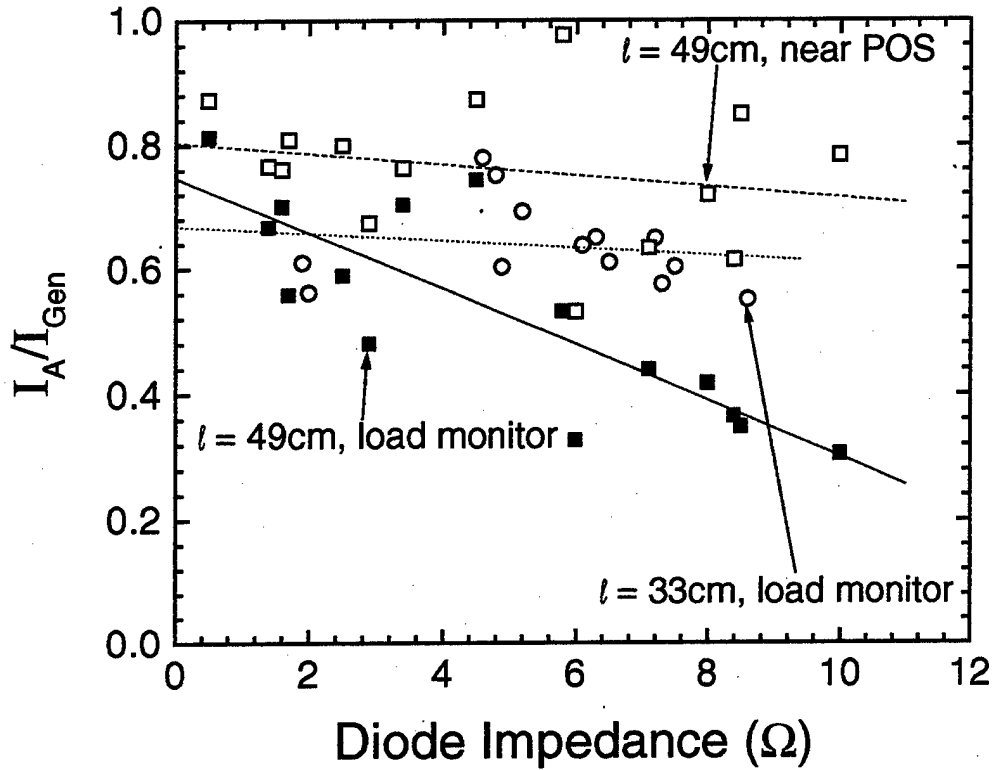


Fig. 36: Anode-current-to-generator-current ratio (at the time of peak power) versus diode impedance for both the long (filled and open squares) and short (open circles) POS-to-load configurations. Conduction times are $0.62 \pm 0.05 \mu\text{s}$ and $0.47 \pm 0.02 \mu\text{s}$ for the long and short POS-to-load configurations, respectively.

Fig. 35 shows that, for both configurations, the ratios of anode current to generator current at the time of peak power decrease as the conduction time is increased. This result is counter to what might be expected from the side-viewing pinhole camera images in Fig. 15 (in which the location where high-energy electrons begin to strike the anode moves downstream as the conduction time increases, and therefore the area for losses decreases). The ratio of anode current to generator current is seen to be greater for the short than for the long POS-to-load configuration, which is consistent with the observations from the x-ray pinhole photographs in Fig. 14. However, for the long POS-to-load configuration, the fraction of the generator current detected at the anode current monitor closest to the POS is greater than that for the short POS-to-load configuration at the same location relative to the POS.

In Fig. 36, the ratio of load anode current to generator current is seen to decrease as the diode impedance increases. The decrease in current reaching the load is steeper for the long POS-to-load configuration than for the short POS-to-load configuration, probably a result of the longer length (larger area) for losses to occur (see discussion in Sec. 3.1 and Fig. 14).

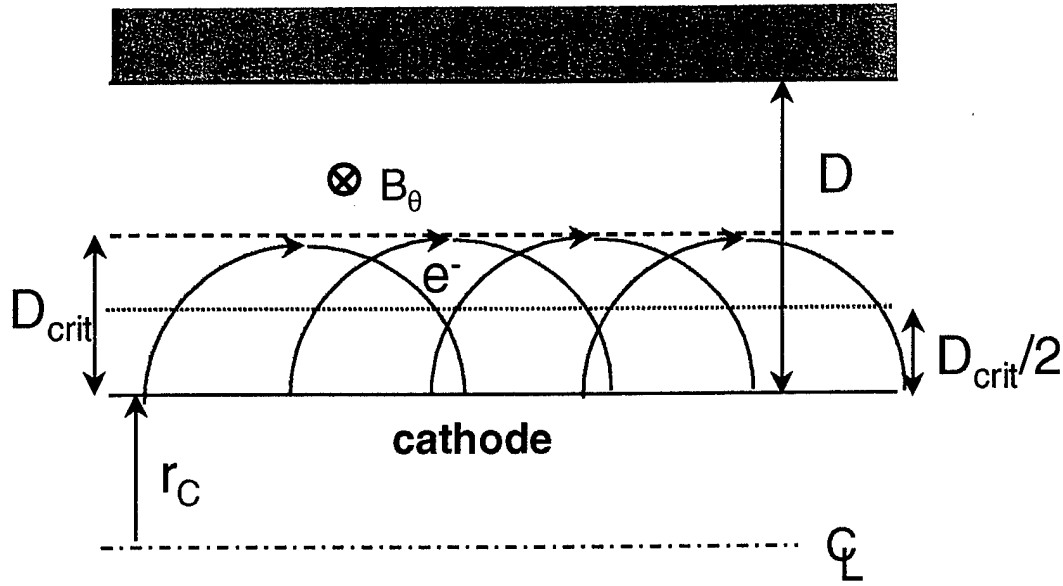


Fig. 37: Idealized illustration of the possible distribution of electrons and plasma in the gap region of a POS. B_θ is the magnetic field associated with the generator current, D is the POS gap, and D_{crit} is the critical gap for magnetic insulation.

4.4 Flow impedance and the POS gap

The significance of vacuum electron flow in the POS can be estimated from the flow impedance.²³ The POS "vacuum" impedance is modeled by assuming that a space-charge-limited electron sheath having a thickness equivalent to the electron Larmour radius forms at the cathode (see Fig. 37). This thickness has been referred to as the effective gap for magnetic insulation,¹ and will be called the critical switch gap, D_{crit} , in what follows. The critical switch gap represents the minimum gap required for magnetically insulated electron flow. The critical current formula derived from the relativistic, single particle description of electron flow [Eq.(1)] can be rearranged to obtain the following expression for D_{crit} ^{1,7}

$$D_{crit} = (1.6) * 8500 * (\gamma_{POS}^2 - 1)^{1/2} * \frac{R_c}{I_{Gen}} \quad (3)$$

where $\gamma_{POS} = 1 + eV_{POS}/mc^2$, V_{POS} is the POS voltage, R_c is the cathode radius, and I_{Gen} is the generator current. Mendel has shown²⁴ that the flow impedance for this coaxial gap is equivalent to the vacuum impedance for a vacuum gap bounded by the anode plasma edge, R_a , and the centroid of the electrons in the cathode sheath, \bar{R}_e :

$$Z_f = 60 \ln(R_a / \bar{R}_e). \quad (4)$$

For a uniformly distributed charge in a thin sheath, the centroid radius can be approximated as $\bar{R}_e = R_c + D_{crit} / 2$. The radial location of the anode plasma edge is $R_a = R_c + D$, where D represents the effective size of the POS gap. Substituting the expressions for \bar{R}_e and R_a into Eq.(4) and assuming $D_{crit}/2R_c \ll 1$ yields

$$Z_f \cong 60 \ln \left[\left(1 - \frac{D_{crit}}{2R_c} \right) \left(1 + \frac{D}{R_c} \right) \right] = 60 \ln \left(1 + \frac{D}{R_c} - \frac{D_{crit}}{2R_c} - \frac{D_{crit}D}{2R_c^2} \right). \quad (5)$$

Retaining terms up to first order in D/R_c , the flow impedance may be approximated as:

$$Z_f \approx 60 \left[\frac{D - D_{crit}/2}{R_c} \right]. \quad (6)$$

Mendel has also shown^{23,24} that pressure balance in the electron sheath can lead to a relationship for Z_f in terms of measured currents and voltages:

$$Z_f = \frac{V_{POS}}{(I_{au}^2 - I_{kd}^2)^{1/2}}. \quad (7)$$

where I_{au} is the anode current just upstream of the POS (which can be taken as I_{Gen} for this experiment), and I_{kd} is the cathode current just downstream of the POS (equivalent to I_{kl} in the long POS-to-load configuration or I_k in the short POS-to-load configuration). Applying the experimental results obtained in this work, Eq.(6) can be rearranged to determine the effective POS gap,

$$D = \frac{D_{crit}}{2} + \frac{R_c}{60} Z_f \quad (8)$$

where D_{crit} is determined from Eq.(3) and Z_f is determined from Eq.(7).

4.4.1 POS gap and flow impedance variation with conduction time

Fig. 38 shows the critical switch gap, D_{crit} , and the experimentally inferred switch gap, D , plotted versus conduction time for the long POS-to-load configuration [Fig. 38(a)] and for the short POS-to-load configuration [Fig. 38(b)] with a fixed 10.4 mm diode A-K gap. D_{crit} decreases with increasing conduction time for both configurations. This reduced D_{crit} reflects better magnetic insulation provided by the higher generator current and associated azimuthal self-magnetic field, while the load and switch voltages are decreasing. One difference between the results shown in Fig. 38 and previous experiments²⁵ is that here the POS gap decreases non-linearly with conduction time (as opposed to linearly in the previous work), and the gap appears to approach asymptotically a value of ~1.5 mm at long conduction times. At optimum conduction time, the gap is about 3 mm. The switch gaps calculated for both the long and short POS-to-load configurations follow the same asymptotically decreasing curve (shown in Fig. 38(a) and (b)) at conduction times less than 0.5 μ s. For the shorter POS-to-load configuration, a sudden decrease in the critical switch gap occurs at a conduction time slightly greater than the optimum. This result is consistent with reduced diode impedance (due to plasma in the load) causing the diode behavior to force the POS into the load-limited regime [See also Figs. 8(b), 13(c), 16, 17, 19(b), 20, 30(b), and 31(b)].

4.4.2 POS gap and flow impedance variation with load impedance

A comparison of the effective switch gap, D , with the critical gap for magnetic insulation, D_{crit} , over a range of diode impedances is shown for the long POS-to-load configuration in Fig. 39(a). The same plot for the short POS-to-load configuration is

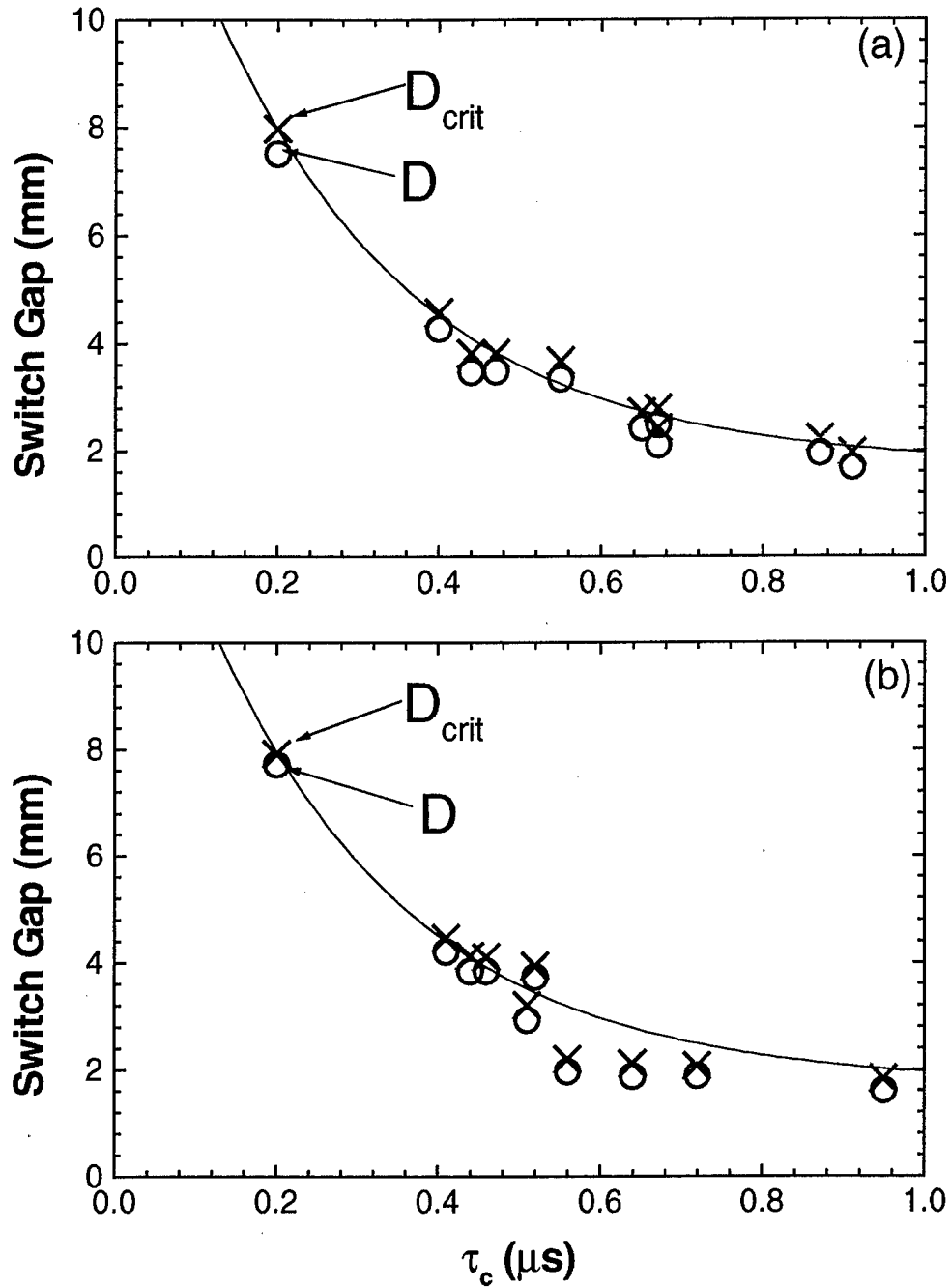


Fig. 38: Critical POS Gap (crosses) and experimentally inferred POS gap (open circles) versus conduction time for (a) the long POS-to-load configuration and (b) the short POS-to-load configuration. The diode A-K gap was fixed at 10.4 mm.

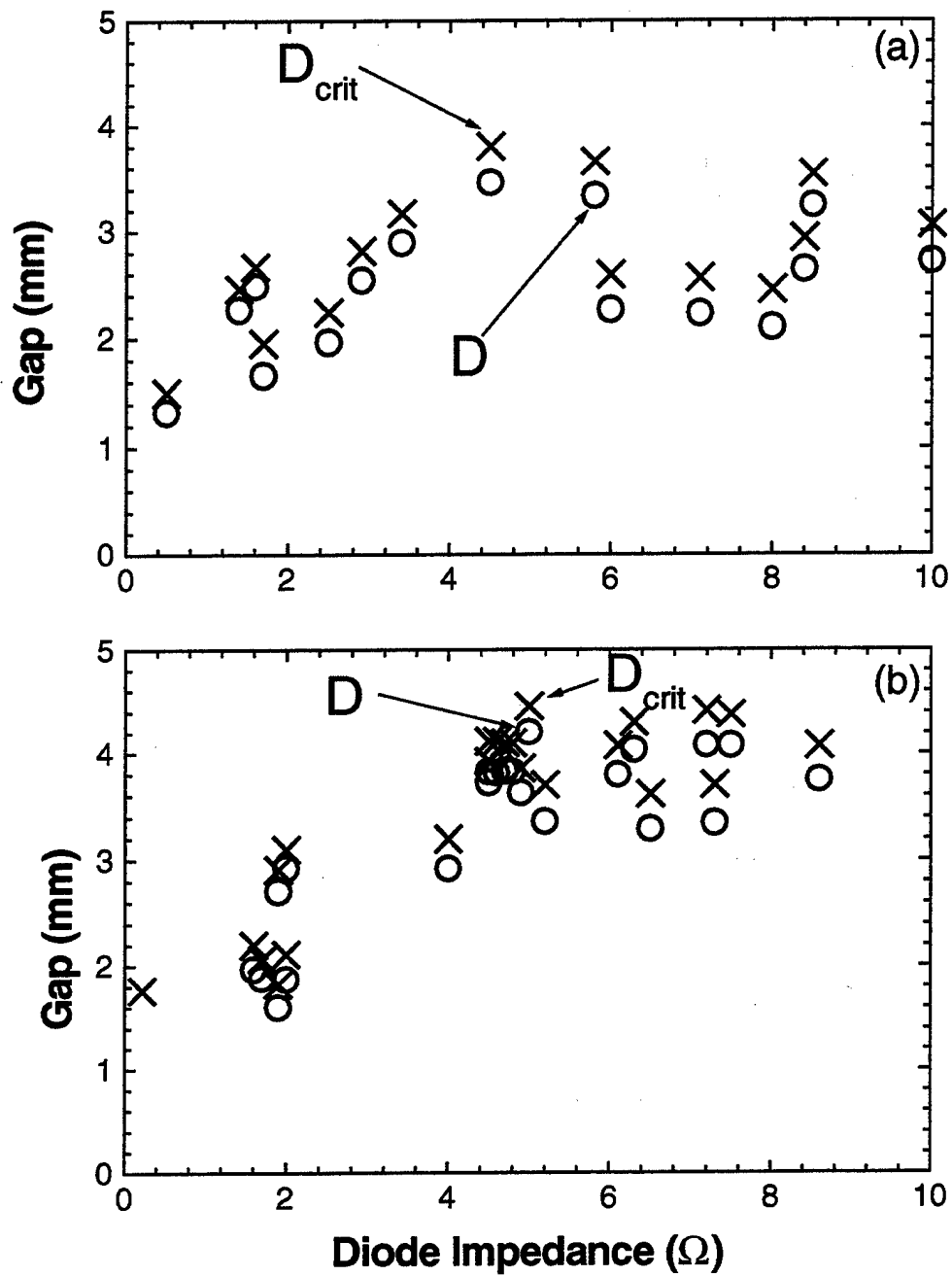


Fig. 39: Critical POS Gap (crosses) and experimentally inferred POS gap (open circles) versus A-K gap for (a) the long POS-to-load configuration, and (b) the short POS-to-load configuration. Conduction times are $0.62 \pm 0.05 \mu s$ and $0.47 \pm 0.02 \mu s$ for the long and short POS-to-load configurations, respectively.

shown in Fig. 39(b). For these data the conduction time was fixed at $0.62 \pm 0.05 \mu\text{s}$ and $0.47 \pm 0.02 \mu\text{s}$ for the long and short POS-to-load configurations, respectively. In the short POS-to-load configuration, the effective gap is equal to (and tracks with) the critical gap. For $Z_L > Z_L^*$, i.e. diode impedance greater than about 4.5Ω (the switch-limited regime), the gap is constant as previously observed.^{1,7-9} However, when $Z_L < Z_L^*$, i.e. the diode impedance is less than about 4.5Ω (the load-limited regime), both the critical gap and the effective gap are reduced, and in fact, the effective gap remains equal to the critical gap even in the load-limited regime. The reduction of the critical gap in the load-limited regime is a result of the lower diode voltage and consequently lower opening-switch voltage. The reduction of the effective gap in the load-limited regime implies that the load impedance influences POS behavior such that the POS gap remains critically insulated. Until now, the size of the effective POS gap in the load-limited regime was only known to be $\geq D_{crit}$.¹ The data for the long POS-to-load configuration is similar but exhibits greater scatter.

The flow impedance can be compared with the vacuum impedance of the critical POS gap. In Fig. 40(a), such a comparison is made for the long POS-to-load configuration, while in Fig. 40(b), the same comparison is made for the short POS-to-load configuration. It is seen in both figures that the flow impedance is half the vacuum impedance associated with the critical POS gap. This was predicted theoretically for a POS in the switch-limited regime.²⁶ This result is significant as it indicates that the POS gap and the flow impedance are influenced by diode impedance in the load-limited regime as well.

4.4.3 Flow impedance variation with inferred gap

Scans in conduction time and diode impedance for both POS-to-load distances indicate that the inferred gap is always approximately equal to the critical gap for magnetically insulated electron flow. Based on this, the centroid of the electron sheath should be located at the midpoint of the inferred POS gap, and the flow impedance should therefore scale as half the vacuum impedance of the inferred POS gap [see Eq.(8)]. This is demonstrated in Fig. 41 in which the flow impedance is plotted versus the inferred POS gap for all Hawk conditions included in this report. Two lines have been plotted on the graph. One of these lines corresponds to well insulated flow in which $D \gg D_{crit}$ such that the flow impedance should scale as the full vacuum impedance of the inferred POS gap, $60D/R_c$ [$D_{crit} = 0$ in Eq.(8)]. The other line corresponds to fully saturated flow in which electrons fill the gap and the flow impedance should scale as half the vacuum impedance of the inferred POS gap, $30D/R_c$ [$D_{crit} = D$ in Eq.(8)]. As can be seen in Fig. 41, the Hawk data all falls along the line corresponding to saturated electron flow. This implies that the switch-load coupling is self-regulated to maintain saturated electron flow in the POS.

4.5 Conduction time scaling

It was mentioned in Sec. 2.3 that the conduction time shows a sudden increase when the delay between the doghouse and Hawk marx bank triggers is between approximately $2.8 \mu\text{s}$ and $3.0 \mu\text{s}$. This sudden conduction time increase occurs at about the peak of the third half-cycle of the doghouse current, and suggests a sudden increase in the plasma mass in the switch at this time, based on the MHD model for the POS conduction phase.^{1,2,27} In this section, the MHD model is derived, and the implications to the observed conduction time behavior are discussed.

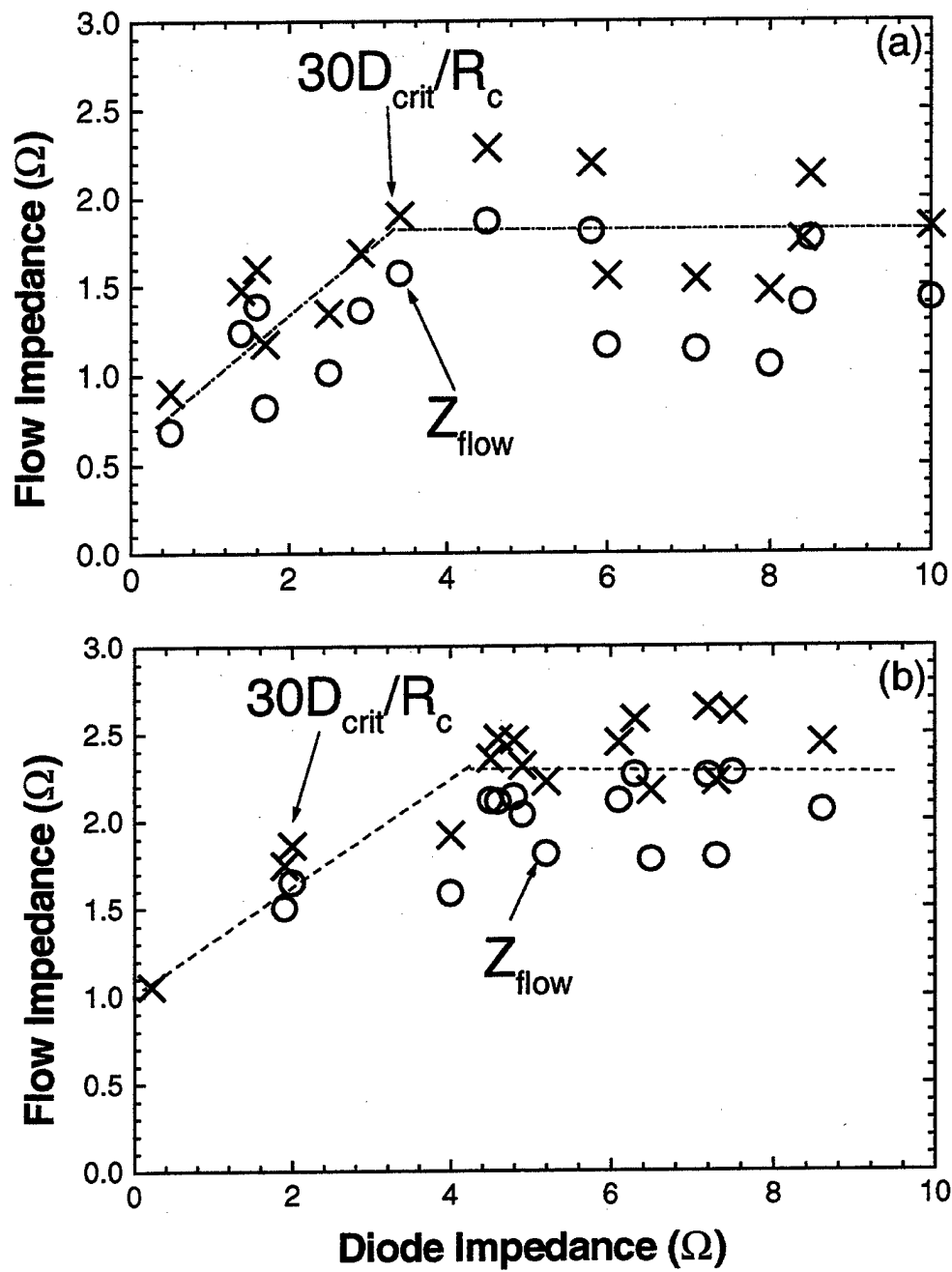


Fig. 40: POS flow impedance (open squares) versus diode impedance compared with half the vacuum impedance of the critical POS gap (filled squares) for the long POS-to-load configuration. Conduction times are $0.62 \pm 0.05 \mu s$ and $0.47 \pm 0.02 \mu s$ for the long and short POS-to-load configurations, respectively.

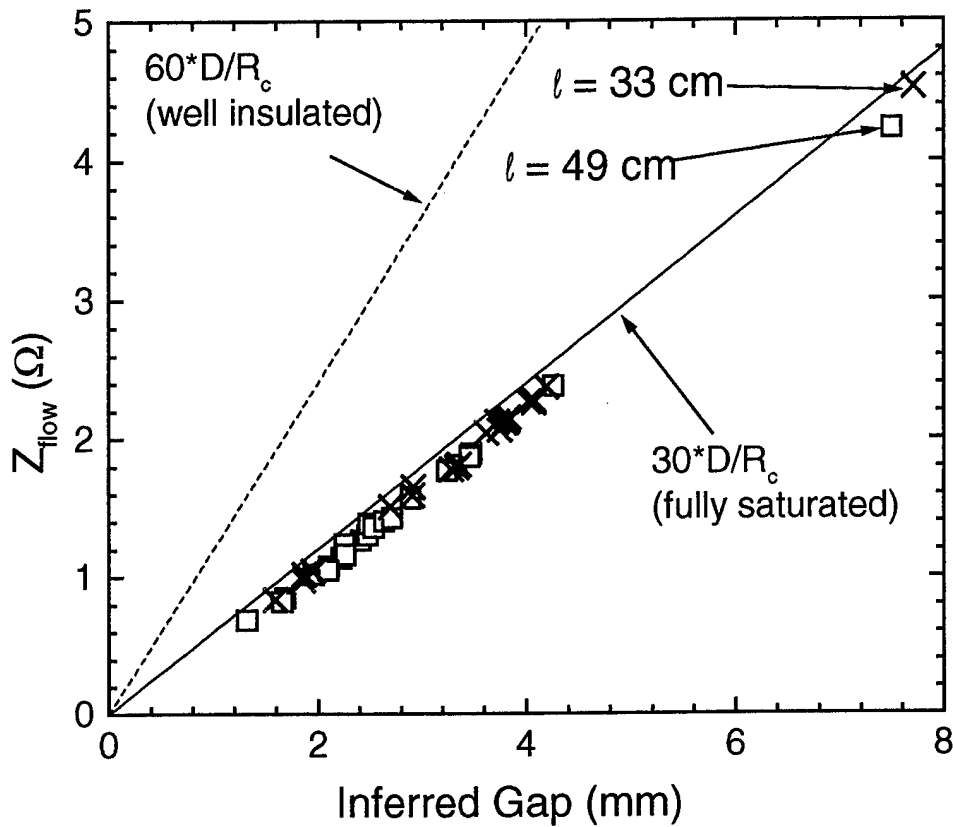


Fig. 41: Flow impedance for both the long (open squares) and short (crosses) POS-to-load configurations plotted versus the inferred POS gap. The solid line represents the predicted flow impedance scaling for fully saturated flow, while the dashed line represents the predicted flow impedance scaling for well insulated flow.

4.5.1 MHD model for POS conduction scaling

In this model, we consider the center-of-mass displacement of a plasma cylinder of thickness Δr (\ll POS A-K gap) and length l_o at radius r (the radial location in the plasma where opening first occurs).^{1,6,28} By Newton's second law, the axial magnetic force, F , on this thin cylinder is:

$$F = \frac{B^2}{2\mu_o} 2\pi r(\Delta r) = \frac{2\pi r(\Delta r) l_o m_i n_e}{Z} \frac{d^2 z}{dt^2}. \quad (9)$$

In this expression, B is the azimuthal magnetic field at radius r , μ_o ($= 4\pi \times 10^{-7}$ H/m) is the permeability of free space, m_i is the ion mass averaged over species, n_e is the electron density in the plasma annulus, and Z is the ion charge state averaged over species and assumed constant during conduction (no ionization). Thus, $n_e = Zn_i$ (quasineutrality). Recognizing that $B = \mu_o J_{\text{Gen}} / 2\pi r$, Eq.(9) can be integrated twice to yield

$$\frac{8\pi^2 r^2 l_o m_i n_e (\Delta z)}{\mu_o Z} = \iint I^2 dt^2. \quad (10)$$

Opening can begin after the plasma annulus center-of-mass has been displaced to the load end of the POS, or in other words, when $\Delta z = l_o/2$.^{1,2} Assuming a sinusoidal current waveform, $I(t) = I_{\max} \sin(\omega t)$, we can analytically evaluate the integral in the above expression from $t=0$ to $t=\tau_c$ (at which point $\Delta z = l_o/2$), leading to the following result,

$$\frac{4\pi^2 r^2 l_o^2 m_i n_e}{\mu_o Z} = \frac{I_{\max}^2}{4} \left\{ \tau_c^2 - \frac{\sin^2(\omega \tau_c)}{\omega^2} \right\} \quad (11)$$

This can be rewritten in terms of the generator current, $I_{\text{Gen}} = I_{\max} \sin(\omega \tau_c)$ as

$$\frac{4\pi^2 r^2 l_o^2 m_i n_e}{\mu_o Z} = \frac{I_{\text{Gen}}^2 \tau_c^2}{4} \left\{ \frac{1}{\sin^2(\omega \tau_c)} - \frac{1}{\omega^2 \tau_c^2} \right\} \quad (12)$$

Performing a Taylor series expansion on the quantity in brackets about $\omega \tau_c = 0$ yields

$$\frac{4\pi^2 r^2 l_o^2 m_i n_e}{\mu_o Z} = \frac{I_{\text{Gen}}^2 \tau_c^2}{4} \left\{ \frac{1}{3} - \frac{2}{3} \left(\frac{\omega^2 \tau_c^2}{15} \right) + \dots \right\} \quad (13)$$

Taking the limit of this expression as $\omega \tau_c \rightarrow 0$, and solving for the generator current yields,

$$I_{\text{Gen}}^2 = \frac{48\pi^2 r^2 l_o^2 m_i n_e}{\mu_o Z \tau_c^2}. \quad (14)$$

This result is precisely the result obtained assuming a generator current which increases linearly with time.¹ Solving this expression for the electron density yields the well-known result for electron density assuming a linearly ramping current,

$$n_e = \left(\frac{\mu_o Z}{48\pi^2 m_i n_e} \right) \frac{I_{\text{Gen}}^2 \tau_c^2}{r^2 l_o^2}. \quad (15)$$

In order to estimate the error in density associated with the approximation of linearly ramping conduction current, we must consider the higher order terms Eq.(13). For the Hawk data presented here, $0 < \omega \tau_c < \pi/2$, such that the maximum possible error in the linear approximation, found by setting $\omega \tau_c = \pi/2$, is $\epsilon_{\max} = \pi^2/30 \sim 33\%$. The maximum error drops to approximately 8% at $\omega \tau_c = \pi/4$, which corresponds to the optimum conduction time in these experiments.

4.5.2 Mass scaling on Hawk

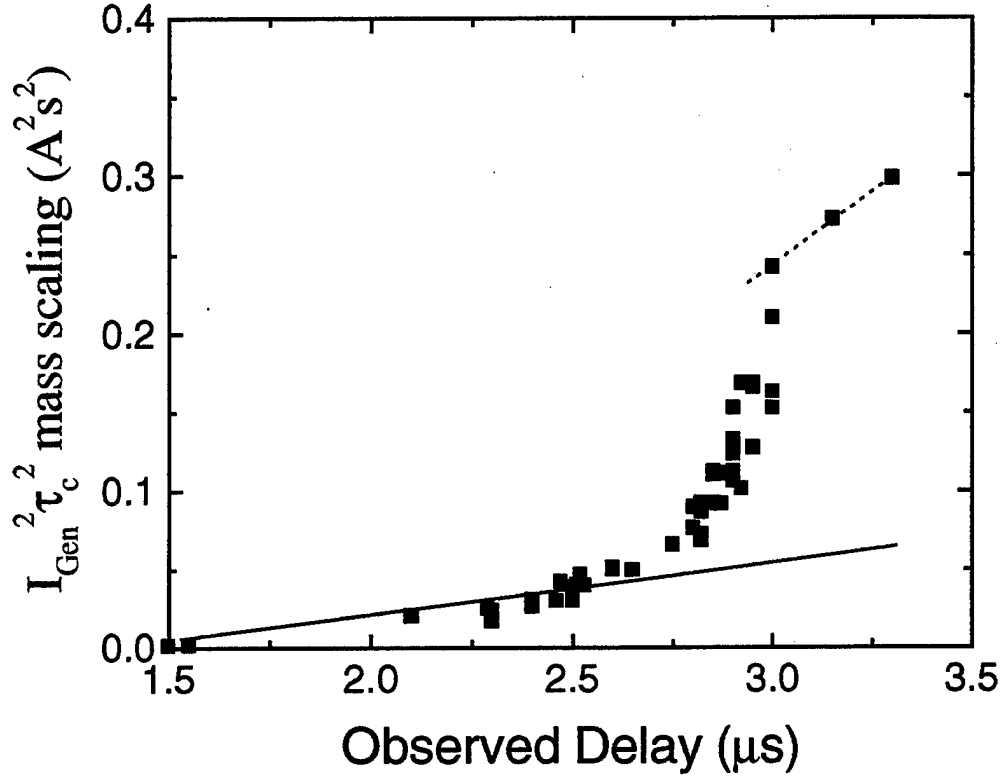


Fig. 42: Snowplow-derived POS mass versus observed delay on Hawk.

Utilizing the linearly ramping conduction current approximation, Eq.(15), the annulus mass can be estimated as:

$$M = \frac{2\pi r(\Delta r)l_o m_i n_e}{Z} = \frac{\mu_o(\Delta r)}{24\pi} \frac{I_{Gen}^2 \tau_c^2}{r l_o}. \quad (16)$$

where r can be taken as R_c for cable gun sources.⁶ This mass scaling, as applied to the Hawk data, is shown in Fig. 42, which shows the $I_{Gen}^2 \tau_c^2$ product plotted versus observed Hawk delay. As the POS radius and length were not varied in these experiments, the $I_{Gen}^2 \tau_c^2$ product should be proportional to the annulus mass, which is related to the injected POS mass. Fig. 42 suggests that the injected plasma mass is not linear with the observed Hawk delay as might initially be expected. A sudden increase in POS mass is inferred for a delay of roughly 2.8 μs . Interferometric measurements of the cable gun plasma while firing Hawk have shown a factor of 2 to 3 increase in electron inventory during the conduction phase compared to measurements of cable gun plasma without firing Hawk.⁶ This increase is not observed with flashboard plasma sources.⁶ The results of Fig. 42 together with the observed increase in electron inventory during conduction strongly suggest that an increase in POS plasma mass occurs during the

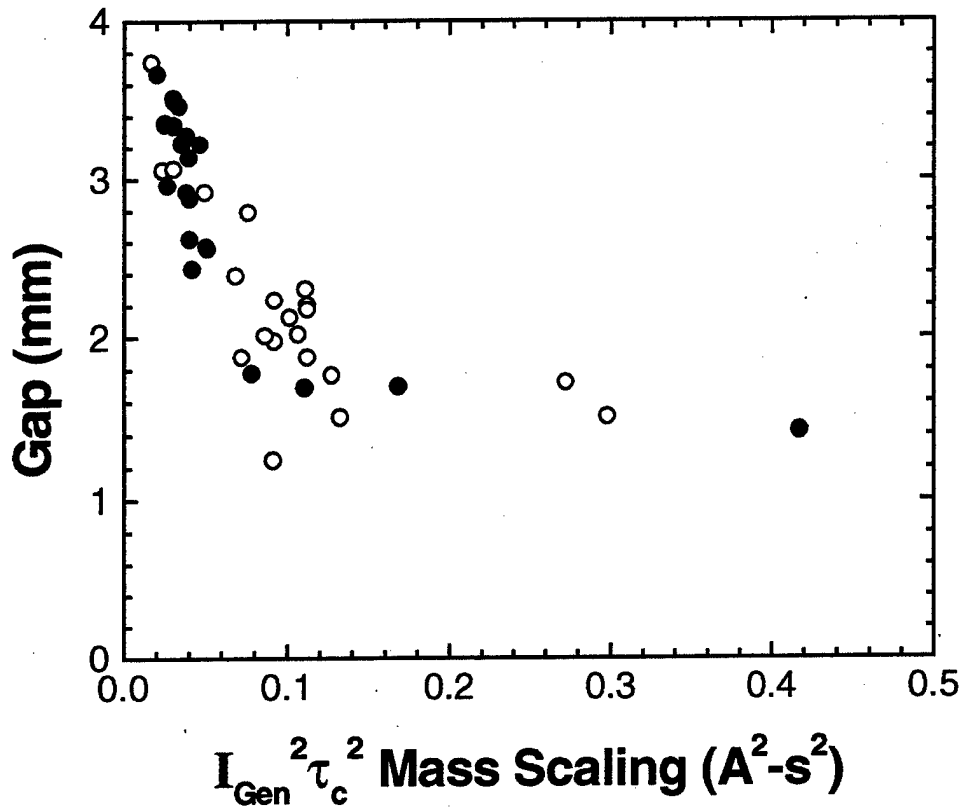


Fig. 43: Switch gap versus injected POS mass for both the long (filled circles) and short (open circles) POS-to-load configurations.

conduction phase as a result of ionization of neutrals, possibly neutrals released when cable gun plasma strikes the cathode.²⁹ This conclusion supports similar analysis of the previous electron density measurements,⁶ in which an average value of ~ 14 for the ratio of mass number to charge was obtained, appropriate for singly ionized carbon and fluorine. The cable guns are located 9 cm from the cathode surface, and the cable gun plasma has a directed velocity of ~ 3 cm/ μ s.⁶ Thus, cable gun plasma striking the cathode can lead to the production of neutrals ~ 3 μ s after the cable guns are fired, close to the time when the sudden increase in mass is inferred based on conduction time scaling.

The switch gap may also be plotted as a function of the initial plasma mass in the switch by applying the snowplow model for conduction time scaling. This is done in Fig. 43, which shows the switch gap plotted against the square of the $I_{Gen}\tau_c$ product. This plot shows the switch gap decreasing roughly linearly with initial plasma mass in the POS until the gap reaches approximately 1.5 mm. Further increasing the POS injected plasma mass has no apparent effect on the switch gap.

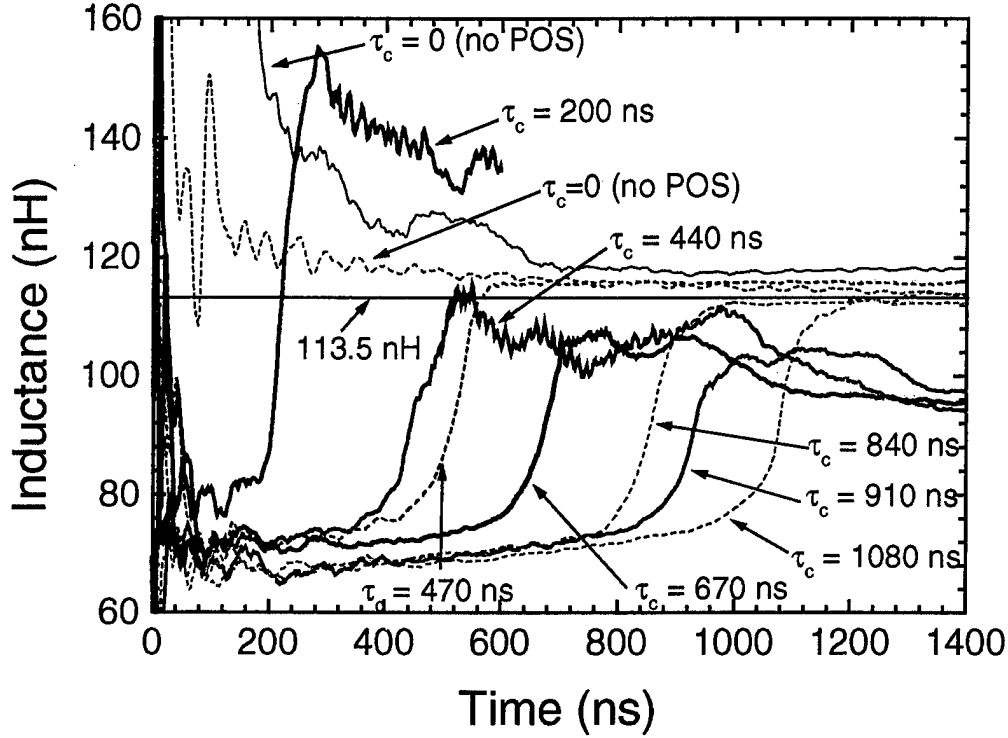


Fig. 44: Inductance uncovered between the upstream voltage monitor and the vacuum voltmeter during POS conduction and opening in the long POS-to-load configuration for several different conduction times. Shots with a diode load are represented by solid lines; while shots with a short circuit load are represented by dashed lines. The vacuum inductance between the upstream voltage monitor and the vacuum voltmeter is 113.5 nH.

4.6 Inductance Calculations and “location” of POS opening

As described in the previous section, the current-carrying plasma in the POS experiences a magnetic pressure on the upstream side that accelerates both the plasma and its associated current toward the load. This produces a time varying inductance in the generator/POS circuit. The inductance uncovered between the upstream voltage monitor and the load voltmeter can be expressed, using measured currents and voltages, as

$$L(t) = \frac{\int (V_d - V_L) dt}{I_{Gen}}, \quad (17)$$

where V_d is the voltage measured just upstream of the insulator, V_L is the load voltage measured with the wire voltmeter, and I_{Gen} is the upstream current. Using this expression, the time-varying inductance was calculated for several Hawk shots in both the long and short POS-to-load configurations. Conduction times for these shots ranged from 200 ns to 950 ns. Results for the long POS-to-load configuration are shown in Fig. 44, while results for the short POS-to-load configuration are shown in Fig. 45.

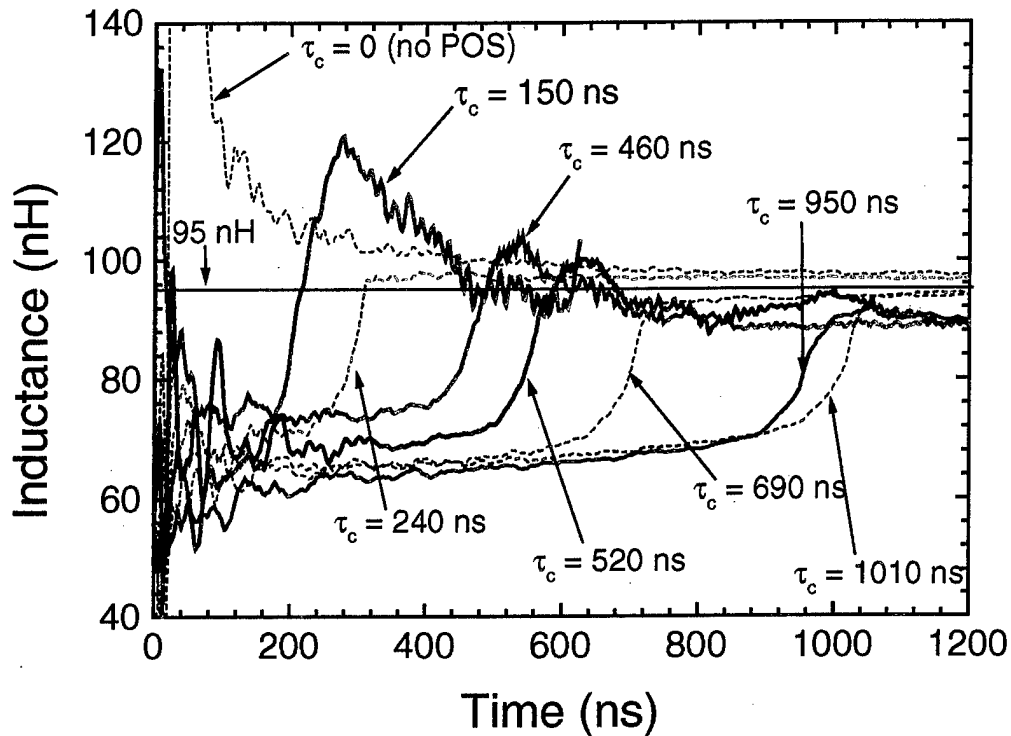


Fig. 45: Inductance uncovered between the upstream voltage monitor and the vacuum voltmeter during POS opening in the short POS-to-load configuration for several different conduction times. Shots with a diode load are represented by solid lines; while shots with a short circuit load are represented by dashed lines. The vacuum inductance between the upstream voltage monitor and the vacuum voltmeter is 95 nH.

For the long POS-to-load configuration, shown in Fig. 44, the initial inductance immediately after Hawk fires ranges approximately from 70 nH to 80 nH depending on the conduction time. For short conduction time shots, the initial inductance is closer to 80 nH, while for long conduction time shots, the initial inductance is closer to 70 nH. This indicates that the axial location of initial POS current conduction is farther upstream for long conduction time shots than for short conduction time shots. The delay between firing the POS cable guns and firing Hawk is larger for long conduction time shots than for short conduction time shots, and the POS plasma has more time to diffuse upstream prior to firing Hawk. So, the axial location where current can be conducted can move upstream as conduction time increases. During the conduction phase, the inductance gradually increases corresponding to the magnetic field pushing and distorting the plasma in the POS injection region. This is followed by a rapidly increasing inductance associated with the propagating current channel discussed in Sec. 3.1.1 and POS opening. The inductance increases sharply to nearly the full inductance value for the coaxial transmission line between the insulator and the load. The total inductance associated with this transmission line, roughly 113.5 nH in the long POS-to-load configuration, was determined from a Hawk shot using a short-circuit-load and no POS. It can be seen in Fig. 44 that for short conduction times (<300 ns), the calculated inductance immediately after opening exceeds the total inductance in the transmission

line. One possible reason for this unphysical result is an erroneously low load voltage measurement that may result from electron emission in the wire voltmeter. This problem seems only to occur for short conduction times, where a slow rising voltage pulse may allow for more emission in the wire voltmeter before the current in the voltmeter is sufficient to allow magnetic insulation. Errors in the voltage or current measurements resulting from transmission line effects may also be partly responsible for this feature in the inductance traces. It is important to note that in further analysis of the inductance measurements, the primary focus will be on the inductance uncovered prior to POS opening (i.e. prior to measurable voltage appearing at the load). Hence, electron emission in the wire voltmeter is not a concern at the times of interest in this further analysis. Inductance time histories for the short POS-to-load configuration, shown in Fig. 45, are similar to those for the long POS-to-load configuration in their initial behavior and general trends. The total inductance in the coaxial transmission line was 95 nH in the short POS-to-load case.

Assuming, for now, that the propagating current channel is purely radial (data in Sec. 3.1.1 suggest that it is not purely radial), the inductance time histories allow an estimate of the axial location of the translating plasma sheet at any time of interest. The inductance uncovered at the time of POS opening can therefore be used to determine the location of the (assumed) radial, current-carrying plasma channel when the POS opens (i.e. when load voltage begins to increase). This is plotted in Fig. 46(a) and (b), which show the axial location where the POS "opens" as a function of conduction time based on the inductance uncovered at POS opening for the long and short POS-to-load configurations, respectively. In Fig. 46(a) and (b), the axial position of POS opening is measured relative to the midplane of the POS injection region, (see Fig. 1). For comparison, the axial location nearest the POS where bremsstrahlung emission is observed in side-viewing x-ray pinhole photographs (see Fig. 14 and Fig. 15) is plotted as well. This represents another possible location of opening because high energy electrons emitted from the opened POS may strike the anode anywhere between the location of the POS at opening and the load thereby producing bremsstrahlung radiation. The lines in Fig. 46 are linear fits to the data points. Finally, for the long POS-to-load configuration [Fig. 46(a)], a crude estimate for the location of POS opening was obtained based on relative timing of the downstream current and load voltage signals in Fig. 12. Since current monitors were only located at one axial position in the short POS-to-load configuration, the relative timing of current and load voltage signals did not provide any additional information on the location of POS opening for that case. As shown in Fig. 46(a), the three different methods for estimating the location at which the POS opened correlate fairly well in the long POS-to-load configuration. In Fig. 46(a), the location of POS opening based on calculated inductance exhibits more scatter than does the location of POS opening based on side-viewing x-ray pinhole camera photographs. Also, the location of POS opening based on calculated inductance does not vary as much with conduction time as does the location of POS opening based on the side-viewing x-ray pinhole camera photographs.

Based on the inductance calculations, opening occurs closer to the POS for the short than for the long POS-to-load configuration. On the other hand, the pinhole camera photographs yield approximately the same opening location for both POS-to-load configurations.

5.0 Conclusions

Two different POS-to-load configurations were studied in this experiment, one with a POS-to-load length of 33 cm, and the other with a POS-to-load length of 49 cm. The

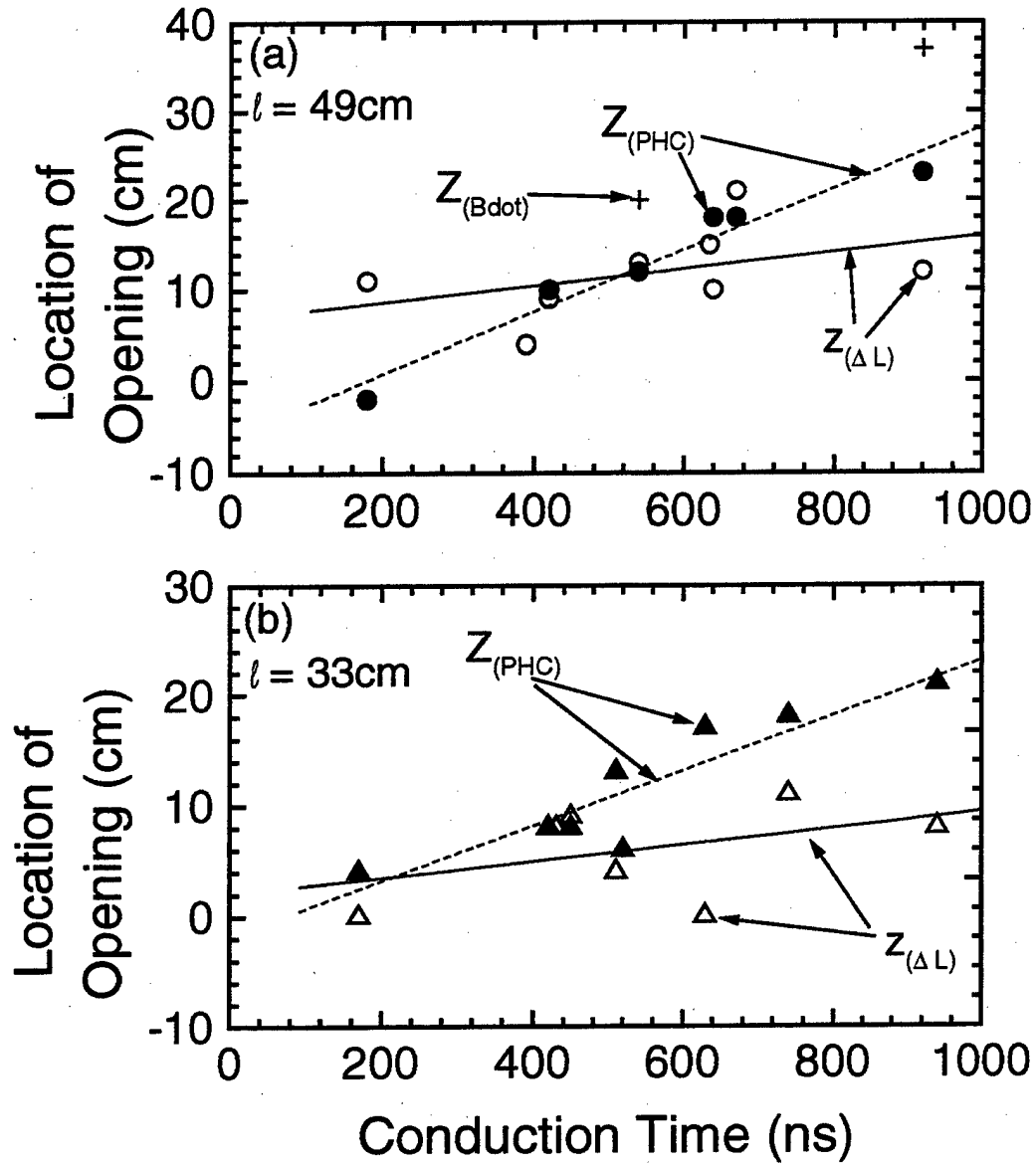


Fig. 46: Inferred axial location of POS opening (relative to the midplane of the plasma injection region) based on both inductance calculations and side-viewing x-ray pinhole camera photographs for (a) the long POS-to-load configuration and (b) the short POS-to-load configuration.

longer POS-to-load distance resulted in reduced plasma influences on the diode, while the shorter POS-to-load distance reduced current loss between the switch and the load. Based on these results, there is an optimum POS-to-load distance (i.e. a POS-to-load distance at which diode power is maximized) determined by the need to minimize current losses while ensuring that plasma reaching the load does not adversely reduce the diode impedance and voltage.

Conduction time was another parameter that was varied in these experiments. The optimum conduction time was found to be $\sim 0.50 \mu\text{s}$ for the short POS-to-load configuration, and $\sim 0.65 \mu\text{s}$ for the long POS-to-load configuration. For conduction times less than optimum, generator and load currents decreased, resulting in lower diode power. For conduction times greater than optimum in the short POS-to-load configuration, load behavior deteriorated, likely due to POS-plasma influences on the diode. For conduction times near or greater than optimum in the long POS-to-load configuration, excessive current losses between the POS and the load reduced diode power.

The diode A-K gap was varied to study the effect of diode impedance on POS-load coupling. The optimum A-K gap was 10 to 15 mm, corresponding to an impedance of approximately 5Ω . For larger A-K gaps, upstream current losses increased, while for smaller A-K gaps, low diode impedance and consequently low load voltage resulted. This behavior is consistent with the switch-limited, load-limited picture of POS operation. This optimum impedance value is larger than was observed in previous work with flashboards, a result of using the cathode load current rather than anode load current in determining the impedance. Also, the fact that a stainless steel anode rather than a tantalum anode was used in the flashboard experiments may have resulted in a different optimum diode impedance due to a different gap closure rate.

In these cable gun experiments, the optimum conduction time ($0.50 - 0.65 \mu\text{s}$) was shorter and the peak diode power ($200 - 240 \text{ GW}$) was lower than was observed in previous flashboard experiments. In those experiments, 400 GW peak power was obtained at conduction times of $0.85 \mu\text{s}$.⁹ Possible reasons for this discrepancy are differences in plasma sources, POS geometry, and anode converter material. Another important result is that at conditions for maximum power delivery to the load, about half the load current is flow current.

The effect of anode material on load impedance and power was only observed for shots without a POS. For these shots, covering the tantalum foil with $\frac{1}{4}$ -mil aluminum foil yielded higher diode impedance and a longer pulse duration than the bare tantalum foil, possibly a result of hindering impurities in the tantalum from being released into the diode gap. For shots with a POS, there was no clear difference between the two load anode materials in terms of load impedance. Based on the measured load voltage and load cathode current, the diode impedance for conduction times equal to or less than optimum follows that predicted for a pinched-beam diode, thus supporting the use of cathode current when calculating diode impedance. For long conduction times in the short POS-to-load case, the diode impedance is less than the pinched-beam value, thus supporting the notion that the diode impedance is affected by POS plasma in this case.

It was also found that the current propagation (transfer process) was affected by changing the conduction time, but was not affected by changing the load impedance. At short conduction times, voltage is observed at the load prior to current being observed on any of the downstream B-dot monitors. Furthermore, signals begin to rise on all the current monitors downstream of the POS simultaneously, indicating that current transfer to the load is precipitated by diode emission. At moderate (optimum) conduction times, a plasma current channel is observed to propagate past the downstream anode current monitor closest to the POS at the same time as voltage appears on the load. This voltage reaches 100 kV , but is not sufficient to drive current through the diode load. Instead, a resistive plasma current channel propagates to the load, after which the diode current and voltage increase to deliver the maximum diode power with no apparent deleterious effects on the diode impedance from the plasma associated with the current channel. In the long-conduction-time case, voltage does not appear on the load until just

before or at the same time as the current channel reaches the anode current monitor closest to the load. In this case, the load-impedance time history and amplitude are adversely affected by the current-channel plasma. Further work is required to fully understand the implications of these observations and the relationships between the plasma-current-channel density, current losses in the POS-to-load region, POS-plasma species and e-beam diode behavior. Based on the downstream current monitors, the current channel propagates faster along the anode than along the cathode, and consequently, there is an axial component to the current flow.

One interesting new result from these experiments is that the POS gap is always approximately equal to the critical gap for magnetic insulation, even in the load-limited regime. Expressing the POS gap in terms of impedance, the flow impedance was found to scale approximately as $Z_{flow} \approx 30D_{crit}/R_c$. This implies that the POS gap adjusts itself based on the load conditions to maintain saturated electron flow in the POS. The mechanism by which the load conditions are communicated to the POS is not clear, and will be the subject of further research. A larger POS gap, though fully saturated, is still desirable to obtain higher flow impedance and extend the range of obtainable voltages. Several experiments have shown that the gap can be changed, e.g., by varying geometry⁷ and POS plasma species.³⁰

Based on an MHD snowplow model for POS conduction time scaling, a sudden increase in POS mass was inferred for a 2.8- μ s delay between firing the cable guns and firing Hawk (Fig. 42). Based on this inference, the previously observed increase in electron density during the conduction phase with a cable gun POS⁶ results from ionization of neutrals as opposed to additional ionization of charged species. The cable guns are located 9 cm from the cathode surface, and the cable gun plasma has a directed velocity of ~ 3 cm/ μ s.⁶ Thus, cable gun plasma striking the cathode can lead to the production of neutrals ~ 3 μ s after the cable guns are fired, close to the time when the sudden increase in mass is inferred based on conduction time scaling. Previous interferometric measurements on Hawk have indicated a factor of 2-3 increase in the electron number density during conduction.⁶ While this increase was attributed to further ionization of plasma species injected from the cable guns (which would not affect the actual mass in the POS), these results are also consistent with an electron density increase resulting from ionization of neutrals.

Acknowledgements

This research was sponsored by the Defense Threat Reduction Agency. The authors wish to thank Rick Fisher and Eric Featherstone for their expert technical assistance.

- ¹ R. J. Commisso, P. J. Goodrich, J. M. Grossman, D. D. Hinshelwood, P. F. Ottinger, and B. V. Weber, "Characterization of a microsecond-conduction-time plasma opening switch," *Phys. Fluids B*, vol. 4, pp. 2368-2376, (1992).
- ² B. V. Weber, R. J. Commisso, P. J. Goodrich, J. M. Grossman, D. D. Hinshelwood, P. F. Ottinger, and S. B. Swanekamp, "Plasma opening switch conduction scaling," *Phys. Plasmas*, vol. 2, pp. 3893-3901, (1995).
- ³ B. V. Weber, J. R. Boller, R. J. Commisso, P. J. Goodrich, J. M. Grossmann, D. D. Hinshelwood, J. C. Kellogg, P. F. Ottinger, and G. Cooperstein, "Microsecond-conduction-time POS experiments," in *Proc. 9th Int. Conf. High-Power Particle Beams*, Washington D.C., pp. 375-384, (1992).
- ⁴ J. R. Boller, R. J. Commisso, P. J. Goodrich, D. D. Hinshelwood, J. C. Kellogg, J. D. Shipman Jr., B. V. Weber, and F. C. Young, "Design and Performance of Hawk, A Versatile Pulsed Power Generator," NRL Memorandum Report # 6748, 1991 (unpublished).
- ⁵ J. R. Goyer, D. Kortbawi, F. K. Childers, and P. S. Sincereny, "Low jitter operation of a plasma opening switch," *J. Appl. Phys.*, vol. 74, pp. 4236-4238, (1993).
- ⁶ B. V. Weber, D. D. Hinshelwood, and R. J. Commisso, "Interferometry of flashboard and cable-gun plasma opening switches on Hawk," *IEEE Trans. Plasma Sci.* vol. 25, pp. 189-195, (1997).
- ⁷ P. J. Goodrich, D. D. Hinshelwood, R. J. Commisso, J. M. Grossman, J. C. Kellogg, and B. V. Weber, "High power opening switch operation on Hawk," in *Proc. 9th IEEE Pulsed Power Conf.*, IEEE Cat. no. 93CH3350-6, Albuquerque, NM, June 1993, pp. 511-515.
- ⁸ P. J. Goodrich, R. C. Fisher, D. D. Hinshelwood, J. R. Boller, R. J. Commisso, and B. V. Weber, "Microsecond plasma opening switch experiments on Hawk with an e-beam diode load," in *Proc. 9th Int. Conf. High-Power Particle Beams*, G. Cooperstein and D. Mosher, eds., Washington D.C., pp. 609-614, (1992).
- ⁹ P. J. Goodrich, J. R. Boller, R. J. Commisso, D. D. Hinshelwood, J. C. Kellogg, and B. V. Weber, "Plasma opening switch experiments on Hawk with an e-beam diode load," in *Proc. 8th IEEE Pulsed Power Conf.*, San Diego, CA, June 1991, pp 515-519.
- ¹⁰ B. V. Weber, R. J. Commisso, G. Cooperstein, J. M. Grossman, D. D. Hinshelwood, D. Mosher, J. M. Neri, P. F. Ottinger, and S. J. Stephanakis, "Plasma erosion opening switch research at NRL," *IEEE Trans. Plasma Sci.*, vol. PS-15, pp.629-634, (1987).
- ¹¹ D. G. Colombant and B. V. Weber, "A simple model for flashboard plasma expansion," *IEEE Trans. Plas. Sci.*, vol. PS-15, p.741, (1987).
- ¹² A. B.-A. Baranga, N. Qi, and D. A. Hammer, "Flashboard plasma characterization using spectroscopy," *IEEE Trans. Plasma Sci.*, vol. 20, pp. 562 - 567, (1992).
- ¹³ G. E. Leavitt, J. D. Shipman, Jr., and I. M. Vitkovitski, "Ultrafast High Voltage Probe," *Rev. Sci. Instrum.*, vol. 36, pp. 1371-1372, (1965).
- ¹⁴ A. G. Brandelik and P. H. Breitfeld, "Accurate voltage probe for pulse power systems," *IEEE Conf. Record of the Workshop on Measurement of Electrical Quantities in Pulsed Power Systems II*, (IEEE Cat. #: 88CH2327-5), (1988).
- ¹⁵ B. V. Weber, R. J. Commisso, P. J. Goodrich, D. D. Hinshelwood, W. F. Oliphant, P. F. Ottinger, and F. C. Young, "Ion emission from PEOS plasmas," in *Proc. 7th Int. Conf. High Power Particle Beams*, Karlsruhe, Germany, pp. 1131-1136, (1988).
- ¹⁶ R. J. Commisso, J. R. Boller, J. M. Grossmann, D. D. Hinshelwood, J. C. Kellogg, D. Mosher, P. F. Ottinger, and B. V. Weber, "Characterization of a 1- μ s, 1-MA plasma erosion opening switch," *Conf. Record-Abstracts for IEEE Int. Conf. Plas. Sci.*, Buffalo NY, May 22 - 24, 1989, IEEE Cat. No. 89CH2760-7, p. 42.
- ¹⁷ D. D. Hinshelwood, R. J. Commisso, P. J. Goodrich, J. M. Grossmann, J. C. Kellogg, P. F. Ottinger, and B. V. Weber, "Axially resolved PEOS measurements at microsecond conduction times," in *Proc. 8th Int. Conf. on High-Power Particle Beams*, Novosibirsk USSR, pp. 1034-1039, (1990).
- ¹⁸ B. V. Weber, P. F. Ottinger, R. J. Commisso, J. R. Goyer, D. Kortbawi, J. Thompson, J. E. Rowley, D. Filios, and M. A. Babineau, "The Decade performance assessment program," in *Proc. 11th Int. Conf. on High-Power Particle Beams*, Prague, Czech Republic, June 1996, p. 121.
- ¹⁹ R. J. Commisso, B. V. Weber, P. J. Goodrich, J. M. Grossman, S. B. Swanekamp, P. F. Ottinger, R. A. Riley, "Review of Hawk power flow experiments," *Pulsed Power Physics Technote #95-12*, 1995 (unpublished).

- ²⁰ J. M. Creedon, "Relativistic Brillouin flow in the high v/γ diode," *J. Appl. Phys.*, vol. **46**, pp. 2946-2955, (1975).
- ²¹ T. W. L. Sanford, J. A. Halbleib, J. W. Poukey, C. E. Heath, and R. Mock, "Dose-voltage dependence of coaxial bremsstrahlung diodes," *Nucl. Inst. and Meth. in Phys. Res.*, vol. **B34**, pp. 347-356 (1988).
- ²² T. W. L. Sanford, J. A. Halbleib, J. W. Poukey, C. E. Heath, and R. Mock, "Dose-voltage dependence for Helia/Hermes III bremsstrahlung diodes," in *Proc. IEEE Particle Accelerator Conference*, Washington D.C. March 16-19, 1987, IEEE Cat. No. 87CH2387-9, pp. 931-933.
- ²³ C. W. Mendel, M. E. Savage, D. M. Zagar, W. W. Simpson, T. W. Grasser, and J. P. Quintenz, "Experiments on a current-toggled plasma-opening switch", *J. Appl. Phys.* vol. **71**, pp. 3731-3746, (1992).
- ²⁴ C. W. Mendel, and S. E. Rosenthal, "Modeling magnetically insulated devices using flow impedance," *Phys. Plasmas*, vol. **2**, pp. 1332-1342, (1995).
- ²⁵ J. R. Goyer and D. Kortbawi, "Observations and Implications of Gap Closure in plasma opening switch operation," *J. Appl. Phys.* Vol. **76**, 3321-3325, (1994).
- ²⁶ S. B. Swanekamp, J. M. Grossman, P. F. Ottinger, R. J. Comisso, and J. R. Goyer, "Power flow between a plasma-opening switch and a load separated by a high-inductance magnetically-insulated transmission line," *J. Appl. Phys.*, vol. **76**, pp. 2648-2656, (1994).
- ²⁷ W. Rix, D. Parks, J. Shannon, J. Thompson, and E. Waisman, "Operation and empirical modeling of the plasma opening switch," *IEEE Trans. Plas. Sci.*, vol **19**, pp. 400-407, (1991).
- ²⁸ D. D. Hinshelwood, B. V. Weber, J. M. Grossman, and R. J. Comisso, "Density redistribution in a microsecond conduction time plasma opening switch," *Phys. Rev. Lett.*, vol **68**, p. 3567, (1992).
- ²⁹ R. J. Comisso et. al., in *Proc. of 12th Int. Conf. on High Power Particle Beams* 98, Israel, June 1998.
- ³⁰ P. S. Ananjin, V. B. Karpov, Ya. E. Krasik, I. V. Lisitzin, A. V. Petrov. and V. G. Tolmacheva, "Application of pulsed gas vents for plasma opening switches," *IEEE Trans. Plasma Sci.*, vol. **20**, pp. 537 - 542, (1992).